

ULTRAFAST SPECTROSCOPY OF SEMICONDUCTING AND MULTIFERROIC MATERIALS

BY SHITAO LOU

**A dissertation submitted to the
Graduate School—New Brunswick
Rutgers, The State University of New Jersey
in partial fulfillment of the requirements
for the degree of
Doctor of Philosophy
Graduate Program in Physics and Astronomy**

**Written under the direction of
Prof. Frank M. Zimmermann
and approved by**

New Brunswick, New Jersey

October, 2007

ABSTRACT OF THE DISSERTATION

ULTRAFAST SPECTROSCOPY OF SEMICONDUCTING AND MULTIFERROIC MATERIALS

by Shitao Lou

Dissertation Director: Prof. Frank M. Zimmermann

In this thesis, we have used ultrafast spectroscopy to study the optical properties of two semiconductors, GaAs and Ge, and one hexagonal multiferroic material, LuMnO₃. Both semiconductor and multiferroic materials are of great importance technologically and economically. By using ultrafast spectroscopy, we obtained time resolved electron and phonon dynamics directly, which is unavailable by conventional optical methods.

Electron-hole pairs, coherent phonon oscillations and an optical coherence response are excited when femtosecond laser pulses interact with either GaAs or Ge crystals. The coherent phonon mode excited in GaAs/Ge is of T_2/T_{2g} symmetry as determined by probe beam polarization analysis. The pump polarization dependence of the phonon oscillation is consistent with the transient stimulated Raman scattering (TSRS) mechanism. From the pump polarization dependence of the phonon oscillation, we have identified two excitation mechanisms contributing to the coherent phonon in GaAs,

one is consistent with TSRS, and the other is consistent with screening effect of photo-excited electrons.

The femtosecond laser pulse, with 800 nm center wavelength and polarized perpendicular to the c axis of LuMnO₃, excites a narrow intra-atomic d_{xy, x^2-y^2} to $d_{3z^2-r^2}$ transition in Mn. This excitation results in a transient reflectivity change for light of the same wavelength and polarization, by partial saturation of the transition. The relaxation time of this electronic excitation is about 1 ps. Furthermore, the electronic excitation resonantly excites a coherent optical phonon with A₁ symmetry (TO: 118 cm⁻¹ and LO: 120 cm⁻¹), involving Lu ions motion along the c-axis, which is identified to be the soft mode driving the ferroelectric transition. A remarkable reversal of the sign of the oscillation amplitude (π phase shift) of the reflectivity curve was observed upon comparing longitudinal optical (LO) with transverse optical (TO) mode geometries. The phase reversal is attributed to the macroscopic electric depolarization field accompanying IR active longitudinal phonon modes, but absent in TO modes, or to coupling of LO phonon coordinate to a change in ferroelectric polarization upon to excitation via a macroscopic electric field.

Acknowledgements

The past 6 years of my Ph.D. program have been challenging in many ways; at the end of the special journey, I am pleased to take this opportunity to express my sincere gratitude to those who helped me, whether his/her name is list below or not.

First, I wish to express my gratitude to my thesis adviser, Professor Frank M. Zimmermann for his direction and support, and Professor Robert A. Bartynski for his help in these years. My Gratitude also goes to all other thesis committee members: Professor David Vanderbilt, Professor Daniel E. Murnick, and Dr. Oleg Mitrofanov. I appreciate the help from all other professors in the physics department, especially from Professor Premala Chandra, Professor Sang-Wook Cheong, Professor Jolie A. Cizewski, Professor Yves J. Chabal, Professor Mark Croft, Professor Eric Garfunkel, Professor Michael Gershenson, Professor Torgny Gustafsson, Professor Theodore E. Madey, Professor Ronald D. Ransome, and Professor Weida Wu.

I also appreciate Professor M.B. Taylor's help in the shell model, Dr. A. Souchkov's help in the IR spectra of LuMnO_3 , and Dr. Girsh Bloomberg's help with the Raman spectra of LuMnO_3 . I appreciate the support from the Lucent-Rutgers foundation and the Rutgers Department of Physics and Astronomy. I wish to express my gratitude to Mr. Zhiqiang Hu (Nanofirst, Shanghai) for his free AFM controller and technique support.

I wish to express my gratitude to Dr. Namjun Hur, Dr. Soonyong Park, and Mr. Chenglin Zhang for the preparation of the LuMnO_3 samples. I appreciate the help from the machine shop and the electric shop. Thank Dr. Burak M. Yilmaz, Dr. Craig Fennie, and Mr. Eric Bersch, Professor R. Merlin for helpful discussions. I wish to express gratitude to all my friends in the physics department, especially to Dr. Jian

Wei, Dr. Meng Li, Mr. Hao Wang, Dr. Wenhua Chen and Mr. Min Dai, Mr. Tian Feng, Mr. Xinjie Wang, and Dr. Hsu-Chang Lu.

I wish to express my gratitude to my wife, Hua Yao for her help in academics and life. My gratitude also goes to our daughter, Kristel Lou, my parents and parents-in-law.

Cleveland, Sept. 13, 2007

Dedication

my wife Hua

and

our daughter Kristel

Thank you and I love you!

Table of Contents

Abstract	ii
Acknowledgements	iv
Dedication	vi
List of Figures	x
1. Introduction	1
1.1. Time Resolution and Apparatus	1
1.2. Introduction to Ultrafast Spectroscopy	2
1.3. Applications of Ultrafast Spectroscopy	4
1.3.1. Applications in Metals	4
1.3.2. Applications of Ultrafast Spectroscopy in Semiconductors	5
1.3.3. Applications of Ultrafast Spectroscopy in Oxide Compounds	9
1.4. Thesis Outline	11
2. Experimental Techniques	13
2.1. Pump-Probe Technique	13
2.2. Experimental Setup	15
2.2.1. Pump-probe Reflection Spectroscopy	15
2.2.2. Differential Reflection Pump-Probe Spectroscopy	18
2.2.3. Pump-Probe Transmission Spectroscopy	20
2.3. Calibration of Initial Phase	21
3. Femtosecond Spectroscopy of Polar and Non-Polar Semiconductors	23

3.1.	Introduction	23
3.1.1.	Structure and Optical Properties of GaAs and Ge	23
3.1.2.	Ultrafast Time Resolved Measurements of Semiconductors	26
3.2.	Pump-Probe Spectroscopy of GaAs	29
3.2.1.	Pump-Probe Effects in GaAs	29
3.2.2.	Pump Polarization Dependence of Phonon Oscillation	31
3.2.3.	Pump Power Dependence of Phonon Oscillation	34
3.2.4.	Crystal Orientation Dependence of Phonon Oscillation	37
3.3.	Pump-Probe Spectroscopy of Ge	40
3.3.1.	Pump Polarization Dependence in Ge	40
3.3.2.	Crystal Orientation Dependence of Ge	41
3.4.	Discussion and Conclusion	42
3.4.1.	Excitation Mechanisms	42
3.4.2.	Continuous Wavelet Transform Analysis	52
3.4.3.	Summary	57
4.	Femtosecond Spectroscopy of Ferroelectric LuMnO₃	59
4.1.	Structure and Properties of LuMnO ₃	59
4.1.1.	Crystal Structure	59
4.1.2.	Anti-Ferromagnetic Properties	62
4.1.3.	Ferroelectricity	64
4.2.	Experimental Procedures and Results	64
4.2.1.	Results of a-b Face	65
4.2.2.	Results of a-c Face	66
4.3.	Symmetry Analysis of Phonon Spectra	68
4.4.	Shell Model Calculation	70
4.5.	Discussion and Conclusion	72

4.5.1. Phonon Excitation Mechanism	72
4.5.2. Phonon Coordinate Motion	74
4.5.3. Depolarization Field Effect	77
4.5.4. Summary	80
5. Summary and Future Work	82
5.1. Summary	82
5.2. Future Work	84
5.2.1. Future Work With GaAs and Ge	84
5.2.2. Future Work on Hexagonal Multiferroic Manganites	85
5.3. Conclusion	86
Appendix A. An Introduction to Femtosecond Laser Pulses	87
A.1. Wave Packets and Pulse Width Measurement	87
A.2. Group Velocity Dispersion and Compensation	89
A.3. Laser Pulse Generation	93
A.3.1. Principle of Kerr-Lens Mode-locking	94
A.3.2. Aligning the Ti:Sapphire Laser	96
Appendix B. Optical Modulator	99
Appendix C. List of Acronyms	102
References	103
Vita	113

List of Figures

1.1. Pump-probe absorption saturation responses	6
1.2. Absorption saturation data	7
1.3. Reflectivity change curve on surface of GaAs crystal	8
2.1. Schematic diagram of generic two beam experiment setup	14
2.2. Schematic diagram of reflectivity change measurement	16
2.3. Function block diagram of the position sensitive photodiode	18
2.4. Photograph of the optical bench layout	19
2.5. Schematic diagram of differential reflectivity change measurement . .	19
2.6. Schematic diagram of transmission change measurement	20
3.1. Structure and band structure of GaAs crystal	24
3.2. Structure and band structure of Ge crystal	26
3.3. GaAs reflectivity change curves	29
3.4. GaAs differential reflectivity change curve.	30
3.5. Pump beam polarization geometry	31
3.6. GaAs pump polarization dependence	32
3.7. GaAs pump polarization dependence on phonon oscillations	33
3.8. GaAs Pump intensity dependence in the reflectivity change	34
3.9. GaAs pump intensity dependence of coherent phonon oscillations . .	35
3.10. GaAs Pump beam power dependence in the reflectivity change	36
3.11. GaAs pump beam power dependence of phonon oscillations	37
3.12. GaAs Sample orientation dependence	38
3.13. GaAs crystal orientation dependence of phonon oscillations	39

3.14. Ge pump polarization dependence of reflectivity change	41
3.15. Ge pump polarization dependence of phonon oscillations	42
3.16. Ge sample orientation dependence of the phonon oscillations	43
3.17. Illustration of impulsive coherent phonon excitation mechanism	44
3.18. Illustration of displacive excitation of coherent phonons	45
3.19. polar plot of coherent phonon amplitude vs initial phase	48
3.20. Schematic of the effect of excited electrons on the coherent phonon excitation	50
3.21. Continuous wavelet transforms of GaAs reflectivity change curve . . .	53
3.22. Wavelet transfer of GaAs unbalanced reflectivity change curve	54
3.23. Simulated reflectivity change with three different contributions	55
3.24. The CWT result of total contribution	56
4.1. Schematic of unit cell structure of LuMnO_3 crystal	61
4.2. The splitting of d orbital energy levels of the Mn ion	61
4.3. IR spectra of LuMnO_3	62
4.4. Phase diagram of HoMnO_3	63
4.5. Reflectivity changes of LuMnO_3 crystal from a-b face	65
4.6. Oscillatory components of reflectivity curves from a-b face	66
4.7. Pump-probe Spectra of LuMnO_3 from a-c face	67
4.8. Oscillation components of reflectivity change curve from a-c face . .	67
4.9. Schematic view of LuMnO_3 phonon motion	74
4.10. Oscillatory components from different plane	78
4.11. Schematic view of LO and TO phonon modes	80
A.1. Schematic diagram of autocorrelation measurement	88
A.2. Spectrum and autocorrelation of a pulse	90
A.3. Schematic of optical path of prism pairs	90
A.4. Schematic for calculating the prism pair dispersion	91

A.5. Ti:Sapphire laser schematic for calculation	95
A.6. Relationship between the pulse duration, energy and negative GVD . .	96
A.7. Region of stability	96
A.8. Ti:Sapphire laser schematic	97
B.1. 3D schematic of the optical modulator	99
B.2. Photograph of the optical modulator	100
B.3. Schematic of current driver of the optical modulator	101

Chapter 1

Introduction

1.1 Time Resolution and Apparatus

In order to record events that happen on a time scale faster than 0.01 second, we have to use sophisticated apparatus. For example, we use high speed video recorders to record sports a competition, and determine the champion by playing back the video at a slower speed. Camcorders can record more than 1000 frames per second [1], which means the time resolution is better than 0.001 second. If an event can be represented by an electrical pulse, the time resolution can be on the order of a nanosecond.

When a physical event happens on the picosecond time scale, we do not have any instrument to observe it directly in a time-resolved fashion. To obtain ultrafast time resolution, instruments have to have the capability to synchronize with physical events. In the past 30 years, the development of pulsed lasers has been very rapid [2, 3]. Today, the shortest achievable pulse widths are of the order of femtoseconds [2]. If we use laser pulses to trigger physical events, the initial time of these events will be synchronized with the pulse. The superposition of many synchronized events have the same time sequence as a single event. Another laser pulse can be used to detect the physical events. Thus the transient information of the physical events can be obtained. However, the data recording speed (now 10^9 per second) is still not fast enough to continuously record physical events in the subpicosecond regime. If the event can be easily repeated, we can record one data point at a certain time, and record another data at another time when the same event happens again. By this method, we can record the whole ultrafast process of the event with slow recording speed devices. The time

difference between the first pulse (pump pulse) and the second pulse (probe pulse) can be accurately controlled through the arrangement of the optical path. So we can obtain femtosecond time resolution by using a laser pulse to synchronize physics events and another pulse (optical, tera Hertz electromagnetic, electron, or X ray pulse) to probe the changes after some delay.

Today, pulsed lasers can produce pulses as short as 6 fs [2], which is only about 3 periods of the electro-magnetic field oscillation. It is very difficult to shorten the laser pulse further, limiting the time resolution of ultrafast spectroscopy¹. One possible solution and extension to even shorter time is to use X-ray pulses since X-rays have shorter wavelength. Ultrafast spectroscopy can be used to observe the time resolved dynamic processes, which enable us to gain insight into the dynamics on the femtoseconds time scale, which is impossible via classical spectroscopy.

1.2 Introduction to Ultrafast Spectroscopy

At the end of the 1970's and the beginning of the 1980's, most pulsed lasers only produced picosecond laser pulses [3], and time resolved Raman spectroscopy was used to study the dynamics of phonons [4]. In the case of a 1 picosecond pulse with 600-800 nm center wavelength, the transform limited spectral width is of the order of 1 nm while the Raman shift is about 2 nm per THz (33.3 cm^{-1}). Raman peaks of optical phonon modes with frequencies of several THz are well separated from the elastic peak in the spectrum. This technique was used for measuring the dynamics of long life time phonons ($> 1\text{ps}$). As the laser pulse becomes shorter (on the order of 10 femtoseconds), the pulse spectral width becomes larger (on the order of 10 nm), and consequently the Raman scattering peaks overlap the unshifted spectrum peak, which makes ultrafast Raman spectroscopy impractical. As the width of spectrum increases, directly measuring the absorption spectrum of a reflected or transmitted beam becomes

¹In nanotechnology, the minimum controlled distance is of the order of \AA , much less than 300 nm, the distance that light travels in 1 fs.

a method to study the dynamics of absorptive materials [5,6,7]. We can also obtain the dynamic information by studying the change of the absorption curve [5,6,7].

On the other hand, the subpicosecond laser pulse duration is shorter than the oscillation period of most acoustic phonons and some optical phonons. Reflection and transmission of ultrashort laser pulses in a material are transient processes comparable to the time scale of phonon oscillations, especially when the pulse width is shorter than 50 fs. For example, excitation and relaxation of electrons, excitons, phonons, etc, give rise to transient changes of the complex refractive index, thus leading to transient changes in reflectivity or transmission. The reflectivity/transmission of the probe beam has been measured to study the dynamics of electrons [8,9,10], phonons [10,11,12,13,14,15] and excitons [10]. To improve the accuracy of time control, interferometric techniques have been used in some experiments [16,10]. With ultrashort pulses, the decay of photo-excited electrons and phonon oscillations were observed in semiconductors, metals, and compounds materials [8,9,10,11,12,13,14,17,18,19,20]. In reflectivity change curves, coherent phonons or polaritons exhibit a decaying sine or cosine like oscillation. The excitation of incoherent electrons or excitons gives rise to a sudden drop or rise in reflectivity, which then relaxes exponentially. The Fourier transform is a common method to analyze the experimental data. A new method, Continuous Wavelet Transform (CWT), has been used to observe real time frequency changes or interactions [15]. In this method, a short period of time is windowed and Fourier transformed locally, and as the window shifts on the time sequence, the time-frequency relationship is obtained.

Nonlinear optical effects of the probe beam have also been used to study pump-induced changes. Optical second harmonic generation (SHG) measurements are the most popular nonlinear methods [21,22,23,24,25,26]. Luminescence excited by the probe beam is another choice for the pump-probe effect to investigate property changes of the sample [9,27,28]. Other kinds of laser induced pulsed beams have also been used as the probe beam, for example, THz electromagnetic pulses [29,30,31,32,33,34,35,

36, 37] and electron pulses [38, 39, 40, 41, 42]. The terahertz beam detects the material properties in the terahertz frequency range. Low Energy Electron Diffraction (LEED) has been widely used to detect the structure of crystals; when a subpicosecond electron pulse is used as the electron source in LEED, the transient structure of the object can be obtained by changing the delay time between the pump laser pulse and the probe electron pulse [38, 39, 40, 41, 42].

1.3 Applications of Ultrafast Spectroscopy

Ultrafast laser spectroscopy has been widely used in physics, chemistry, and other fields because of its femtosecond temporal resolution. It is used to investigate the dynamics of electrons, phonons and excitons in semiconductors, metals and compound materials.

1.3.1 Applications in Metals

Scientists have employed ultrafast spectroscopy to study the properties of metals. Femtosecond time resolved two-photon photoemission has been used to study the electron dynamics of Ni and Cu surfaces [16, 43]. The relaxation of the photoexcited charge carriers, as well as quantum beats, were observed [16]. Hase *et al.* used pump probe reflectivity change measurement to study the dynamics of coherent phonons in bismuth [44, 45, 46]. For low density excitation, the phonon mode excited is mainly of A_{1g} symmetry. As the excitation density increases, the amplitude of an E_{1g} symmetry mode increases.

The surface of a ferromagnetic metal, Gd(0001), has been studied in detail with the technique of time resolved photoemission, two-photon photoemission, and second harmonic generation (SHG)². The Gd sample was put into a magnetic field, while the incidence plane of the pump and probe beams was perpendicular to the magnetic

²Reference [47] and the reference there in

field. The time resolved photoemission spectrum was observed to change when the probe beam polarization was changed from s polarized to p polarized due to the non-coincidence between the spin polarization and the exchange splitting in the femtosecond dynamics [47]. A spin-flip process was invoked to explain this phenomenon [47]. Decaying cosine oscillations in the time resolved second harmonic generation curves, which have a frequency close to the zero wave vector longitudinal phonon frequency, were believed to be an effect of phonon oscillations despite their absence in the linear reflectivity response. The second harmonic oscillations of even symmetry with respect to the crystal orientation have the opposite initial phase to those of odd symmetry [48]. The oscillation of the even symmetry SHG is believed to be a direct result of phonon oscillation. Odd symmetry SHG oscillations are believed to be the result of coherent lattice and spin dynamic coupling via the exchange interaction J , which is amplified by surface effects [47, 48, 49]. These oscillations disappear when the center wavelength of the pump pulse shifts out of the resonant region. The dependence on pump pulse center wavelength, as well as the cosine like SHG signal suggests that the excitation mechanism of the coherent phonon is Displacive Excitation of Coherent Phonons (DECP). The driving force is the optically induced electron redistribution among the surface and bulk states of Gd (001). The damping of this coherent phonon has many different channels, for example, (i) the thermalized heat bath of electrons, phonons, or magnons, (ii) elastic scattering with defects, (iii) scattering with phonon and magnons, (iv) decaying with spin mode process, (v) excitation of electron-hole pairs. The details of their contribution is not very clear [47].

1.3.2 Applications of Ultrafast Spectroscopy in Semiconductors

Semiconductors are the most important materials in the electronics industry. Scientists have studied the dynamics of charge carriers and phonons in semiconductors with

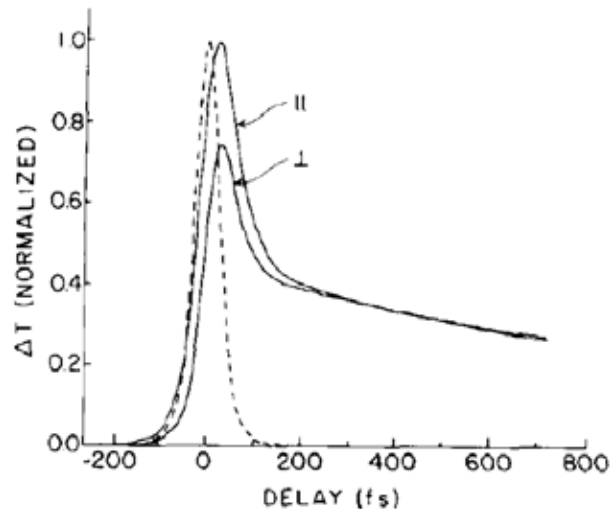


Figure 1.1: Pump-probe absorption saturation responses in GaAs, measured with the probe polarized either parallel or perpendicular to the pump. The dashed curve is the intensity of autocorrelation of the pump and probe pulse, which defines the zero delay. The curves were normalized by the slow decay part [50].

ultrafast spectroscopy [9, 10, 17, 51, 52, 53, 54, 55, 56, 57]. Lin. *et. al.* used transmission spectroscopy to study the relaxation of hot charge carrier in GaAs single crystals [18, 50, 58]. The transmission response curve has two parts: a fast decay and a slow decay as shown in Fig. 1.1. The slow decay process is believed to be the cooling process of excited charge carriers through electron-phonon interaction [50]. This is consistent with Schultheis's degenerate four wave mixing results [59]. The fast decay is due to scattering between the charge carriers and thermalizing in the Γ valley in the Brillouin zone. This explanation is consistent with experimental results by different probe photon energies as shown in Fig. 1.2. The ratio between the fast decay and the slow decay depends on the polarization geometry of the pump and probe beams, as well as the excitation density [50]. Parallel polarization has a higher ratio than cross polarization, and lower excitation intensities produce a higher ratio [50]. Charge carriers scattered to the L or X valleys are cooled by the electron-phonon interaction, then tunneled back to the Γ valley on a picosecond time scale [50]. If the probe photon energy is lower than the pump energy, charge carriers relaxed from the Γ valley, and scattered from other valleys, saturate the transition. The decay of the charge carriers

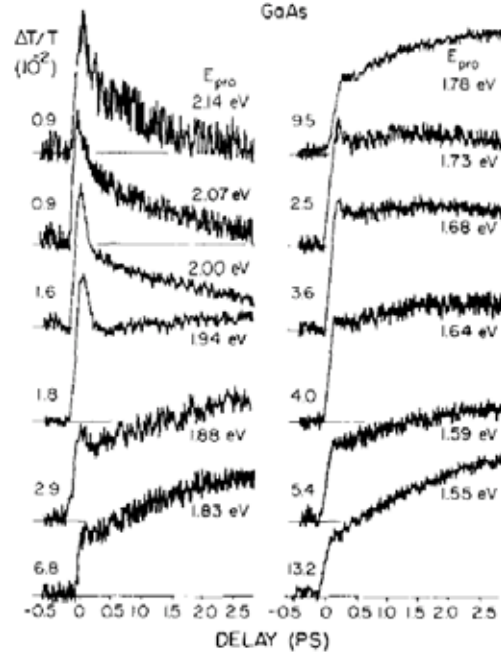


Figure 1.2: Absorption data for GaAs obtained with femtosecond probe pulses of different center wavelengths. The traces are displayed with arbitrary normalization for comparison of dynamics occurring at each probe energy. The actual amplitude of absorption saturation is indicated for each curve [50].

in the Γ valley and from the other valleys determines the slow change of the saturation process. Comparison between $\text{Al}_x\text{Ga}_{1-x}\text{As}$ and GaAs was used to explain this process [18]. Charge transport in quantum well structures has also been studied by ultrafast spectroscopy [60].

Kurz's group has used femtosecond reflectivity measurement to study phonon oscillations in GaAs and Ge crystals [61, 62, 63, 64]. The laser pulse duration was about 50 fs with 632 nm center wavelength. In their measurements, the coherent phonon exhibits a decaying sine or cosine oscillation in the reflectivity change curve as shown in Fig. 1.3. The initial phase of the phonon oscillations was not observed to be dependent on the polarization direction of the pump beam in GaAs within their measurement accuracy (5%). The phase and amplitude of the oscillation depended on the pump polarization in Ge. When the pump beam polarization was rotated by 90° , the phase was reversed. The phase and amplitude of the oscillation in the reflectivity change curve depend on the polarization direction of the probe beam in both GaAs and Ge crystal.

The amplitude of the phonon oscillation was found to be also related to the surface charge density of GaAs [63]. The excitation mechanism of this longitudinal phonon was believed to be a screening effect of the surface field by the photoexcited charge carriers [63], which was considered to be an special example of a displacive excitation of coherent phonon (DECP) mechanism [65]. In Ge, the phonon oscillation is sine-like, which suggests the excitation mechanism is transient stimulated Raman scattering (TSRS) near the impulsive limit [11, 62]. However, the theory of transiente stimulated Raman scattering predicts that the initial oscillation phase of absorptive material is not pure sine-like [11, 66]. In agreement with this prediction, the phonon oscillation in silicon does not have a pure sine or cosine phase [67].

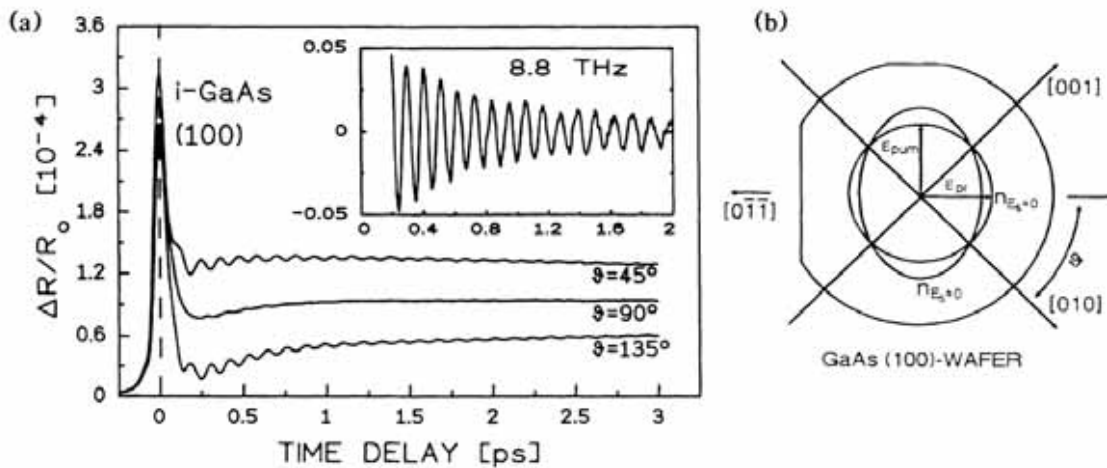


Figure 1.3: (a) Time resolved reflectivity change curve from (100) oriented intrinsic GaAs at an excitation density of $N = 10^{18} \text{ cm}^{-1}$ for orthorgonal pump and probe beam polarization. (b) The parameter θ is the angle between the probe polarization and the [010] crystal axis. Also shown is the projection of the index ellipsoid on the surface of an (100)-orientated wafer in the case of Zero and nonzero applied field in the [100] direction. [61]

Hase *et al.* have measured the reflectivity change in doped GaAs crystals with carriers densities of about $N = 10^{18} \text{ cm}^{-1}$. The time differential reflectivity change curves show oscillation beating, and the form of the beats changes with the pump intensity. These beats are mainly composed of two frequencies, 8.06 THz and 8.76 THz considered to be the transverse optical (TO) and longitudinal optical (LO) phonon

modes, respectively. With higher pump intensities, the TO mode is stronger than the LO mode, while with low pump intensity, the LO mode is stronger than the TO mode [68]. The frequency splitting between LO and TO modes is due to coupling between the LO phonon and a plasmon [69], which exists as a result of the interaction between the laser pulse and the sample surface. The local intensity of the laser pulse determines the frequency of the plasmon [60, 70] and the intensity gradient of the laser spot on the sample surface leads to the continuous spectrum of the plasmon. In the reflectivity change measurement, these frequency may be averaged out due to the integration of the whole spectrum [70].

Besides phonon oscillations, there are several other real time oscillations that have been measured by ultrafast spectroscopy, including Bloch oscillation, polarization beats, and quantum beats. Bloch oscillations exist in semiconductor superlattices while polarization beats are due to the interference (at the detector) of emitted fields, each from a two level system [10]. The quantum beats come from interference between two transitions excited by the laser pulse with a broader spectrum covering the difference of two transition energies [10]. All of these beats have periods of the order of picoseconds and can be measured by real-time four wave mixing (FWM) [10].

1.3.3 Applications of Ultrafast Spectroscopy in Oxide Compounds

Ultrafast spectroscopy has also been used to study some important oxide materials like ferroelectric and ferromagnetic materials, and superconductors. Temperature dependence of the pump-probe spectrum is a common measurement for the ferromagnetic materials, especially crossing the Néel temperature [14, 20, 71, 72, 73, 74]. The phase transition to the ferromagnetic state leads to a drop in the frequencies of coherent phonons or polaritons [14, 20]. The photoexcited charge carrier density is also affected by the temperature [73]. In hexagonal manganite LuMnO_3 , not only the frequency, but also the initial phase and the relaxation time of coherent acoustic phonons depend on the temperature, especially near the Néel temperature [14]. The extra change of

these parameters was explained by the coupling between these parameters and the ferromagnetic order [14, 20, 71, 72, 73, 74, 75]. The magnetic field dependency of these parameters is another method to understand the magnetic order [71]. Alignment and disordering of magnetic moments in photoexcitation of a charge- and orbital-ordered antiferromagnetic material was observed [74]. Magnetization in DyFeO_3 was controlled by a circularly polarized femtosecond optical pulse, which has an equivalent effect to a high magnetic field [76]. Terahertz radiation was observed from BiFeO_3 thin film which has a similar structure to DyFeO_3 [77].

The temperature dependence of pump-probe spectra of perovskite ferroelectric materials is also an interesting research field. Not only the relaxation of the photoexcited charge carriers, but also the frequency and the dephasing time of the coherent phonon depends on the temperature of the sample [12, 78, 79]. Polaritons have been observed at a frequency far below the frequency of phonons in some crystals, and this may be due to the intrinsic anharmonicity of the phonon or cross-anharmonic coupling between the different phonon modes [12]. The coherent soft phonon modes of $\text{Pb}_{1-x}\text{Ge}_x\text{Te}$ show large redshift and heavily over damped decay when the temperature approaches the phase transition temperature from the lower side. It disappears when the temperature is higher than the Curie temperature T_c [78]. A computational model has been built to simulate the transient behavior of the coherent phonon oscillation in LiTaO_3 [80].

The recombination time of Cooper pair electrons is of great interest as regards to the nature of high T_c superconductivity. In the experiment, the relaxation of photoexcited electrons in superconductors, such as $\text{YBa}_2\text{Cu}_4\text{O}_8$ or doped YBCO has been observed by pump-probe spectroscopy [8, 19, 81, 82, 19, 83]. The relaxation time increases as the temperature increases both below and above the phase transition temperature [83, 81, 84]. Dvorsek *et al.* found that the relaxation process of the $\text{YSr}_x\text{Ba}_{2-x}\text{Cu}_4\text{O}_8$ superconductor has two relaxation components, one associated with the superconducting transition and the other one with the pseudogap independent of the temperature [81]. Coherent phonons have been observed in the reflectivity change curves

of superconductors [81, 82]. Coherent phonon modes with different symmetries, relaxation times and associated with different metal ions have been observed with time resolved reflectivity change spectroscopy in $\text{YBa}_2\text{Cu}_4\text{O}_8$ superconductor [82]. Besides the study of nano-dots in semiconductors, pump-probe spectroscopy has also been used to study carbon nanotubes. Coupling between multiple coherent phonon modes was observed in carbon nanotubes [15].

1.4 Thesis Outline

The dynamics of electrons, phonons, and excitons is of the basic interest as regards to the nature of materials. Some of these effects can be observed from the shape of the regular spectrum, others may be too weak to appear on the spectrum, especially those associated with excited states. Ultrafast spectroscopy provides the possibility to observe these dynamics. Understanding the ultrafast dynamics may help us to develop the next generation electronics which works at terahertz frequencies.

In this thesis, we used pump-probe spectroscopy to study the ultrafast dynamics of ferroelectric LuMnO_3 , and semiconductors GaAs and Ge. LuMnO_3 is a hexagonal multiferroic material with an antiferromagnetic phase transition temperature at about 90 K, and a ferroelectric phase transition temperature at about 900 K. We used femtosecond pump-probe spectroscopy (FPPS) to excite and probe a manganese d-d transition and coherent optical phonon vibrations in a single crystal. An empirical shell model is used to calculate the normal modes of this material, and the relationship between the phonon modes and the ferroelectric phase transition are discussed. We also use FPPS to study coherent optical phonons in GaAs and Ge single crystals. Polarization analysis was used to analyze the excitation mechanisms of those coherent phonons. Ge and GaAs coherent phonons have different pump polarization dependencies. In Ge, the amplitude of coherent phonon oscillations purely depends on the pump polarization, which suggests that the excitation mechanism is purely the transient stimulated

Raman mechanism. In GaAs, the amplitude of the coherent phonon oscillations has two components, pump polarization dependent and independent components, which suggests that both the screening effect of photoexcited electrons and TSRS contribute to coherent phonon excitations.

In Chapter 2, experimental techniques and setups will be described in detail. In Chapter 3, we will discuss our experiments and results for GaAs and Ge. In Chapter 4, we will present our investigation of the ultrafast properties of LuMnO₃ crystal and discuss some related theoretical work. In chapter 5, we will summarize our findings, provide perspective on them and discuss the possible future direction in this field.

Chapter 2

Experimental Techniques

In this Chapter, I will start with a brief summary of some of the most important pump-probe techniques. In those techniques, the femtosecond pulse beam is employed as the pump pulse or to produce other kinds of pulses¹. In the second section, I will introduce some of our homemade devices and describe our experimental setup.

2.1 Pump-Probe Technique

In pump-probe techniques, a pulsed beam from the laser is split into two pulses; and both of them are directed to the sample on the same position. The optical path lengths of the two components are adjusted such that the pulse of one component (the pump beam) arrives at the sample first, followed by the pulse in the other beam (probe beam). The probe pulse is delayed with respect to the pump pulse by introducing an optical delay in its path or an optical advance in the path of the pump pulse. This form is also called degenerate pump-probe spectroscopy [10]. The time resolution is limited only by the pulse width of the laser. A common modification in the pump-probe technique is called non-degenerate pump-probe spectroscopy in which the pump and probe beam have different frequencies [10]. The frequency change is obtained by frequency doubling or optical parametric amplification in nonlinear crystals [14], which makes it easy to separate the probe beam from the scattered pump light by a filter. Other modifications, such as terahertz probing or electron pulse probing, have also been realized.

¹The femtosecond laser pulse is produced by Kerr-lens mode-locking. This method is described in Appendix A and references therein.

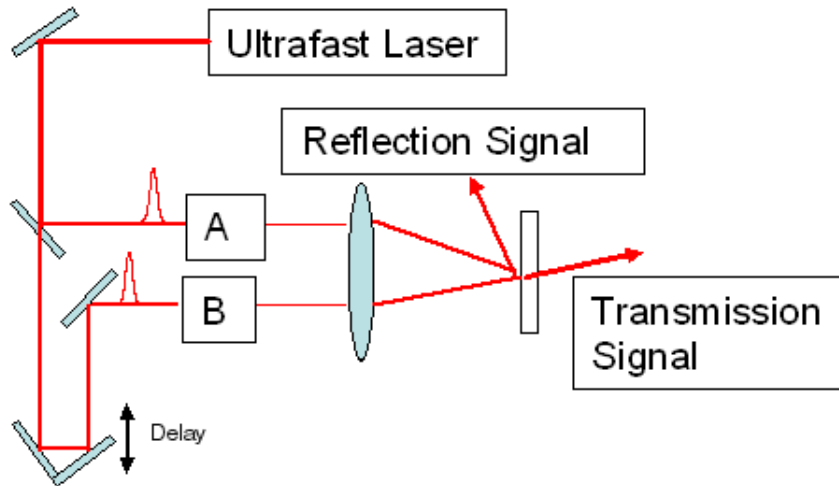


Figure 2.1: Schematic diagram of generic two beam experiment setup. This setup can be used as pump-probe reflection or transmission spectroscopy. In the schematic, boxes A and B may contain nothing, or frequency doubling/tripling crystals, or optical parametric amplifier and polarization optics.

The most straightforward way to measure the pump-probe effect is to measure the reflected or transmitted probe intensity. Fig. 2.1 is a schematic diagram of the pump-probe transmission and reflection spectroscopy setup. In the degenerate pump-probe technique, polarization adjustment devices may be put in the position of boxes A and B in the schematic diagram. In the non-degenerate measurement, more devices are put in the position of boxes A and B. They can be either a frequency doubling/tripling crystal or an optical parametric amplifier. In general, the pump beam always has higher intensity than the probe beam. In transmission/reflection spectroscopy, the change in the transmission/reflectivity is measured. Due to the low signal level, the average of a large number of measurements is used to increase the signal-to-noise ratio. Chopping the pump beam and lock-in detection of the transmitted or reflected probe beam are good choices to increase the signal-to-noise ratio too. In some of the experimental setups, pump and probe beam are chopped at different frequencies, and the pump-probe signal is detected by lock-in amplifiers at the sum or difference frequencies. The time resolution is defined by the pulse width of the laser beam at the position of the sample. Thus, the detector for the reflectivity and transmission does not need to have a

very fast response. The change in the reflectivity or transmission is always normalized by the reflectivity or transmission.

$$\frac{\Delta R}{R_0} = \frac{R - R_0}{R_0} \text{ or } \frac{\Delta T}{T_0} = \frac{T - T_0}{T_0} \quad (2.1)$$

Here, T, R are the transmission and reflectivity, respectively. ΔT and ΔR represent the change in the transmission and reflectivity, respectively. T_0 and R_0 are the transmission and reflectivity without the pump beam.

Another way is to measure the spectral change in the reflected or transmitted probe. As the time delay between the pump and probe beam changes, the spectrum of the reflected or transmitted probe beam may change. Recording the spectrum as a function of pump-probe delay can uncover the microscopic change in the material. Methods to measure the pulse width are autocorrelation, and frequency-resolved optical gating (FROG). They are introduced in details in Appendix A. Minimizing noise is the most important object in all of those detection methods.

2.2 Experimental Setup

Our pump-probe experimental setup is built for transmission/reflection spectroscopy. Our experiments are mainly focused on reflection spectroscopy. We proceeded with two kinds of reflection measurements: total reflectivity change and differential reflectivity change.

2.2.1 Pump-probe Reflection Spectroscopy

Our femtosecond pulse laser is a Mini Ti:Sapphire Laser (Model MTS, Kapteyn-Murnane Laboratories L.L.C.), pumped by a diode pumped, frequency doubled continuous wave (CW) Nd:vanadate laser (VerdiTM V-5, Coherent INC.). After the fs laser beam is emitted, the pulses are compressed by a pair of extra-cavity prisms². The laser beam enters

²A detailed description is available in Appendix A.

our pump-probe system as shown in Fig. 2.2. First, the laser pulse passes through a thin plate polarizer (less than 1 mm thickness) to ensure the horizontal polarization direction. Then the beam is split into two parts at a ratio of 15:85 by a thin plate beam splitter (less than 1 mm thickness). The weaker part passes through retro reflector 2,

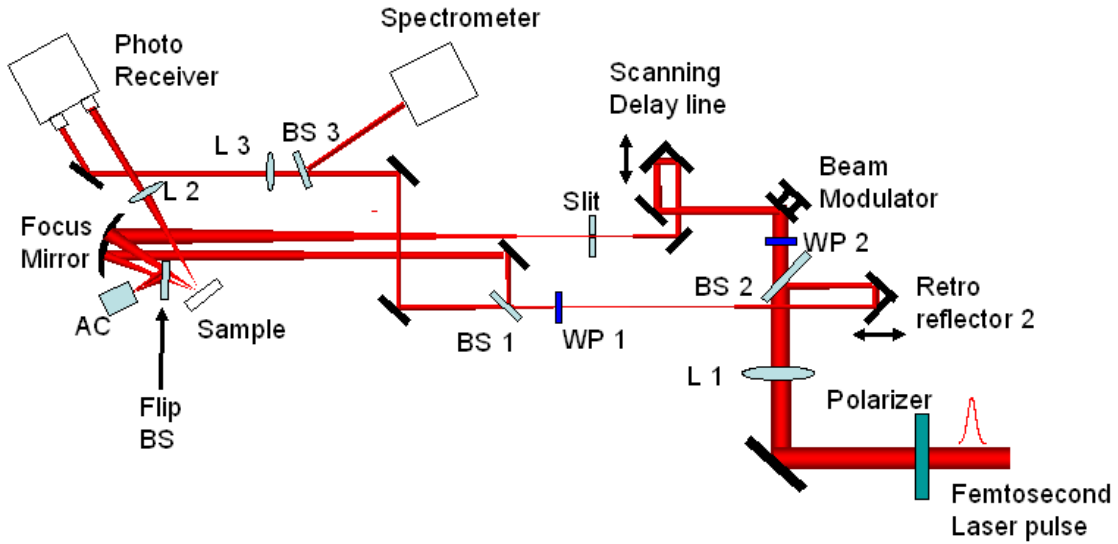


Figure 2.2: Schematic diagram of reflectivity change measurement. In the figure, L, BS, and WP represent lens, beam splitter, and half wave plates, respectively. AC is the autocorrelation diode.

which is mounted on a translation stage. We can change the delay between pump and probe pulses manually by adjusting the translation stage. Then the beam passes a half wave-plate (WP1) for polarization adjustment, and is equally split into 2 parts. One part is used for the probe beam, the other is used for reference of detection and spectrum monitoring. Here, a USB2000 spectrometer from Ocean Optics has been used to monitor the spectrum.

The other part of the beam with higher intensity is the pump beam. It passes through another half wave-plate (WP2), and is reflected by a mirror on a home-built piezo-electrically driven mechanical oscillator³. This oscillating mirror can sway the beam 0.8 degree horizontally, and in conjunction with a narrow slit serve as an optical

³The structure and the function of this device is introduced in Appendix B

modulator. Then, the beam is directed into a scanning optical delay line (ODL-150, Clark-MXR Inc). After the beam exits the delay line, a vertical optical slit is used to modulate the intensity of the beam in conjunction with the oscillating mirror. The position of this slit is at the beam waist of lens L1. If the laser beam enters the delay line not precisely parallel to the scanning direction, the laser beam is translated sideways upon scanning of the delay line. This beam walking is monitored by a home made position sensitive photodetector whose function block diagram is shown in Fig. 2.3. Before we align the scanning direction of the delay line, we set the position sensitive photodetector at a position between the slit and the focusing mirror, and the pump beam is directed into the center of the position sensitive photodetector. Then we minimize the output of the position sensitive photodetector by gently adjusting its position. Finally, we align the scanning direction of the delay line until the oscillatory signal due to the scanning is below the noise of the position sensitive detector.

Both the pump and probe beams are focused onto the surface of the sample with the same focusing mirror. We adjust the beam incidence direction to let the pump beam and the probe beam focus onto the same point. An autocorrelation measurement⁴ was performed to monitor the overlap of the two pulses in time and space. The position of the autocorrelation diode⁵ is at the mirror position of the sample through a flip-mounted beam splitter. When the autocorrelation peak is maximized, two beams have their best overlap in space. Since the pump beam is focused when it passes through the delay line, the focal point of the probe beam moves along the beam direction when it scans in a large scale. The intensity of the pump beam at the point overlapping with the probe beam will thus change. However, as a result of careful alignment, the intensity change of the pump in our experiments is much less than 1 %⁶.

⁴We will introduce this measurement in detail in Appendix A.

⁵The photodiode only response to the photon with wavelength ranging from 300nm to 600 nm, which means the output current of the photodiode is excited by two photon effect of our laser beam.

⁶In the experiment, the focal length of the mirror is 100 mm and the distance from the slit (the focused point of Lens L1) to the focusing mirror is about 650 mm. The beam diameter at the sample surface is

The reflected probe beam is measured by a Nirvana auto-balanced photoreceiver

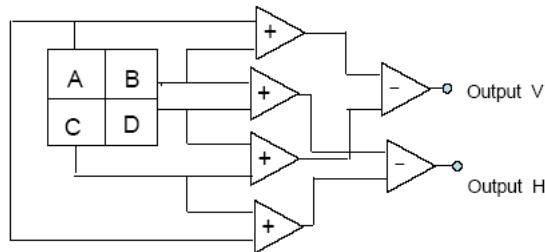


Figure 2.3: Function block diagram of the position sensitive photodiode. The photodiode has four sections which have independent photocurrent output. The photo-current of each section of the diode is proportional to the incident laser power. The output V and output H can represent the offset of the laser spot on the photodetector. The oscillation of the output means the walking of beam in the horizontal or vertical direction.

(Model 2007, New Focus) after it is collimated by a lens. Another collimated beam which does not pass the sample is used as the reference of the auto-balanced photoreceiver. A lock-in amplifier (SR830 from Stanford Research Systems, Inc.) is used to pick out the pump-probe signals. Fig. 4.1 is a photograph of the optical bench layout for the reflectivity change measurement.

2.2.2 Differential Reflection Pump-Probe Spectroscopy

The excitations induced by the pump pulse may result in different optical property changes in different polarization directions. Differential reflection spectroscopy measures the difference of the optical property changes among different polarization directions. In this measurement, the polarization direction of the probe beam is kept at

about $50 \mu\text{m}$, the distance from the sample to the focusing mirror is about 118 mm, the diameter of the laser beam on the focusing mirror is about 5 mm. The relation between the beam diameter d and the distance from its waist z can be written as

$$\frac{d^2(z)}{0.05^2} - \frac{z^2}{1.18^2} = 1$$

1 % of the intensity change means 1 percent of beam diameter square change. This means that the focus position can move back and forth 0.12 mm. This allows the focus point of L1 can move front or back 0.67 mm. In other words, a 2.2 ps scanning range of the delay line only change 1% of the beam intensity compared to the highest intensity. If we set the highest intensity point in the center of scanning range, 4.4 ps delay can be used.



Figure 2.4: Photograph of the optical bench layout for the reflectivity change measurement

45° to the horizontal direction, and the difference of reflectivity change between the vertical and horizontal polarization component is measured.

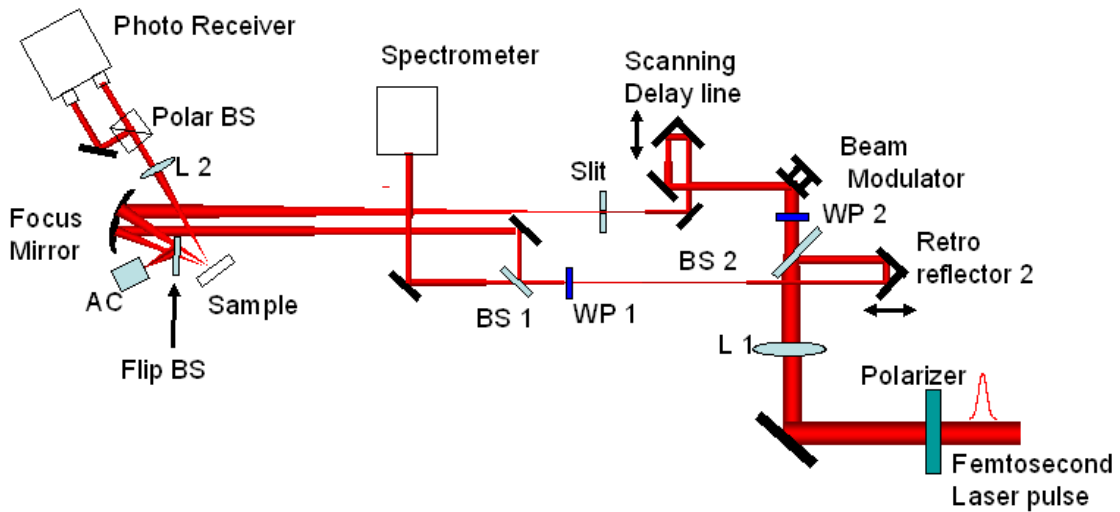


Figure 2.5: Schematic diagram of differential reflectivity change measurement. In the figure, L, BS, and WP represent lens, beam splitter, and half wave plates, respectively. AC is the two-photon autocorrelation diode.

Fig. 2.5 is a schematic diagram of our experimental setup. In comparison with Fig. 2.2, the only difference is the optical path after the sample. After reflection from the sample and collimation by a lens, the probe laser beam is split into two components

by a polarizing beam splitter. The horizontally polarized component goes to the signal sensor of the photo receiver while the vertically polarized component goes to the reference sensor of the photo receiver. We can obtain the differential reflectivity change by setting the photo- receiver to the "balance" mode. We also can study the pump dependency of the differential reflectivity change by rotating the polarization of the pump beam.

2.2.3 Pump-Probe Transmission Spectroscopy

In transmission spectroscopy, the detector measures the change in the transmission induced by the pump pulse. This requires that the sample is transparent, which may be realized for absorbing materials by using a thin film. In the experimental setup, we move our photoreceiver to a position where the transmitted beam passes. In this spectroscopy, total or differential transmission changes can be measured. Fig. 2.6 is a

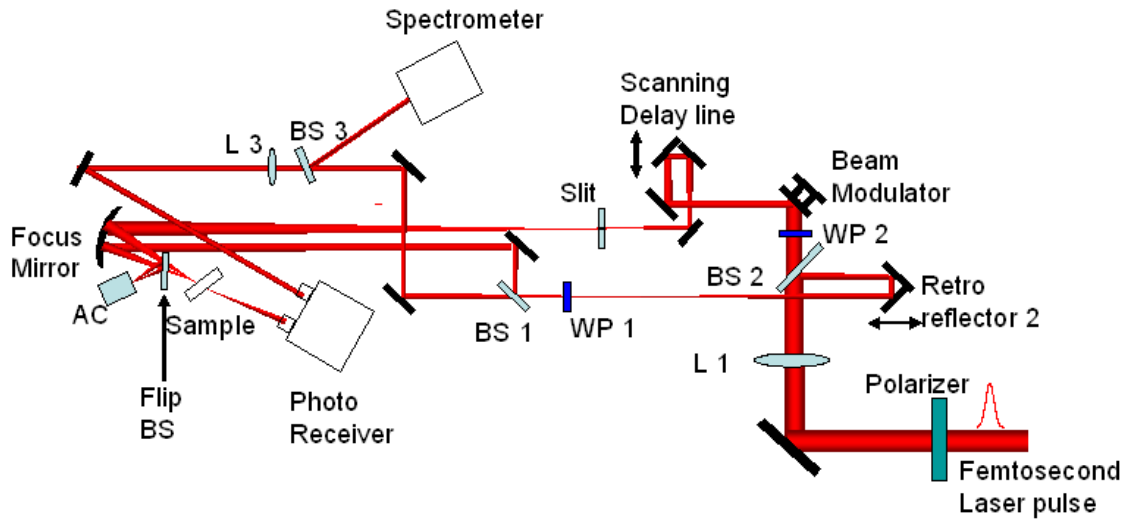


Figure 2.6: Schematic diagram of transmission change measurement. In the figure, L, BS, and WP represent lens, beam splitter, and half wave plates respectively. AC is the two-photon autocorrelation diode.

schematic diagram of the transmission spectroscopy that we have used to measure dye-sensitized TiO_2 nanoparticales and thin films. The transmitted probe beam is directed

onto the signal sensor of the photo receiver, while a beam which does not pass through the sample is directed onto the reference sensor of the photo receiver. The output of the photo receiver is the time resolved transmission change. In this measurement, the sample is always mounted on a transparent substrate.

2.3 Calibration of Initial Phase

In principle, the autocorrelation peak measured by the nonlinear photodiode should define the zero delay time. However, we also found that the autocorrelation peak time shifts by an amount as large as 8 fs when we move the photodiode in the direction of the pump and probe beam, even though we do not change the optical path of the pump and probe beams. This may be caused by the difference between the incidence angle of pump beam and that of probe beam. This means that the zero delay time on the sample also shifts when the sample moves back and forth, and the way we define zero delay time has a measurement error as large as 11 fs, which is about $1/8$ period or 0.8 radian of the GaAs or Ge optical phonon. However, if we do not move the sample nor readjust the optical geometry, this error is a systematic error in a whole set of data. If we calibrate the initial phase of one reflectivity curve in a set of experiments, we can therefore calibrate the whole set of data.

In the experiment, the initial phase of the phonon oscillation in GaAs does not depend on the pump power when the pump beam is polarized in the [010] direction (see Section 3.2.3). The probe beam has the same intensity and polarization as the pump beam. If we now interchange the role of pump and probe beams, we should obtain the same results; in particular, the initial phase of the phonon oscillation should be unchanged. Based on this idea, we set the pump and probe beam polarizations along the GaAs [010] crystal axis direction with equal intensity. After focusing both beams onto the same spot of the sample surface, we measured the reflectivity change of one beam while chopping the other. We then exchanged the beam for reflectivity

measurement and chopping. Then we varied the nominal zero of delay, searching for a point where the phonon oscillations in both curves have the same initial phases. This point must be the true point of zero delay. It turned out close to the autocorrelation peak. The initial phase we obtained in this way is for GaAs $0 \pm 4^\circ$, which was used to calibrate the initial phases that we measured in the other experiments.

For Ge, if the pump beam is polarized along [010] or [100] directions, we can not excite the coherent phonon due to the symmetry of the Raman tensor. However, the initial phase of the Ge phonon does not depend on the pump polarization. So changing the polarization of the pump and probe beam will not change the initial phase of the phonon oscillations. We set the pump beams polarized along the [110] axis and the probe polarized along the [010] axis. We then measured the differential reflectivity of the probe beam while chopping the pump beam. After we obtained the pump-probe spectrum, we exchanged the polarization of both beams by rotate the half-wave plates by 22.5° . Then, we measured the differential reflectivity of what used to be the pump beam by chopping what used to be the probe beam. By setting zero delay time at a point of time where both reflectivity curves have the same initial phases of phonon oscillation, we obtained the initial phase of the phonon oscillations in Ge crystal as $102 \pm 15^\circ$. This value was used to calibrate the initial phase of all phonon oscillations of Ge crystal.

Comparing with the period of the phonon oscillation in LuMnO_3 , the systematic error on the zero delay time is small. So we did not calibrate the zero delay time beyond the value given by the autocorrelation peak when we measuring pump-probe spectra in LuMnO_3 .

Chapter 3

Femtosecond Spectroscopy of Polar and Non-Polar Semiconductors

This chapter describes my research on semiconductor crystals. I will start with a brief introduction into the history of time resolved measurements on semiconductors, as well as the properties of GaAs and Ge. In the second and third sections, our experiments on GaAs and Ge crystals will be described in detail. Data analysis, results discussion, as well as conclusion will be discussed.

3.1 Introduction

Semiconductors are one of the most important material classes in modern technology. Most of modern electronics are made of semiconductors. Electro-optic devices are also made from semiconductors. As the working frequency of electronics and optical devices becomes higher and higher, it is necessary to study the ultrafast real time response of semiconductors.

3.1.1 Structure and Optical Properties of GaAs and Ge

Gallium arsenide (GaAs) is an important semiconductor for devices such as microwave frequency integrated circuits, infrared light-emitting diodes, laser diodes and solar cells. The left panel in Fig. 3.1 shows a ball-and-stick model of the Zincblende GaAs crystal structure; the lattice parameter a_0 at 300K is 0.565 nm and the bond length between the Ga and As is 0.2448 nm [86]. The right panel in Fig. 3.1 is the calculated band structure of GaAs [85]. The measured direct band gap of this crystal is 1.424 eV

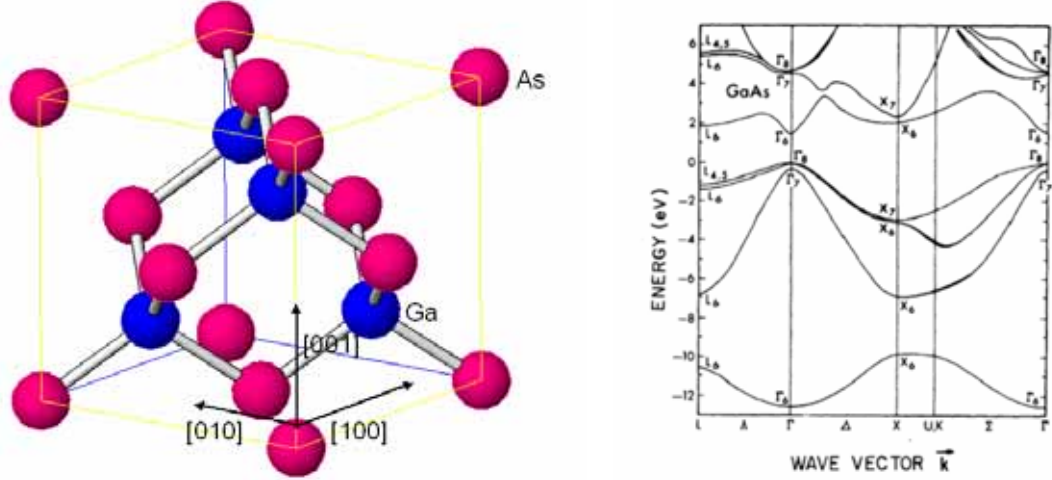


Figure 3.1: The left panel is the ball-and-stick model of the GaAs crystal structure. The pink balls represent As atoms, and the blue ball represents Ga atoms. The sticks represent covalent bonds. On the right is the band structure of the GaAs crystal adapted from reference [85].

T_d	E	$8C_3$	$3C_2$	$6S_4$	$6\sigma_d$
A_1	1	1	1	1	1
A_2	1	1	1	-1	-1
E	2	-1	2	0	0
T_1	3	0	-1	1	-1
T_2	3	0	-1	-1	1
Total in GaAs	6	0	2	0	2

Table 3.1: Character table of the T_d point group, which is the point group of the $P\bar{4}3m$ space group of the GaAs crystal, the last row is the total character for general coordinate displacement at the Γ point, which can be decomposed into $1A_1 + 1E + 1T_2$

at 300K [86]. Table 3.1 shows the character table of T_d point group of GaAs crystal. To obtain the phonon modes of the crystal, we calculated the total characters of vibrations at the Γ point in GaAs crystal from the cartesian coordinates displacements. The result is shown in the last row of the table. The total characters can be decomposed into $1A_1 + 1E + 1T_2$. All of these three vibration symmetries are Raman active. A_1 and E modes are acoustic phonons, and the T_2 mode is an optical phonon mode. The

Raman tensor of this mode can be expressed as follows [11]:

$$T_2 : \begin{pmatrix} 0 & 0 & c \\ 0 & 0 & 0 \\ c & 0 & 0 \end{pmatrix} \quad \begin{pmatrix} 0 & 0 & 0 \\ 0 & 0 & c \\ 0 & c & 0 \end{pmatrix} \quad \begin{pmatrix} 0 & c & 0 \\ c & 0 & 0 \\ 0 & 0 & 0 \end{pmatrix} \quad (3.1)$$

This means that when the light is polarized in the [100] or [010] direction, the Raman scattering cross-section is zero with the condition that light is incident and scattered along the [001] direction. When the probe beam is polarized in the crystal graphic [110] or [1-10] directions, it has the maximum cross-section to measure the oscillation of the phonon. Due to lack of inversion symmetry, the GaAs crystal exhibits a linear electro-optic effect. The electro-optic coefficients are of the form:

$$r_{ij} = \begin{pmatrix} 0 & 0 & 0 \\ 0 & 0 & 0 \\ 0 & 0 & 0 \\ r & 0 & 0 \\ 0 & r & 0 \\ 0 & 0 & r \end{pmatrix} \quad (3.2)$$

Here, i represents directions of the electric fields (x, y, z), and the j represents the refractive index ellipsoid change coefficient (x^2 , y^2 , z^2 , yz , zx , and xy). When the electric field is in the z direction, the refractive indexes in x+y and x-y directions change in opposite directions, and vice versa¹. The electro-optic constant $r = 1.6 \times 10^{-10} \text{ cm/V}$ [70].

The germanium crystal has the diamond structure, which is similar to that of GaAs, but only composed one kind of atom. The left panel of Fig. 3.2 shows the ball-and-stick model of Ge. The lattice parameter at 300 K is 0.566 nm and the nearest neighbor distance is 0.245 nm [89]. The right panel of Fig. 3.2 shows the calculated band structure [85], and the indirect band gap from the top of the valence band to the bottom

¹The electro-optical effect is explained in detail in reference [87] and reference [88]

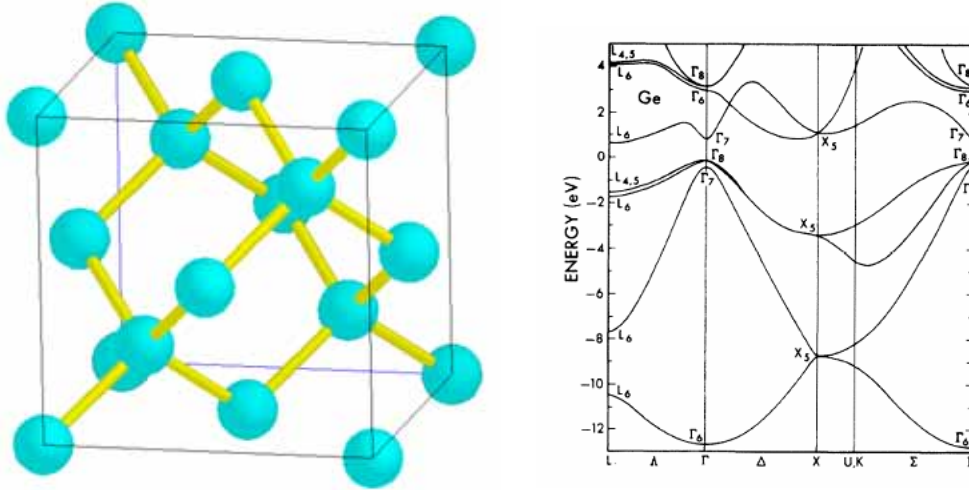


Figure 3.2: The left panel is the ball-and-stick model of Ge crystal structure. The sticks represents the valence bond. The right panel is the calculated band structure of Ge, which is from reference [85].

of the L valley is 0.66 eV at 300 K and the calculated gap from the top of the valence band to the bottom of Γ valley is 0.80 eV [89]. Compared with GaAs, the Ge crystal is only made of Ge atoms and has inversion symmetry. This $Fd3m$ space group, O_h point group crystal has A_1 and an E symmetry acoustic phonon, and a T_{2g} symmetry optical phonon. The optical phonon has the same Raman tensor as that of GaAs (Eq. 3.1). Due to the inversion symmetry, the germanium crystal does not exhibit the linear electro-optic effect.

3.1.2 Ultrafast Time Resolved Measurements of Semiconductors

Many ultrafast spectra of semiconductors have been reported in the past twenty years. The experimental methods include time resolved transmission spectroscopy [18, 50, 58, 90, 91], time resolved reflectivity change [62, 92, 93, 94, 95, 96, 97], spectrally resolved four-wave-mixing (FWM) [5, 6, 98], and time-resolved FWM [59, 99, 100, 101, 102]. Transient FWM signals are determined by photo-excited electron populations as well as photo-excited polarizations. When the experiment is performed at very low temperatures (a few K), the coherent exciton oscillation appears as beats with a beat period of

about 1 ps on the time resolved FWM curves [5, 6, 10, 59, 98, 99, 100, 101, 102]. Pump-probe spectroscopy (time resolved reflectivity change and time resolved transmission spectroscopy), whose signal is determined by the coherent and incoherent response of the sample, is used for measuring photoexcited carriers and coherent phonons over a large range of temperatures.

In the late 1980's, Lin *et al.* measured pump-probe transmission spectra of GaAs with 2.0 eV pump photon energy [18, 50, 58]. The transmission change curve has two components: a fast decay with a decay time of less than 30 fs and a slower decay-ing process with an exponential decay time of 1.5 ps. The shape of the fast decaying component can be obtained by convoluting the autocorrelation with an exponential decay [50]. The decay time decreases as the photoexcited carrier intensity (proportional to the pump intensity) increases [50, 58]. The strength of this component depends on the angle between polarizations of the pump and probe beam. When the pump polarization is parallel to the probe polarization, this component has a maximum contribution to the transmission change curve; it contributes minimally when the pump polarization is perpendicular to the probe polarization [50]. The slow decay is believed to be a process where the photoexcited charge carriers relax back through electron-phonon interactions [58]. The reflectivity changes due to the photoexcited charge carriers also depend on the crystal orientation [61, 63]. When the excitation intensity is high, the reflectivity difference between GaAs [110] and [-110] crystal axes have a fast change in the first few femtoseconds, which is followed by an exponential decay. When the photoexcitation intensity is low, the differential reflectivity increases slowly [64, 103]. This is attributed to the much larger distance the photoexcited carriers have to travel before they can screen the surface field [64].

Time resolved phonon oscillations were observed in GaAs after signal averaging had been performed over 10^5 successive scans [61]. The initial phases of these oscillations were reported as 0 or π , with oscillations measured from the [110] and [1-10]

axes having opposite initial phases [61]. When the photoexcited charge carrier intensity or surface charge density increases, the phonon oscillation initial amplitude in the differential reflectivity change curve also increases [63]. As the dopants in the semiconductor changes from n type to p type, the differential reflectivity is changed from positive to negative [64]. Dekorsy *et al.* described the excitation mechanism as the screening effect of the photoexcited charge carriers. The pump beam excites the electrons from the valence bands to the conduction bands [64]. The high concentration of photoexcited electrons and holes screens the surface electric field and thus reduces the electrostatic forces exerted on the ions. The corresponding changes in the equilibrium position of the ions drives the lattice to vibrate [64]. Photoexcitation of coherent plasma oscillations results in noticeable oscillations in the reflectivity. The plasma frequency depends on the density of the excited charge carriers. In pump-probe experiments, the laser beam is focused onto a small spot with a Gaussian intensity distribution. Thus, the plasma frequency varies spatially across the irradiated spot. If we average all these frequencies with their appropriate weights, the result will be a broad spectrum, similar to white noise. Thus, due to frequency averaging the plasma oscillations cancel out [70, 104]. Phonon oscillation beats due to the coexistence of both TO and LO phonons were observed in n-doped GaAs [68, 69]. Coherent phonon oscillations were also observed in the reflectivity of Ge [62]. The excitation mechanism was believed to be impulsive stimulated Raman scattering [11, 62]. The phonon oscillations of silicon were observed in the differential reflectivity curve [67] with an initial phase close to π [67].

3.2 Pump-Probe Spectroscopy of GaAs

3.2.1 Pump-Probe Effects in GaAs

The intrinsic GaAs wafer used in this study was polished when it arrived from a commercial company. It was measured in atmosphere at room temperature. The measurement setup is described in detail in Section 2.2.1. The incidence angle of both pump and probe beam was about 5° to the normal direction of the sample surface while the angle between the pump and the probe beam was also about 5° . In the experiment, the $[110]$ and $[001]$ axes of the sample were set horizontally while the $[-110]$ axis was set vertically. The solid blue line in Fig. 3.3 represents the reflectivity change when the

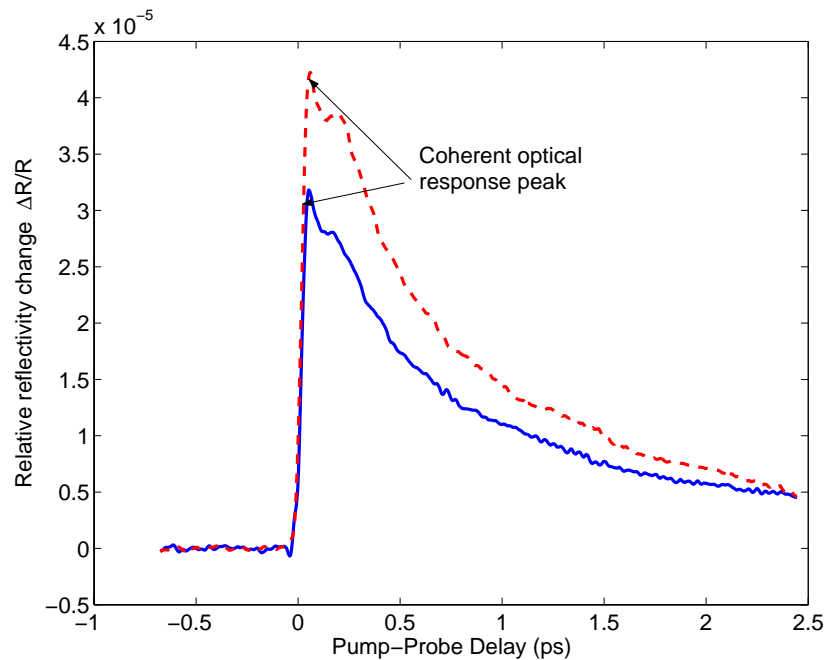


Figure 3.3: Reflectivity change curve measured from the (001) surface of intrinsic GaAs. The pump polarization was set along the $[110]$ direction. The solid blue curve is obtained with the probe beam polarized along $[110]$ and the red dash curve is obtained with probe beam polarized along $[1-10]$

probe beam was polarized horizontally. The pump beam was polarized at 45° to the vertical. The red dashed line in Fig. 3.3 represents the reflectivity change when the probe beam was polarized in the vertical direction. In our system, the pump photon

energy is around 1.55 eV, which is higher than the direct band gap of GaAs, from the top of the valence band to the bottom of the Γ valley, but it is lower than the energy gap from the top of the valence band to bottom of any other valleys. So the relaxation channel that the photo-excited electrons are scattered to other valleys can be excluded. The relaxation channel is only through phonon-electron scattering in Γ valley [18, 50, 61]. The decay time in this process is in the order of ps. We also noticed that there is a sharp peak at zero delay time. We attribute this peak to the coherent optical response. When we compare these two curves, we notice that the heights of the peaks are dif-

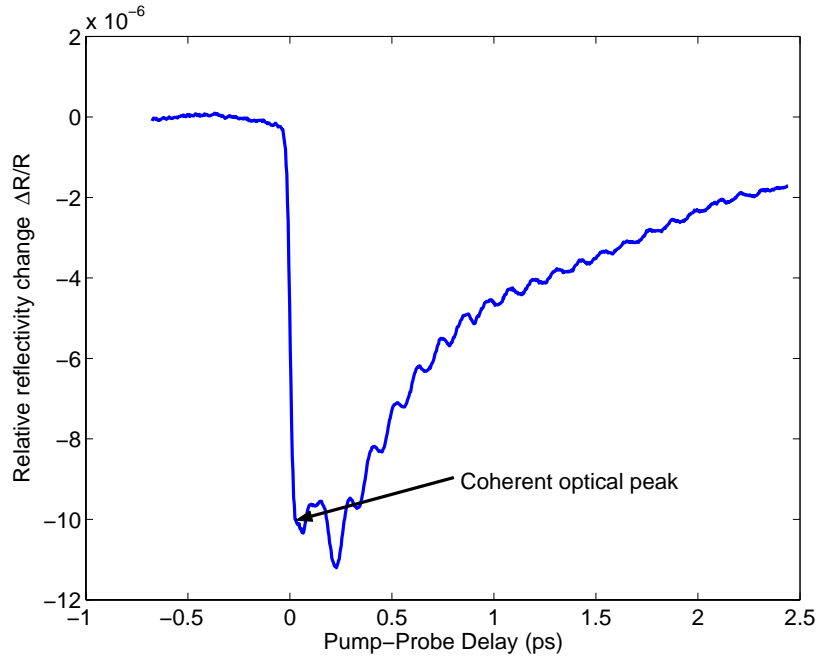


Figure 3.4: Differential reflectivity change measured from the (001) surface of intrinsic GaAs. The pump polarization was set along [110] direction (horizontal). The probe beam was polarized at a 45 degrees angle to the horizontal. The result was obtained by measuring the difference between the horizontal and vertical components of the reflected probe beam.

ferent. Besides the decaying behavior, which is attributed to the relaxation of charge carriers, there are some very weak oscillations on these two curves. These oscillations may be due to the coherent optical phonon. To observe these oscillations clearly, a

differential reflectivity measurement was performed ². The probe beam was polarized at a 45 degree angle to horizontal. After it was reflected from the sample, it was split into horizontal and vertical components, and their difference was recorded. The benefit of this measurement is that the hot-charge carrier effect is mostly canceled. However, since the 4-fold rotational symmetry is broken by the surface field, this cancellation is not complete. Fig. 3.4 shows the results obtained from the differential measurement. When the excited charge carriers relax back to the valence band, screening of the band bending surface field decreases. Therefore, the difference of the refractive index change between [110] and [-110] also decreases. It has the same decay constant as that of the curves in Fig. 3.3. The reflectivity change due to the phonon oscillation is very obvious. The frequency of the phonon is 8.8 ± 0.2 THz with a decay time of about 2.2 ps. The bulk Raman LO frequency 8.6 THz [86] is in the range of error bar of our measured value.

3.2.2 Pump Polarization Dependence of Phonon Oscillation

In the Fig. 3.4, there are 3 kinds of features: A coherent optical peak, a slow decay, and coherent oscillations. To gain insight into the excitation mechanisms of the coherent

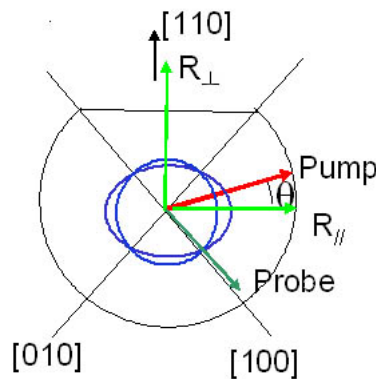


Figure 3.5: Pump beam polarization geometry.

phonon, we measured the pump polarization dependence of the reflectivity changes.

²Experimental methods are described in details in Section 2.2.2

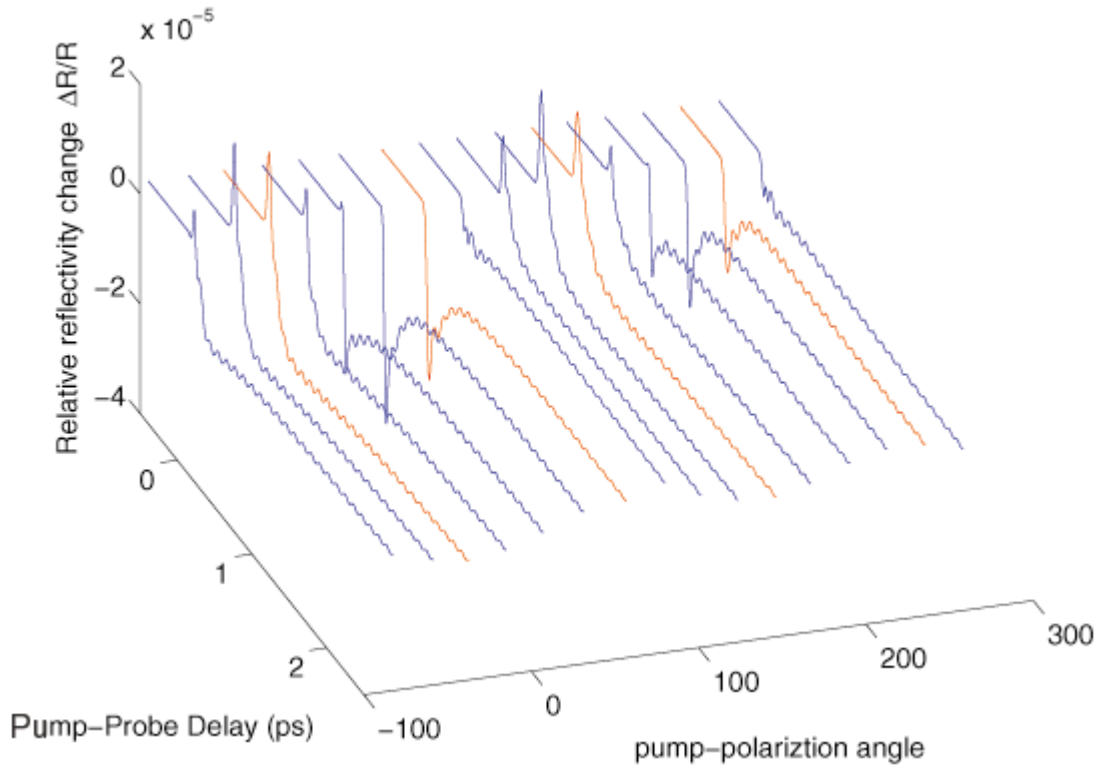


Figure 3.6: GaAs pump polarization dependence in the reflectivity change. The pump polarization angles are -90° , -66° , -45° , -22° , 0° , 24° , 49° , 72° , 94° , 117° , 139° , 160° , 183° , 205° , 228° , 250° .

The probe beam was set at 45 degrees with respect to the horizontal as shown in Fig. 3.5. The power of the pump beam was about 20 mW. We rotate the pump polarization direction and measured the pump-probe spectra at various angles. The angle between the pump polarization and the crystallographic [110] direction is shown in Fig. 3.5. The resulting differential pump-probe spectra are shown in Fig. 3.6. In Fig. 3.6, the step-function-like initial signal is believed to be due to screening of the surface charge by photogenerated carriers. The sharp peaks at zero delay are due to the coherent optical response. The coherent optical response peak is the nonlinear optical coupling between the pump and probe fields via the optical Kerr effect.

After subtracting the slowly varying components of the signal, the oscillations due to the optical phonon could be studied in more detail. An exponentially decaying

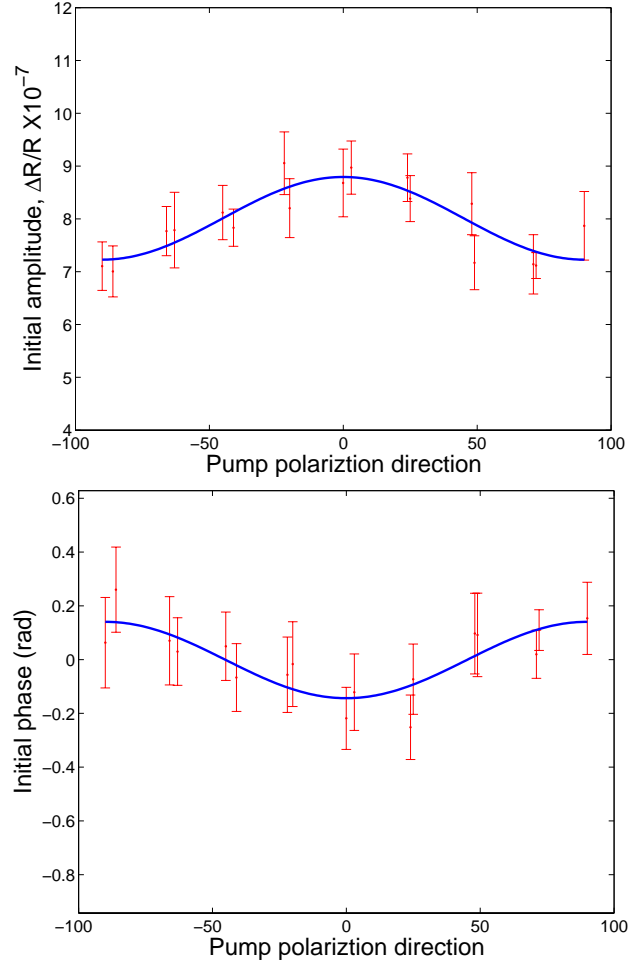


Figure 3.7: Dependence of the amplitude and phase of the coherent phonon oscillations on the pump beam polarization angle. Zero degree means that the pump beam polarization is parallel to the $[1-1\ 0]$ direction.

cosine function (Eq. 3.3) was used to fit these oscillations.

$$\Delta R/R = A \cos(\omega t - \phi) \exp(-\gamma t) \quad (3.3)$$

The fitting parameters A (the initial phonon oscillation amplitude) and ϕ (the initial phonon oscillation phase) varies with pump beam polarization with a period of 180° ³. These parameters are plotted in one period, from -90° to 90° , in Fig. 3.7. The initial

³The change of amplitude and the phase can not be induced by the change of the overlap of the pump and probe beams or the drift. The drift only changes in one direction as the time goes on. If the change is induced by the overlap change due to adjustment of the polarization of the pump beam, the period will be larger than 180° . If the two surface of the half wave plate is not parallel, this will induce with 720° period. If the rotation stage were not smooth, it would not resulted in a periodic change.

amplitude can be fit as $A(\theta)=(8.0+.8\cos(2\theta))*10^{-7}$ where θ is the angle between the pump beam polarization and the horizontal direction or crystal [110] axis. The initial phase can be fitted as $\phi=-0.05\cos(2\theta)*\pi$. The initial oscillation amplitude changes by about 20% and the initial phase shifts by 0.1π when we rotate the pump polarization from [110] to [1-10].

3.2.3 Pump Power Dependence of Phonon Oscillation

The pump power dependence also has been investigated. First we set the pump polarization direction along crystal [010] axis. The differential reflectivity was measured between [110] and [1-10] probe polarization components. In this set of experiments, the pump beam power intensity was 4.0, 9.0, 13.5, 19.0, and 23.5 mW in a focused spot size of 0.1 mm diameter. The resulting differential reflectivity change curves are shown in Fig. 3.8. As the pump power increases, the exponential decay of the reflec-

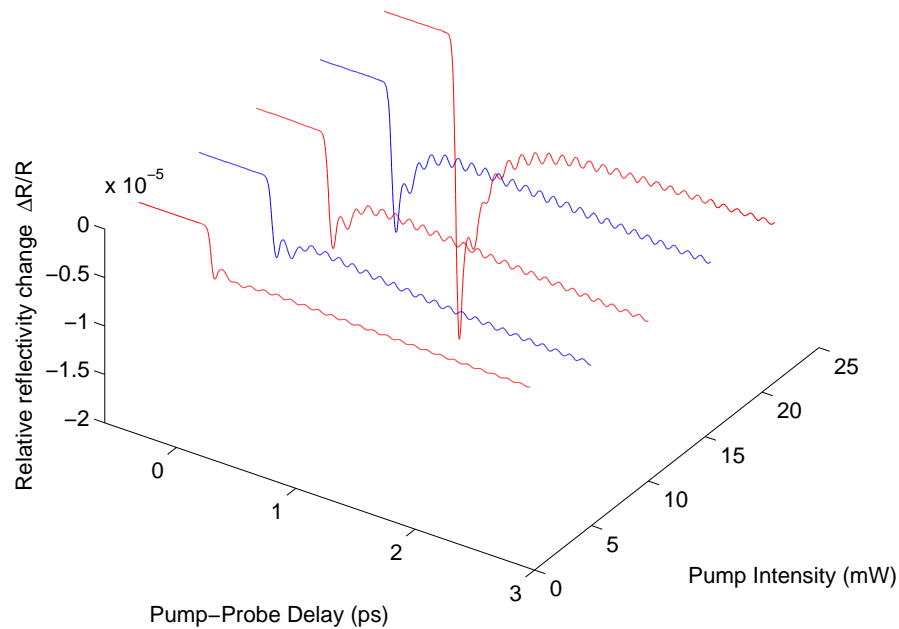


Figure 3.8: Pump intensity dependence in reflectivity changes. The pump intensity has been set at 4.0, 9.0, 13.5, 19.0, and 23.5 mW. The pump polarization is placed at about 45 degree to [110] axis.

tivity change (attributed to charge carrier screening and relaxation) changes its shape,

which is consistent with results reported for 2.0 eV pump photon energy [64]. At low excitation density, the charge carriers need longer time to screen the surface charge electric field, and at high excitation density, screening becomes faster [64]. The slow reflectivity changes after zero delay time are mainly attributed to the decaying of the excited charge carrier density. In our experiment, the excited charge carriers do not have enough energy to be scattered or tunnel to the L or X valleys. The coherent optical response is a nonlinear process. As the pump intensity increases, we expect the coherent peak to grow proportional to the pump intensity. By fitting the phonon oscilla-

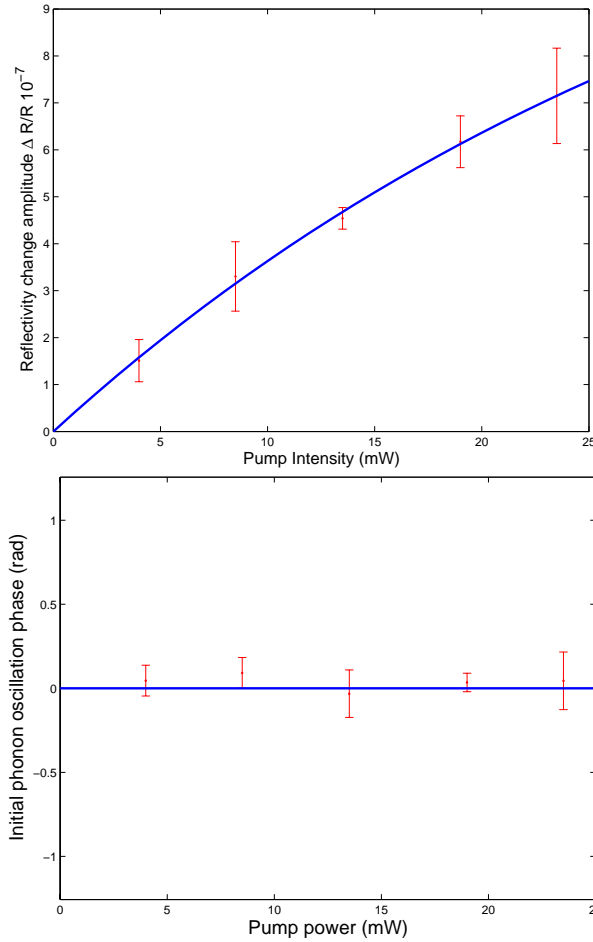


Figure 3.9: Pump intensity dependence of coherent phonon oscillations in GaAs. The upper panel is initial amplitude vs. the pump power, and the bottom panel is the initial phase vs. pump power. Lines are guides to eye.

tions with a decaying cosine function, the amplitude and initial phase were determined.

They are plotted in Fig. 3.9. The upper panel is the amplitude of the phonon oscillation vs. the pump intensity. The phonon oscillation amplitude is sublinear in pump power. The continuous line is a guide to the eye. The bottom panel is the initial phase vs. the pump power. In the graph, we can see that the initial phase is essentially constant.

Another set of the pump power dependence experiments was carried out with the pump beam polarized parallel to the [110] axis of the crystal. The crystal orientation and the polarization of the probe beam are in the same condition as in the first set of experiments. The pump beam power was set at 3.4, 8.0, 14.0, 18.0, 26.0, and 32.5 mW. The results are shown in Fig 3.10. The reflectivity change due to the slowly decaying charge carrier excitation had the same behavior as when the pump beam was polarized along [010]. However, the relationship between the phonon oscillation and the pump

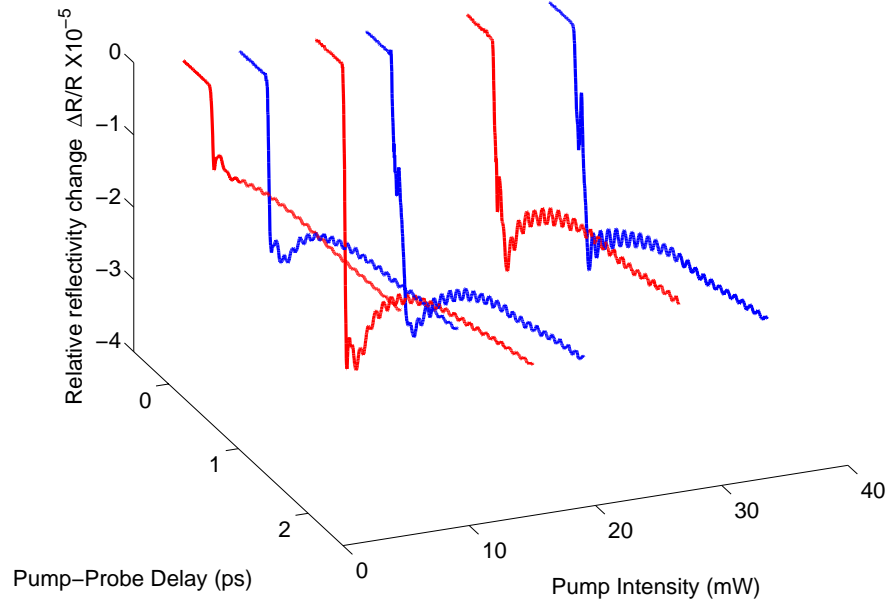


Figure 3.10: Pump power dependence of the pump-probe spectra. The pump power are 3.4, 8.0, 14.0, 18.0, 26.0, and 32.5 mW. The pump polarization is set along crystallographic [110].

intensity are different from before. The upper panel in Fig. 3.11 shows the pump power dependence of the phonon amplitude extracted from Fig. 3.10. The blue line is a guide line to eye. The bottom panel in Fig. 3.11 shows the pump power dependence of the phonon phase. The phonon oscillation phase increases when the pump power

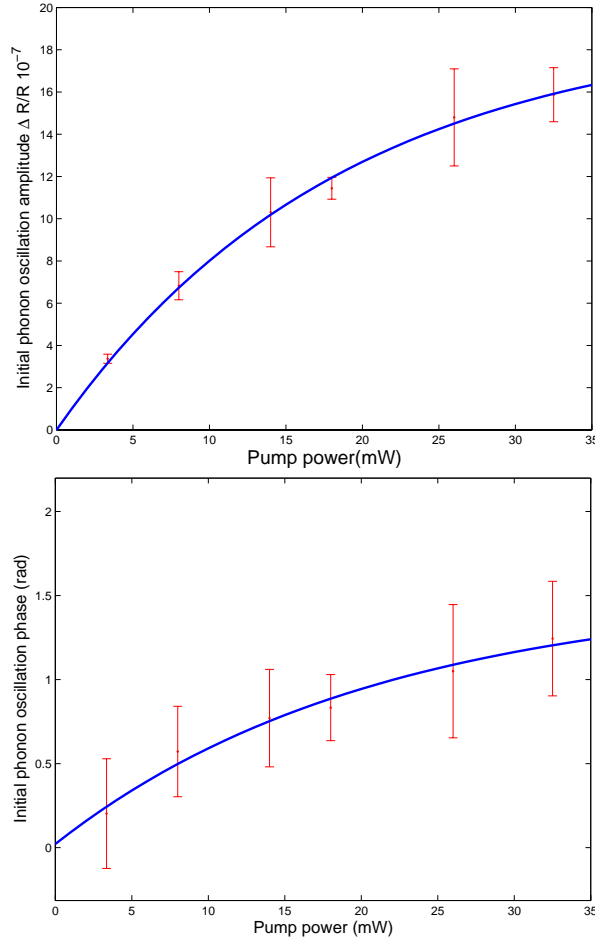


Figure 3.11: Pump beam power dependence of coherent phonon oscillations in GaAs. The above graph is the initial amplitude vs. the pump power, and the bottom graph is the initial phase vs. pump power. The blue solid line is a guide to the eye.

increases. The blue solid line is a guide to the eye.

3.2.4 Crystal Orientation Dependence of Phonon Oscillation

In this subsection, the polarization effects of the probe beam were measured. The ideal situation would be to rotate the probe beam polarization only. However, in our case, this would imply having to rotate both the polarizing beam splitter and the detector, which was not practical.

We therefore rotated the sample instead of the polarization of the probe beam. In

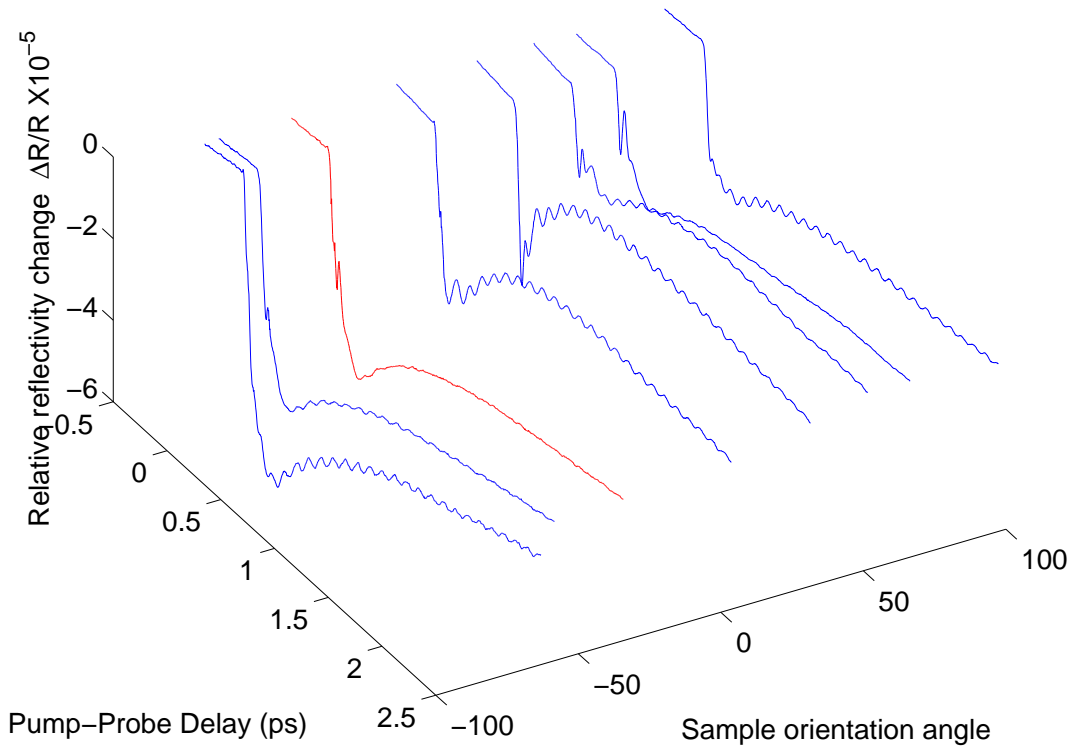


Figure 3.12: GaAs Sample orientation dependence of reflectivity changes. The angles between the pump polarization (horizontal) and axes $[-110]$ are -71° , -66° , -41° , -4° , 24° , 44° , 59° , and 90° .

this experiment, the symbol θ represents the angle between the horizontal direction and the $[1-10]$ axis. The pump intensity was set at about 20 mW. The experimental results reflected the combined effects of rotating the pump and probe beam polarization angles. Fig. 3.12 shows some of our reflectivity change curves where θ values are -71° , -66° , -41° , -4° , 24° , 44° , 59° , and 90° . As θ approached 45° , the oscillation amplitude became very small. We used an exponentially decaying oscillation as in equation 3.3 to fit the oscillation in the reflectivity change curves. The fitting parameters are shown in Fig. 3.13. The upper panel in Fig. 3.13 is the phonon oscillation amplitude vs. the angle θ between crystal $[110]$ axis and the horizontal direction. The red dots and error bars are experimental results and their error from the measurement. The green dash line is the best fit to a simple cosine function $\Delta R/R = -16.9 \cos(2\theta)$. The blue solid line is given by $\Delta R/R = -16.7 \cos(2\theta)(1 + 0.22 \cos(2\theta))$, which counts the effect of the pump

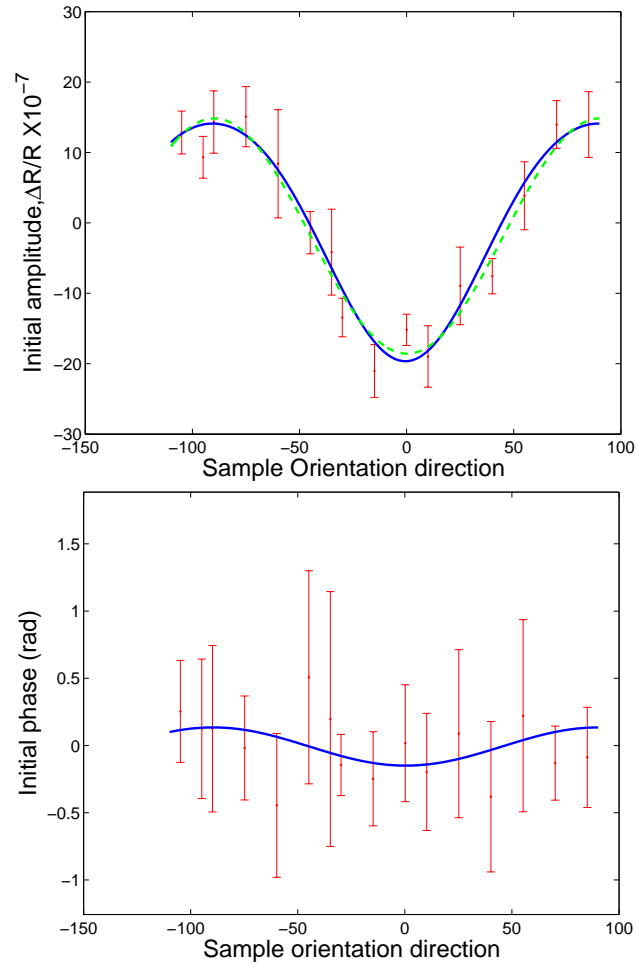


Figure 3.13: Sample orientation dependence of the phonon oscillations in GaAs. The upper panel is the initial amplitude vs. the sample rotation angle. The bottom panel is the initial phase vs. sample rotation angle.

polarization rotation in. The bottom panel is the initial phase vs. θ . As θ approached $\pm 45^\circ$, the oscillation amplitude became very small, the fitting error of the initial phase was very large. It was easy to inadvertently change the zero delay time when rotating the sample. In the experiment, we tried our best to keep the zero delay unchanged, however, it was unavoidable that the error in the initial phase increased. In the bottom panel of Fig. 3.13, the blue line is an guide to the eye.

3.3 Pump-Probe Spectroscopy of Ge

The polished Ge wafer had a low density of n-type dopants. The experimental setup and condition were the same as for GaAs. We measured the pump polarization dependence and sample orientation dependence of the reflectivity change in Ge.

3.3.1 Pump Polarization Dependence in Ge

The pump beam polarization dependence in Ge was measured in the same way as we did in the case of GaAs. The [001] and [110] crystal axes were set at horizontal direction, and the reflected probe beam was split into two equal intensity parts: horizontal and vertical. the symbol θ represents the angle between the horizontal direction and the pump beam polarization in the experiment. The pump beam power was about 20 mW. Figure 3.14 shows the reflectivity change curves obtained at varies pump beam polarization angles. We can see that the electronic response and the coherent response have a period of 180° . Moreover, there is an anti-periodicity of period 90° , i.e. the signal is reversed upon 90° rotation of the pump polarization. This is consistent with the cubic crystal symmetry. Because the crystal point group O_h contains the inversion and C_4 symmetry separately (not just their combination S_4 , as in the case of GaAs, point group T_d), the surface field does not reduce the surface symmetry to C_{2v} (from C_{4v}) as in the case of GaAs. The oscillations attributed to the phonon also reverse their sign when the pump beam polarization was rotated by 90° . When the pump polarization was set at 45° to the horizontal, no phonon oscillation was observed. We fit the oscillations in the reflectivity change curve with an exponentially decaying cosine oscillation as Eq. 3.3. The frequency of the phonon is 9.02 ± 0.15 THz, and the decay constant is about 4 ps. The initial amplitudes and phases were plotted in Fig. 3.15. The upper graph is the amplitude vs. angle and the bottom graph is the initial phase vs. angle. The initial amplitude was fitted with $\Delta R/R = 1.97 \cos(2\theta) \times 10^{-7}$. The initial phase was fitted with a constant of 102° within the range of the error.

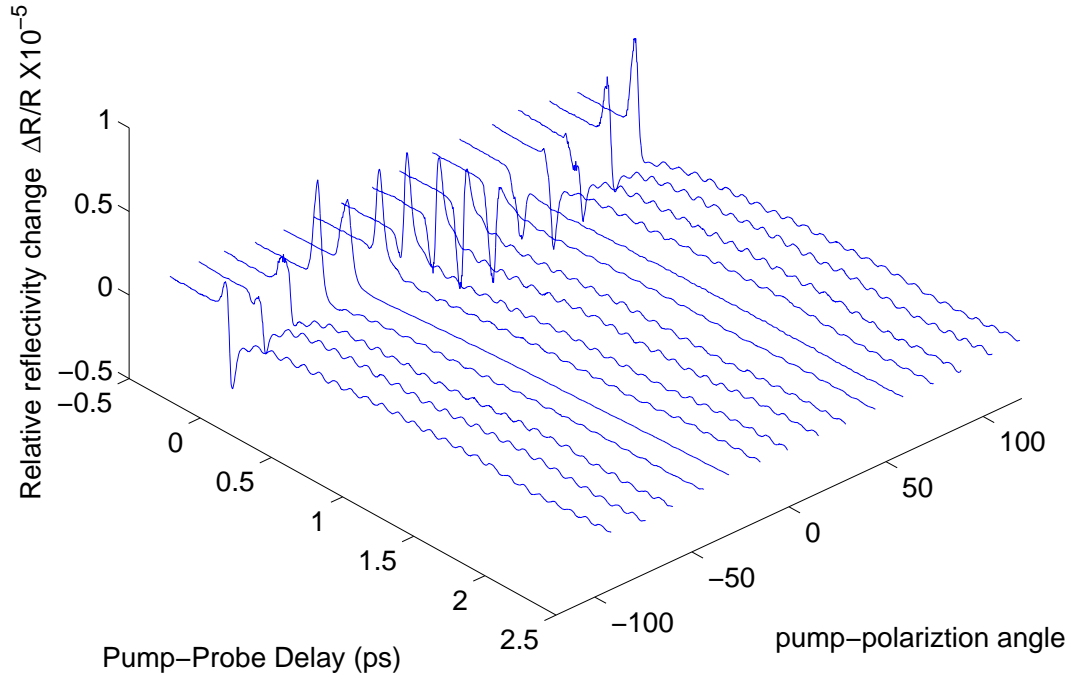


Figure 3.14: Dependence of the differential pump-probe spectra for Ge on the polarization direction of the pump beam. The pump polarization angles are -106° , -90° , -76° , -60° , -46° , -30° , -16° , 0° , 14° , 30° , 44° , 60° , 74° , 90° , and 104° .

3.3.2 Crystal Orientation Dependence of Ge

The crystal orientation dependence experiment with Ge was carried out the same as with GaAs. The pump intensity was set at 20 mW. As the sample was rotated, the reflectivity change curves were recorded. The sample orientation angles were set at -15° , 0° , 30° , 45° , 53° , 60° , 75° , 90° , and 105° . The curves repeat with a period of 90° , which is consistent with the symmetry of the Ge crystal structure. We used an exponentially decaying cosine curve (Equation 3.3) to fit the oscillations in the reflectivity change curves, and the fitted initial oscillation amplitude and phase were plotted in Fig. 3.16. In the upper panel in Fig. 3.16 the blue curve is the fitting curve of with function of $A=1.93\cos^2(2\theta)$. The initial phase in Fig. 3.16 is a constant within the range of the error bars.

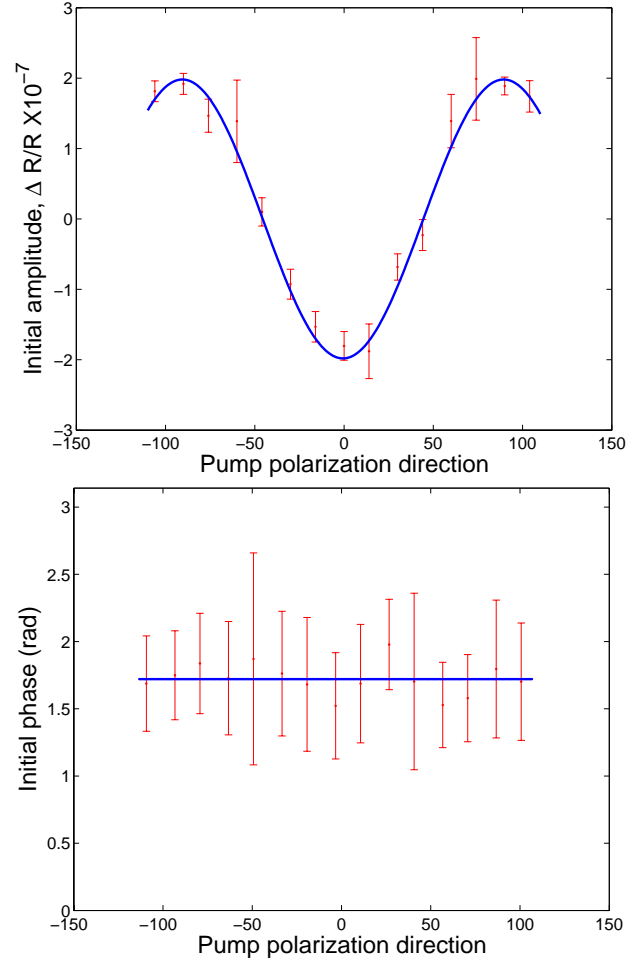


Figure 3.15: Pump polarization dependence of phonon oscillations in Ge. The upper panel is the initial amplitude vs. pump polarization direction, and the bottom panel is the initial phase vs. pump polarization direction.

3.4 Discussion and Conclusion

3.4.1 Excitation Mechanisms

Coherent phonon excitation mechanisms may be classed into impulsive, displacive and intermediate cases by the initial phase. When the initial phase is close to $\pi/2$, the excitation mechanism is impulsive. This may be brought about by a mechanism called impulsive stimulated Raman Scattering [11]. This mechanism leads to a reflectivity

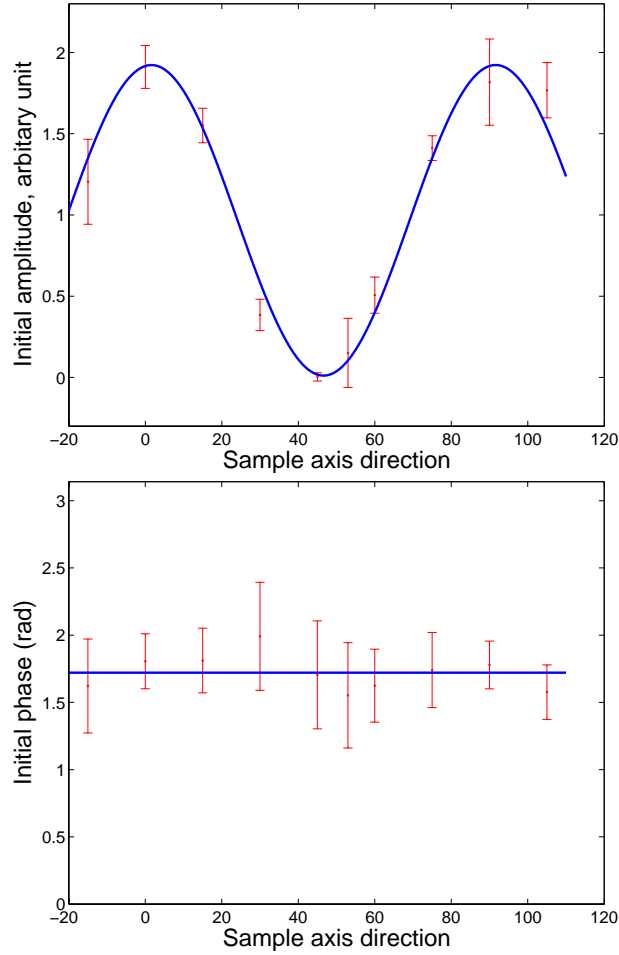


Figure 3.16: Sample orientation dependence of the phonon oscillations in Ge. The upper panel is initial amplitude vs. the sample orientation angle. The bottom panel is the initial phase vs. the sample orientation angle.

change of the form

$$\Delta R/R \approx A e^{-\Gamma t} \sin(\Omega t) \quad (3.4)$$

Here Ω is the frequency of the coherent phonon, and t is the time delay between the pump and probe pulses. Γ is the dephasing time constant, not only the energy relaxation time of the coherent phonon. A is a constant related to the Raman cross-section, the refractive index of the material, the photon frequency, and the pump beam intensity [11]. This mechanism has been proposed to describe coherent phonon generation in transparent materials. In this situation, the force on the phonon coordinate exerted by the laser pulse has the same life time as the pulse width of the pump beam which is

much shorter than the period of the coherent phonon as shown in Fig. 3.17

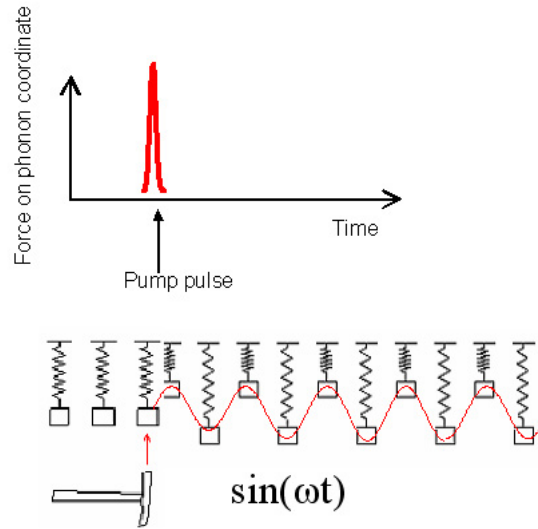


Figure 3.17: Illustration of impulsive coherent phonon excitation mechanism. A possible interaction between the sample and the light pulse giving rise to such a sine-like oscillation is impulsive stimulated Raman Scattering. The force on the phonon coordinate exerted by the laser pulse has the same life time as the pulse width of the pump beam which is much shorter than the period of the coherent phonon.

In contrast, when the initial phase of the phonon oscillation is close to π or 0, the excitation of mechanism is considered a displacive mechanism. This tends to occur in absorptive materials. Zeiger *et al.* proposed an excitation mechanism named as "displacive excitation of coherent phonons" (DECP) [65]. In their explanation, electrons are excited when the pump light is absorbed, and these excitations change the equilibrium position of the phonon coordinate. This is equivalent to a force exerted on the phonon potential with a life time of the force which is much longer than the oscillation period of the phonon. This mechanism is illustrated in Fig. 3.18. Zeiger *et al.* argued that only totally symmetric phonon modes are excited by DECP because exciting electron distribution is thought to quickly lose all memory of the polarization direction of the exciting lights, thus becoming a totally symmetric distribution if so called "hot electrons". A totally symmetric hot electron distribution can excited only the total symmetric coherent phonons. When the life time of the excited electron is much longer than the period of phonon displacement, and therefore the reflectivity change

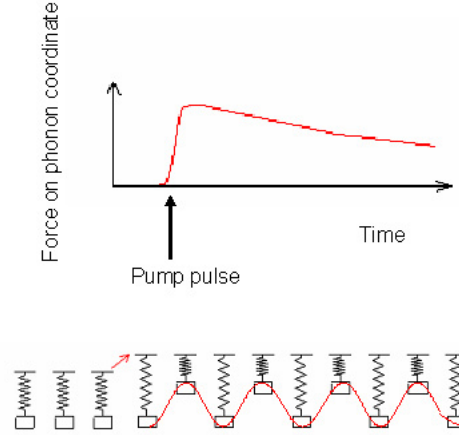


Figure 3.18: Illustration of displacive excitation of coherent phonons. The phonon coordinate is subjected to a force due to the hot electrons, which lasts much longer than the phonon vibration period. The oscillation of this excitation is cosine like.

can be expressed by

$$\Delta R/R \approx Ae^{-\Gamma t} \cos(\Omega t) \quad (3.5)$$

There is a similar description for the coherent phonon excitation mechanism in GaAs, which was proposed by Cho *et al* [61, 63, 70]. In their description, when the electrons and holes are excited near the surface of the semiconductor, they drift to the opposite direction under the effect of the surface field. As a result of drifting, the surface electric field is screened, leading to a sudden change in force on the phonon coordinate. The screening effect was believed to be one special case of DECP [11]. In this effect, the coupling path between the hot electrons distribution and the phonon coordinate was pointed out. In both of these two descriptions, the pump photons excite electrons, and the excitation of the coherent phonon, is due to photoexcited electrons. However, the symmetry selection rule of the surface screening mechanism is not necessarily totally symmetric mode of the crystal (example, GaAs, T_2), but the totally symmetric in the point group of the surface.

Merlin's group developed a theory of transient stimulated Raman scattering (TSRS) to explain coherent phonon excitation [11, 13, 66]. They used two Raman tensors to describe the excitation and the probing of the coherent phonon. Both of these tensors

have the same real part but they differ in the imaginary part. The tensor responsible for probing is just the regular Raman tensor, while the tensor responsible for the excitation is different. In a transparent material, the imaginary part of both tensors vanishes, and the tensors become the same. In this case, coherent phonon excitation is predicted to be impulsive. In an absorptive material, the excitation tensor has significant weight on the imaginary part, and the initial phase shifts from $\pi/2$ to π or $3\pi/2$ to zero. In the limit that the imaginary part is much larger than the real part of the tensor, the initial phase approaches 0 or π , i.e. the excitation becomes displacive. In this sense, certain displacive excitation mechanisms can be considered special cases of TSRS mechanism.

In the TSRS mechanism, the wave vector of the charge density fluctuation has to match the wave vector of the phonon, and the laser light. Since the stimulated Raman scattering is a coherent process, any electronically incoherent mechanism cannot be TSRS. In some materials, photo-excited electrons are strongly scattered by phonons, or electrons, such that they quickly lose their coherence. Although these photo-excited electrons are incoherent, they are still capable of exciting coherent phonons. Whether such incoherent electrons excite coherent phonons impulsively or displacively depends on the hot electron lifetime compared to the phonon oscillation period. Therefore, it is often difficult to decide experimentally whether a coherent phonon was excited by the coherent TSRS mechanism or the incoherent "hot electron" mechanism. An exception is surface field screening mechanism in GaAs, which is clearly caused by incoherent photoexcited charge carriers. In this effect, as the photoexcited electrons screen the surface field of the material, and the phonon coordinate is subjected to a transient force. The lifetime of this transient force ranges from a few femtoseconds to picoseconds.

In our experiments, the oscillations of coherent phonons in GaAs have two parts; one is dependent on pump polarization and the other is independent of pump polarization. The amplitude and the initial phase of the coherent phonon in Fig. 3.7 was fit by

$$A = (8.0 + .8\cos(2\theta)) * 10^{-7}$$

$$\phi = -0.05\cos(2\theta) * \pi$$

Where θ is the angle between the pump polarization direction and crystal [110] direction. The oscillation of the coherent phonon in Ge has only the pump polarization dependent part. The initial phase of that is a constant, 0.57π , and the amplitude, shown in Fig. 3.15 can be fit by

$$A = 0.97\cos(2\theta) \times 10^{-7}$$

Here, θ is the angle between the pump polarization direction and crystal [110] direction. The fact that the initial phase is close to $\pi/2$ means that the excitation mechanism is mostly impulsive. From the symmetry of the crystal, we expect that the pump polarization dependence follows $\cos(2\theta)$. The observed relationship between the polarization of the pump beam and the Ge crystal axis is consistent with the symmetry of the T_{2g} optical phonon mode in Ge. We conclude that TSRS is a likely excitation mechanism of the coherent phonon in Ge. The amplitude and the initial phase of the coherent phonon in GaAs changed when the pump polarization was rotated; the change of the initial phase has a 2-fold symmetry, and the change of the amplitude also has a 2-fold symmetry. In contrast to Ge, the amplitude did not reverse its sign when the polarization of pump beam was rotated by 90° . From the symmetry of the bulk Raman tensor of the coherent phonon mode in equation 3.1, the TSRS mechanism contribution to the excitation of the coherent phonon is zero when the pump polarization is along the [010] or the [100] axis. In the measurement, we found that the coherent phonon oscillations at this pump polarization angle was not zero, but had an amplitude of 8.0×10^{-7} . By symmetry, we can thus exclude bulk TSRS as the excitation mechanism. The initial phases of the coherent phonon oscillations in these directions are zero, which implies a displacive mechanism. Physically, the mostly likely candidate for such a displacive excitation is the "screening" effect of the photoexcited electron mechanism [61], where the photoexcited charge carriers screen the near surface band bending field, resulting in a displacive change of the equilibrium ion position.

In order to investigate to what extent the TSRS mechanism contributes to the

phonon excitation mechanism when the pump beam polarization is not along [010] or [100], we have plotted the data of Fig.3.7 and 3.15 in a polar plot, shown in Fig. 3.19. In this figure, the initial phase of the oscillations is the polar angle, and the amplitude is the radius. The red crosses represent the data from the GaAs (001) surface, and the red line is a linear fit. The blue stars represent the data from the Ge (001)

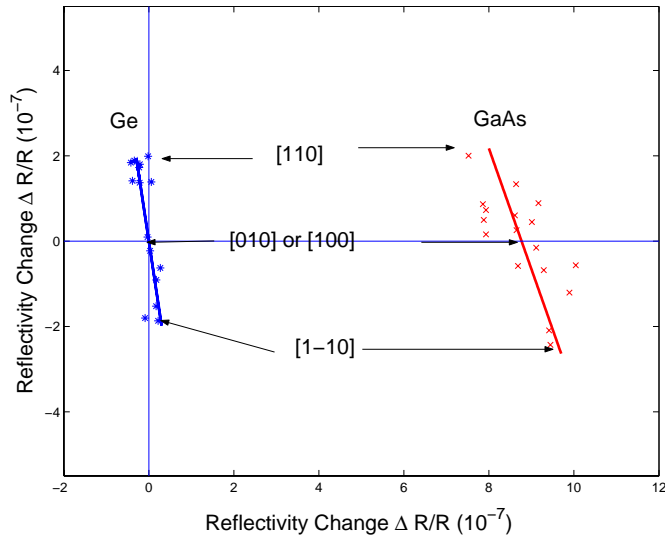


Figure 3.19: Polar plot of coherent phonon amplitude vs initial phase. The angle between the data point and the x axis represents the initial phase of the coherent phonon oscillation, and the distance from the origin is the initial amplitude of the coherent phonon. The blue stars represent the data from the Ge surface and the red crosses represent the data from the GaAs. The blue line and the red line are the fitting curves. The unit of the amplitude labeled in the figure is 10^{-7} .

surface. The excitation mechanism of the coherent phonon in Ge appears to be purely TSRS, which is the blue line passing through the origin in Fig. 3.19. The angle of this line is $102 \pm 15^\circ$, which represents the initial phase of the coherent phonon. The error mainly comes from the calibration of the initial phase. As discussed above, when the pump beam is polarized along the GaAs [010] or [100] direction, the TSRS mechanism makes no contribution to the excitation of the coherent phonon. The excitation mechanism at this polarization direction is purely the screening effect of the photoexcited charge carriers, which is represented by a line on the x-axis in Fig. 3.19. We fit the phonon amplitude and phase data points with a red line in the figure. The angle to

the x axis is about $109 \pm 4^\circ$. The crossing point of the red line and the x axis can be regarded as the origin of the TSRS contribution. The distances from this point to the data points are the amplitudes contributed by the TSRS mechanism, and the angle is the initial phase of coherent phonon component excited by the TSRS mechanism.

In the TSRS mechanism, when the material is transparent, the Raman interaction results in an impulsive force. The phonon thus begins to oscillate at its equilibrium position with maximum velocity. When the material is absorptive, besides the coherent stimulated Raman interaction between the light and the phonon, the incoherent excited electrons also interact with the phonon coordinate. We modeled the effect of the coherently and incoherently excited electrons as an exponentially decaying force with decay constant λ , shown in Fig. 3.20. Thus the motion of the phonon can be described by

$$\ddot{Q} + 2\gamma\dot{Q} + \omega^2 Q = F(t) = Ae^{-\lambda t} \quad (3.6)$$

Here, A is an amplitude of the force, and γ is the dephasing time of the coherent phonon. We solve this equation analytically with the boundary condition that at delay time zero the phonon coordinate stays at the equilibrium position. The solution can be expressed as

$$Q(t) = -\frac{Ae^{-\gamma t} \cos(\Omega t + \varphi)}{\sqrt{\omega^2 - \gamma^2}} + \frac{Ae^{-\lambda t}}{\sqrt{\omega^2 - 2\gamma\lambda + \lambda^2}} \quad (3.7)$$

$$\Omega = \sqrt{\omega^2 - \gamma^2} \quad (3.8)$$

$$\tan(\varphi) = -\frac{\lambda - \gamma}{\sqrt{\omega^2 - \gamma^2}} \quad (3.9)$$

In the case that we can observe the coherent phonon oscillation, the dephasing time is much longer than the period. So we can simplify the solution to

$$\Omega = \omega \quad (3.10)$$

$$\tan(\varphi) = -\frac{\lambda}{\omega} \quad (3.11)$$

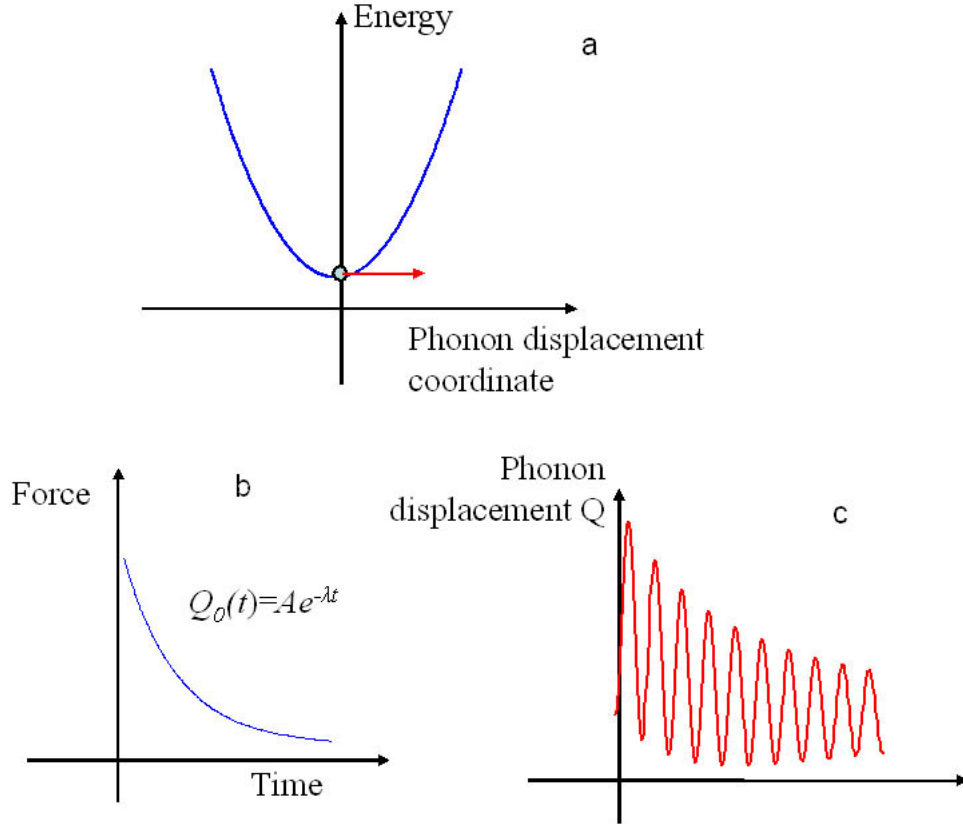


Figure 3.20: Schematic of the effect of excited electrons on the coherent phonon excitation. The potential of the phonon coordinate is modeled as the harmonic potential as shown in panel a. Panel b shows exponentially decaying the force on the phonon coordinate caused by the excited electron. The time constant of this force has the same order of the phonon oscillation periods. Panel c is the oscillation of the phonon coordinate.

From equation 3.11, since $\tan(\varphi) < 0$, it is obvious that the data point are predicted to lie in the 2nd and 4th quadrants of Fig. 3.19 for the TSRS mechanism, as observed for Ge. On the other hand, we can obtain the lifetime of the electron excitation from the initial phase of the coherent phonon via equation 3.11. According to this analysis, the electronic life time in Ge is determined to be 4 ± 5 fs, and the lifetime of electron excitation in GaAs is 6 ± 2 fs. The initial phase of the coherent phonon in Ge was given in reference [62] as about 90° . This is in the range of error of our measurement, $102 \pm 15^\circ$.

In the measurement of Ref. [62], the autocorrelation was used to define the zero delay time, which is likely to have caused some measurement error in the phase as we

discussed in Chapter 2. However, in the literature, the excitation mechanism of coherent phonons in GaAs was believed to be only the screening effect of the photoexcited electrons because no dependence of the pump polarization was found [61, 63, 64]. The photon energy in Cho's experiment was 2 eV instead of 1.55 eV used by us. The amplitude of the coherent phonon of the screening effect is proportional to the absorption coefficient [65, 11]. The absorption coefficient at 2.0 eV is about three times of that at 1.55 eV [105], which means that the amplitude of the coherent phonon due to the screening effect is expected to be two times larger than in our experiment at 2.0 eV photon energy. In transparent materials, the TSRS phonon amplitude is proportional to the Raman cross section [11]. The real part of the excitation tensor of the coherent phonon has the same real part as the Raman tensor [66] in absorptive materials. When the dominant part of the excitation tensor is still the real part, the amplitude of the coherent phonon is still roughly proportional to the Raman tensor. In GaAs, the initial phase of the TSRS contribution is 109° , which means that the dominant part is still the real part. Since the Raman cross-section at 2.0 eV is about half of that at 1.55 eV [106], we can roughly estimate that at 2.0 eV the amplitude of the coherent phonon excited through the TSRS is half of our measured value for 1.55 eV photons. The ratio between the contribution of TSRS and screening effect is about 1:4 in our experiment. Therefore, we estimate this ratio to be about 1:24 at 2.0 eV. The total amplitude of these two contributions is their vector sum. With the assumption that the resonant TSRS has the same initial phase as at 1.55 eV, the difference between the maximum and minimum amplitude of the coherent phonon in GaAs is predicted to be about 3% when we use 2.0 eV photons to measure the pump polarization dependency of GaAs. Considering that the measurement accuracy of Cho's experiment was no better than about 5% [61], it is understandable why this small 3% modulation was not detected. Similarly, the initial phase shift of the coherent phonon is estimated to be about 2° at 2.0 eV energy, which is also much smaller than the experimental accuracy.

We conclude that the coherent phonon excitation mechanism of the coherent phonon

in GaAs crystal is a combination of TSRS and screening effect of the photoexcited electrons. The relative contribution of both mechanisms depends on the exciting photon energy. The relative contribution of the TSRS mechanism is too small to measure when 2.0 eV photons are used to excite and probe the phonon. However, using 1.55 eV photons, the TSRS mechanism contributes enough to the amplitude to be detectable as a pump-polarization dependent component.

3.4.2 Continuous Wavelet Transform Analysis

Continuous wavelet transform (CWT) is a data analyzing method in which a short period of time is windowed to obtain something like a local Fourier transform, and the time-frequency relationship is obtained when the window shifts on the time sequence. In recent years, this method has been used in the data analysis of ultrafast spectroscopy [15, 67, 107]. Real time phonon frequency changes were observed in CWT of ultrafast spectroscopy [15]. The line shape of the spectrum was used to analyze the interactions in the crystal or molecules [108]. Hase *et al.* tried to use CWT spectra to observe interactions in real time [67, 107, 109]. We will use CWT to analyze pump-probe spectra and compare with the CWT of simulated spectra.

Panel a in Fig. 3.21 is a CWT result of a reflectivity change curve in Fig. 3.6 in GaAs with pump beam polarized at 90° . Panel b is a CWT result of a reflectivity change curve in Fig. 3.6 in GaAs with the pump beam polarized at 0° . Under the color figure are the spectra at zero delay time. Comparing the two spectra at 0 delay time, spectrum in panel c has a deep dip at about 7 THz. Panel a is obtained with the pump beam polarized the along [1-10] axis, and panel b is obtained with pump beam polarized along at the [110] along. As we discussed in the last subsection, there are three components in the reflectivity change curve: the coherent optical response, the electronic response, and the coherent phonon oscillation. In the experiment, if the probe beam is not strictly at 45° to the horizontal, we can minimize the electronic contribution (the slow decay part due to the electronic excitation) in the pump probe

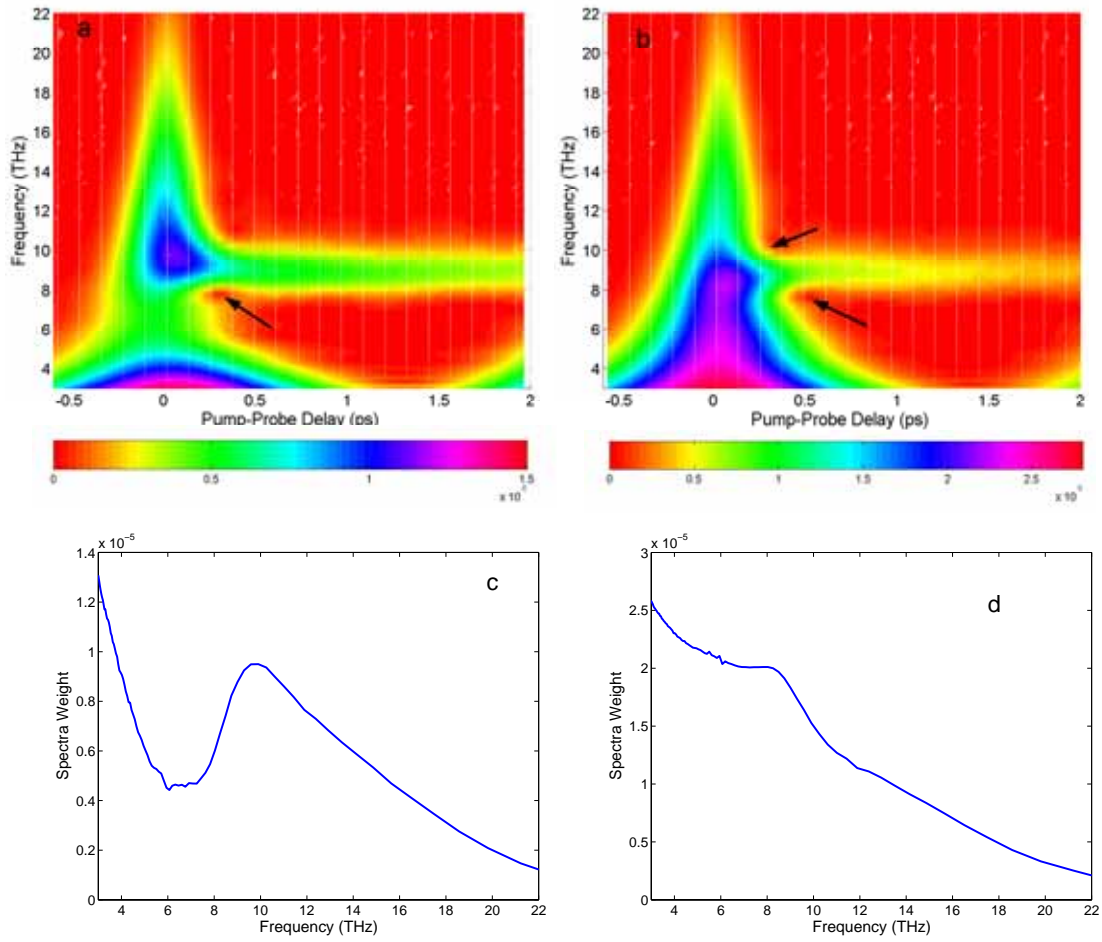


Figure 3.21: Continuous wavelet transforms of GaAs reflectivity change curves. The reflectivity change curves from Fig. 3.6. The polarization angles of the pump beam are -90° , and 0° , respectively. Positions of spectral holes are pointed out by arrows. The lower curves are the cross sections of the CWT spectra at zero delay time of the upper figures.

spectra by changing the intensity ratio in the signal and reference sensors. As a result, the phonon contribution will be enlarged. The resulting reflectivity change curve and its CWT are shown in Fig. 3.22. Compared with panel a and b in Fig. 3.22, the slow

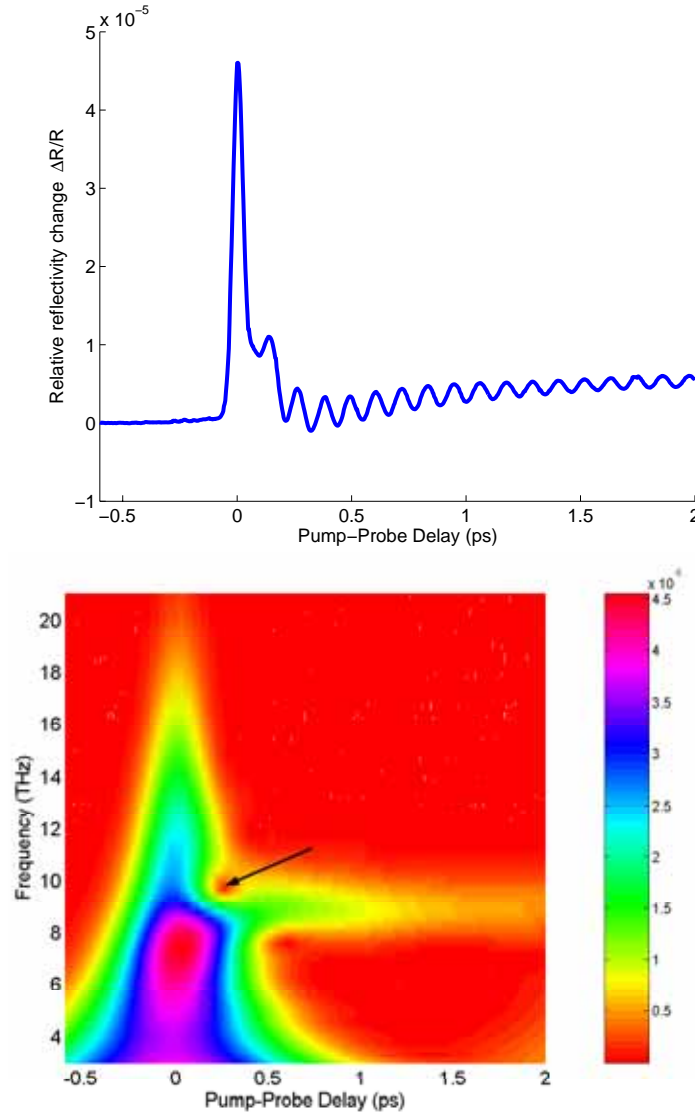


Figure 3.22: The result of unbalanced reflectivity change curve and its CWT results. In the measurement, the pump polarization at crystal [110] direction. The position of a spectra hole is pointed out by an arrow.

electronic response does not have much contribution at frequencies higher than 5 THz. The oscillation of the phonon has larger weight in the reflectivity change curve features in Fig. 3.22, which makes the frequency of 8.8 THz become stronger and the canceling

hole at higher frequency became more obvious.

To obtain insight into physics contained in the CWT of the reflectivity change curve, we have used simulated pump-probe spectra to study the results of CWT. A decaying cosine with a phase shift is used to simulate the phonon oscillation. An autocorrelation is convoluted with this decay cosine wave to be the start of the phonon oscillation. The coherent optical response is a fast decaying component, and it has the same decaying speed as the autocorrelation peak, so we use the autocorrelation peak as the coherent optical response, which was also described in reference [16]. The contribution of the electron response is represented by convoluting the autocorrelation with an exponential decay, which was suggested by several papers [18, 70]. The basic shape of these three contributions are plotted in Figure 3.23. We used different weights of

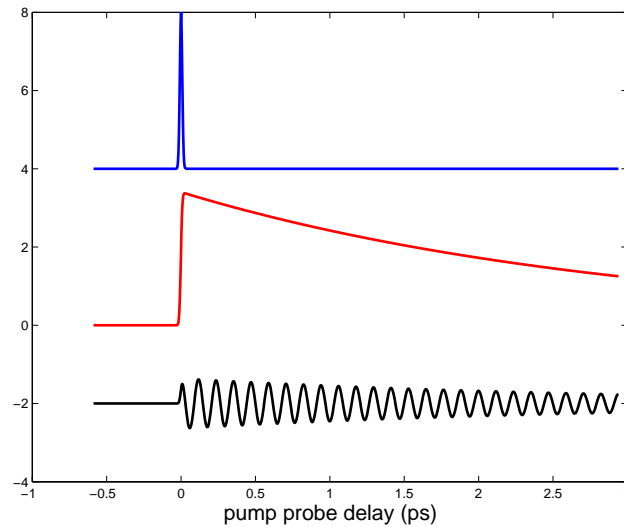


Figure 3.23: Simulated reflectivity change with three different contributions. the upper blue peak represents the coherent optical response, the middle red curve represents the electronic contribution. The bottom black curve is the coherent phonon oscillation.

these three components and different initial phases of the phonon oscillation to create the reflectivity change curves, then processed the CWT of these curves. After we studied CWT images with different weight of the electronic responses, we find that the weights of the electronic response has a large effect on the low frequency part, but the effect on the higher frequency is very weak, almost no effect when the frequency

is higher than 5 THz. The coherent phonon oscillations have a main frequency component at the frequency near 8.8 THz which exhibits a decaying band. The coherent response has frequency components in a large range at near zero delay time. As we sum up these three parts with a ratio of 1:1:1, and set the initial oscillation phase to Zero, then process the CWT, we obtained panel a in Fig. 3.24, which is similar to our GaAs result in Fig. 3.21. The difference is that CWT results of the GaAs reflectivity change curves in Fig. 3.21 has only one dip when the delay time is 0.3 ps in either graph, while the simulated results has the two symmetrical dips at both sides. As we sum up three contributions with the ratio of 1:1:-1, in other words, reversed the initial phase of the phonon oscillation, then process CWT, we obtain panel b shown in Fig. 3.24. There is a deep hole at the place that the frequency is 8.8 THz and the delay time is about 50 fs. If we enhance the component of the coherent optical response, this hole shifts to a later delay time. If we weaken the component of the coherent optical

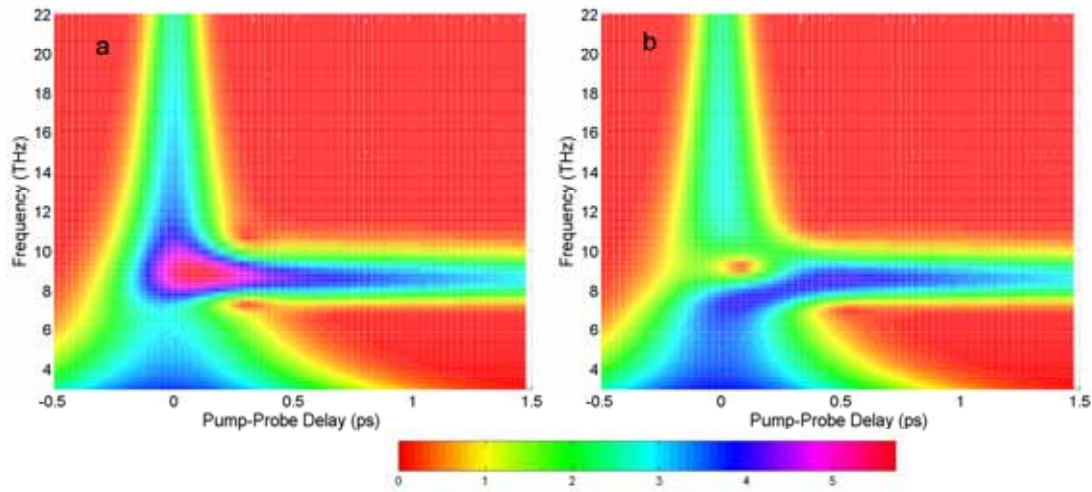


Figure 3.24: The CWT result of the sum of three different contributions. Panel a is a CWT map of a curve obtained by summing of three curves in Fig. 3.23. Panel b was is a CWT map of a curve obtained by summing of the upper two curve, then subtracting the bottom one in Fig. 3.23.

response, the hole moves to an earlier delay time. If we increase the phonon oscillation initial phase, this hole moves to a higher frequency. If the initial phase decreases, the frequency of the hole becomes lower. These are consistent with the CWT results of our

experimental values.

In our simulation, the position of the hole in the CWT spectra is determined by the initial phase of the coherent phonon, and the ratio between the amplitude of the coherent response and the amplitude of the coherent phonon oscillation. In the differential reflectivity measurement, the ratio between the coherent peak and the phonon amplitude is determined by many factors, for example, the pulse width of the pump and probe beams, and the way that the probe beam splits. The spectral hole position in the frequency is determined by the initial phase of the phonon oscillation, which will not change for different measurements. Therefore, all we can learn from the existence of an "antiresonance" in CWT is the initial phase of the phonon, with respect to the coherent peak. Any direct conclusion about coupling/interaction between electronic and coherent phonon degrees of freedom appears doubtfully. In the simulation, the initial phase seems related to the frequency of the spectral hole in CWT. The hole frequency in the simulation has the same value as the spectra hole in the CWT of measured data. These suggest CWT is a possible tool for us to find the initial phase of the coherent phonon. We may need more simulation to explore the different conditions, for example, changing the line shape of the coherent optical peak.

3.4.3 Summary

We have observed coherent optical phonon oscillations in GaAs and Ge crystals directly through their modulation of the anisotropic reflectivity signal. We have also investigated the excitation mechanism of the coherent phonon by measuring the pump and the probe polarization dependency and the pump intensity dependency. The symmetry of the coherent phonon excitation in Ge agrees with the symmetry of the Raman tensor, which suggests that the excitation mechanism is TSRS. The measured initial phase of the coherent phonon in Ge is $102 \pm 15^\circ$. The coherent phonon excitation in GaAs depends on the polarization of the pump beam, however, the symmetry of the coherent phonon excitation does not agree with the symmetry of the T_2 phonon, Although

the symmetry of probing the coherent phonon agrees with it. The pump polarization dependency of the coherent phonon in GaAs crystal can be decomposed into a pump polarization independent component and a pump polarization dependent component which agrees with the symmetry of the T_2 phonon's Raman tensor. Both screening effect of photoexcited electron and TSRS mechanisms contribute to the excitation of the coherent phonon in GaAs. The initial phase of the coherent phonon is $0 \pm 4^\circ$ when the pump beam is polarized along the [010] or [100] crystal axes where the stimulated Raman contribution is zero. The initial phase of the phonon oscillation shifts to a positive value when the polarization of the pump beam is rotated to the [110] axis and a negative value when the polarization of the pump beam is rotated to the [1-10] axis.

We used the CWT to analyze our measured reflectivity change curves and simulated reflectivity change curves. Spectral holes appear in all CWT figures. The center frequency of those holes is determined by the initial phase of the coherent phonon.

Chapter 4

Femtosecond Spectroscopy of Ferroelectric LuMnO_3

The hexagonal rare-earth manganites RMnO_3 ($R = \text{Ho, Er, Tm, Yb, Lu, Y}$), are multiferroic materials in which magnetic order coexists with ferroelectric order [110]. Coupling between ferroelectric and magnetic order in multiferroic materials provides the potential of controlling the magnetic properties electrically or optically [75]. To realize this potential, the interactions among charges, orbital, spin and lattice degrees of freedom have to be clearly understood. We have used femtosecond spectroscopy to investigate the coupling between photoexcited electrons and coherent phonons in LuMnO_3 . I will begin with the background and properties of the hexagonal multiferroic crystal.

4.1 Structure and Properties of LuMnO_3

LuMnO_3 has both ferroelectric and ferromagnetic order. The phase transition temperature for frustrating anti-ferromagnetic order is about 90 K. It is anti-ferromagnetic below 90 K. The temperature for the ferroelectric phase transition is about 900 K. Thus at the temperature below 90 K, it is both anti-ferromagnetic and ferroelectric. At room temperature, it is ferroelectric.

4.1.1 Crystal Structure

In LuMnO_3 crystal, the manganese ion and the five neighborly oxygen ions constitute a triangular bi-pyramid with the Mn ion at the center, and oxygen ions at the apexes. Hexagonal layers constructed by oxygen Mn bi-pyramids are separated by layers of Lu ions as shown in Fig. 4.1. The buckling of the Lu layers and the tilt of the oxygen

bi-pyramids breaks the inversion symmetry of the crystal. This lattice distortion makes

Table 4.1: Atomic position parameters of LuMnO_3 from single crystal x-ray diffraction [111]. X, Y Z are in fractional unit cell parameters. The hexagonal unit cell parameters are $a=b=6.038 \text{ \AA}$, and $c=11.361 \text{ \AA}$.

Ion	Position	X	Y	Z
Lu(1)	2	0	0	.2746
Lu(2)	4	0.3333	0.6667	0.2311
Mn	6	0	0.3355	0
O(1)	6	0	0.307	0.165
O(2)	6	0	0.3614	-0.163
O(3)	2	0	0	-0.0277
O(4)	4	0.3333	0.6667	0.0198

the crystal change its space group from $P6_3/mmc \{D_{6h}^4\}$ to $P6_3cm \{C_{6v}^3\}$ [112]. X-ray diffraction has been used to measure the tilt and the buckling [110, 113, 111]. Table 4.1 gives the structural parameters of the crystal [111]. Fig. 4.1 shows the crystal structure of LuMnO_3 . The left panel is the top view along the c-axis of the crystal and the right panel is the side view. In these graphs, the large, medium-sized, and small balls represent the Lu, Mn, and O ions respectively. For the Lu ions, the gray balls represent Lu(1) ions and black balls represents Lu(2) ions. The oxygen ion above the Mn ion is labeled O1 and the oxygen ion under the Mn ion is labeled O2. The oxygen ion between the two Lu(1) ions is labeled O3 and the oxygen ions between the two Lu(2) ions is labeled O4.

In the LuMnO_3 crystal, the Mn ions are surround by three in-plane and two apical oxygen ions. The d-orbital of the Mn ion splits into 3 groups: d_{xz} , d_{yz} ; d_{xy} , $d_{x^2-y^2}$; and $d_{3z^2-r^2}$ in order of increasing energy [75]. With strong bonding to the in-plane oxygen ion, the rotational symmetry of d_{xy} , $d_{x^2-y^2}$ is broken, which causes the absorption of photons polarized in the plane to excite the transition from d_{xy} , x^2-y^2 to $d_{3z^2-r^2}$. The splitting between d_{xy} , x^2-y^2 and $d_{3z^2-r^2}$ is about 1.58 eV at room temperature [75] and the energy splitting between d_{xz} , yz , and d_{xy} , x^2-y^2 is about 1 eV [7]. Fig. 4.2 shows the energy splitting of the Mn d electrons and the absorption spectrum of LuMnO_3 when the light is polarized in the a-b plane of the crystal. The absorption peak in Fig. 4.2 is

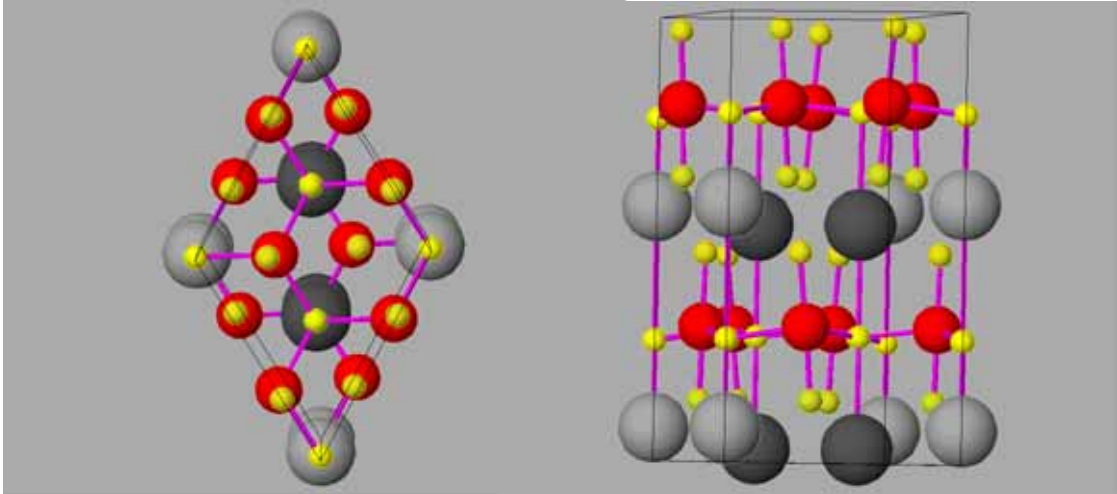


Figure 4.1: Schematic of unit cell structure of LuMnO_3 crystal. The left is the top view along the c -axis and the right is the side view. There are 30 atoms in a unit cell of LuMnO_3 crystal, including 6 Lu ions, 6 Mn ions and 18 oxygen ions. In the figure, the big black and gray balls represent the Lu ions, the middle size balls with red color represent the Mn ions and the small yellow balls represent the oxygen ions.

due to the transition from Mn d_{xy}, x^2-y^2 to $d_{3z^2-r^2}$ [75]. When the polarization of the light is parallel to the c axis, no such absorption peak has been observed [75].

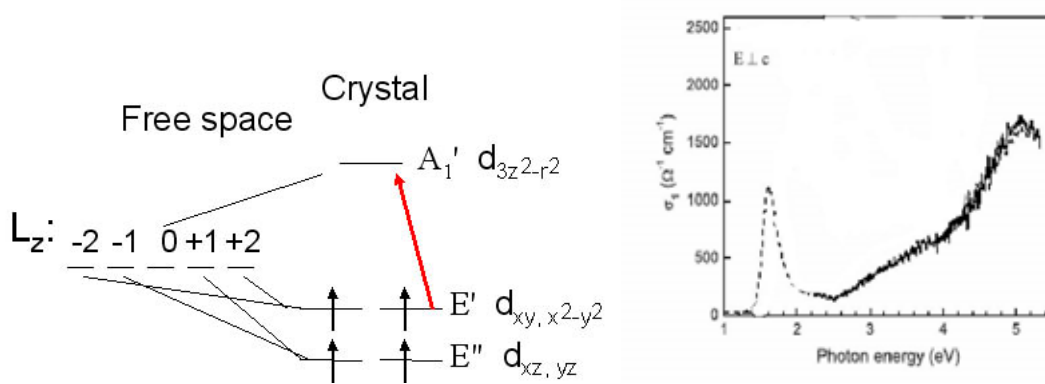


Figure 4.2: The splitting of d orbital energy level of Mn ion. Left: diagram of the energy level splitting of the manganese d orbital. Right: the absorption spectrum of LuMnO_3 with the light polarized in the a - b plane of the crystal. The absorption peak at 1.58 eV is due to the transition from d_{xy}, x^2-y^2 to $d_{3z^2-r^2}$. The measurement temperature is 300 K [75].

4.1.2 Anti-Ferromagnetic Properties

At low temperatures (below 90 K) [114], LuMnO_3 is anti-ferromagnetic. Above 90 K, it exhibits paramagnetic properties. Shamra *et al.* have measured the temperature dependence of the thermal conductivity, which shows the magnetic phase transition as an inflection point on the curve [114]. There are several methods that have been used to study the phase transition in the hexagonal multiferroic material, for example: temperature or magnetic field dependence of the second harmonic generation [115, 116], neutron diffraction [117, 118], magnetic susceptibility [119], dielectric constant [120, 121], specific heat constant [122], thermal expansion [123] and even the Raman and IR spectrum [75, 124].

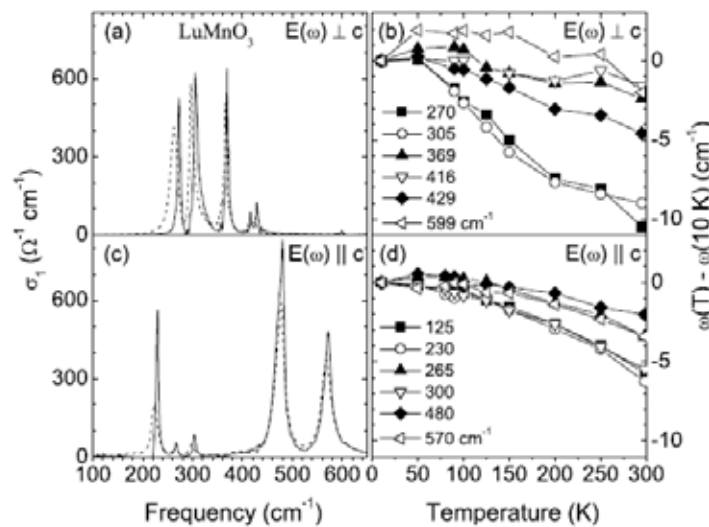


Figure 4.3: IR spectra of LuMnO_3 from reference [75]. (a) and (c): Real part of the optical conductivity of LuMnO_3 at 10 K (solid curves) and 300 K (dashed curves). (b) and (d): temperature shifts of the phonon frequencies. Two phonon at frequencies 270 and 305 cm^{-1} exhibit a large blueshift at the Neel temperature

The magnetic order originates from the Mn ion's d electron. As shown in Fig. 4.2, four Mn d electrons occupy four different orbitals with parallel spins (Hund's rules). The exchange interaction between manganese ions in the triangular lattice causes the anti-ferromagnetism [113, 125]. The super-exchange interaction between Mn ions also leads to an extra blueshift of 0.1 eV in the Mn d-d transition at the Neel temperature

[75]. The spin-phonon coupling leads to an anomalous blueshift of some LO phonon frequencies [75], which is shown in Fig. 4.3.

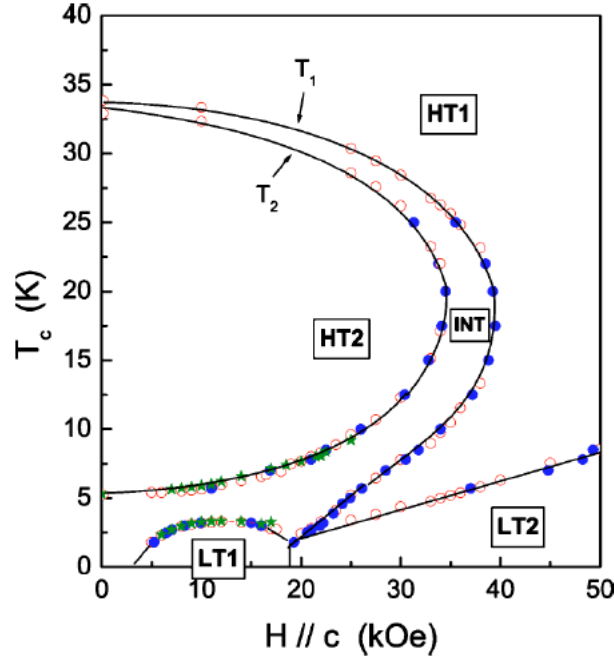


Figure 4.4: Magnetic phase diagram of hexagonal HoMnO_3 for a magnetic field H parallel to z from reference [119]. The different symbols in the curves are from different measurement methods.

The spins of Mn ions in the unit cell have four one-dimensional representations which are labeled A1, A2, B1 and B2. These spin orderings represent different antiferromagnetic phases. The phase changes among the A (including A1:LT1, A2:LT2), B1 (HT2), and B2 (HT1) were observed by optical second harmonic generation with the laser beam direction parallel to c axis in the HoMnO_3 which has a similar structure as LuMnO_3 [115, 126]. An intermediate temperature phase, also shown in Fig. 4.4 [119], was found between the HT2 and HT1 phases by several methods, including neutron scattering [118], magnetization, ac susceptibility, heat capacity and dielectric constant measurements [119, 120]. This intermediate state is produced by indirect coupling between ferroelectric and antiferromagnetic orders [121]. When the temperature is not very low (> 8 K), the spins of the Ho ions do not need to be count in, therefore, the antiferromagnetic properties of HoMnO_3 is very similar to LuMnO_3 .

4.1.3 Ferroelectricity

The ferroelectric order of LuMnO_3 is retained to 1000 K as shown by x-ray diffraction [113]. Due to a high Curie temperature, the phase diagram for the ferroelectric state and paraelectric state has not been mapped out by experimental methods. The theory of the ferroelectric transition and its mechanisms was discussed with a symmetry analysis [112, 127]. The most likely path is a zone-boundary mode that triples the unit cell (K_3), moving the structure from the paraelectric $P6_3/mmc \{D_{6h}^4\}$ space group to ferroelectric $P6_3cm \{C_{6v}^3\}$ space group [127, 112]. Katusuji *et al* attributed anomalous changes in the specific heat and the dielectric constant at the Neel temperature to coupling between the magnetic order and the ferroelectric order [128]. Others believe that these anomalies are caused by the geometric constraints of the crystal. The coupling between the anti-ferromagnetic order and ferroelectric order is weak since the magnetic exchange coupling is predominantly in the *ab* plane and the electric dipole moments are along the *c* axis [129]. The interaction between the ferromagnetic order and the ferroelectric order makes multiferroic materials potential magneto-electric switching materials [14, 130].

4.2 Experimental Procedures and Results

Pure polycrystalline hexagonal LuMnO_3 was synthesized by a solid-state reaction of stoichiometric amounts of Lu_2O_3 99.99% and MnO_2 99.99%, and further annealed for 24 hour at 1120° C in oxygen atmosphere. Single crystals of LuMnO_3 were grown by Bi_2O_3 flux in a Pt crucible. The flux was mixed with the pure polycrystalline hexagonal LuMnO_3 powder, then held at 1280° C for 5 hours and slowly cooled down to 930 °C at a rate of 2 °C per hour. Hexagonal crystals grew in the form of thin platelets with large (0001) (*a-b*) faces ¹. Then, the samples were cleaved into platelet samples with about 0.1 mm thickness, about 3 mm in width and 5 mm in length. Both reflectivity

¹The crystal were grown by Dr. Namjun Hur.

change and differential reflectivity change methods are described in detail in section 2.2. The incidence angles of both pump and probe beam were about 5° and the angle between the pump and probe beam was also about 5° .

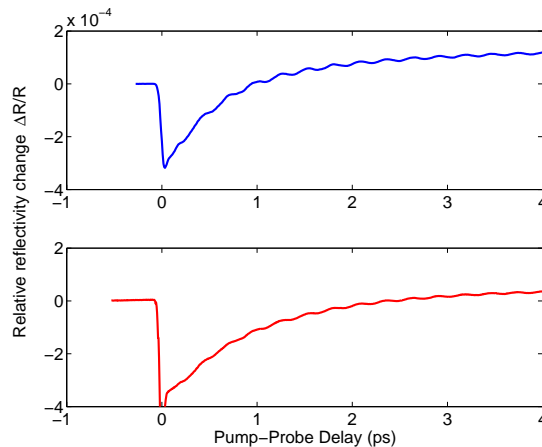


Figure 4.5: Reflectivity changes of LuMnO_3 crystal from a-b face at room temperature. The blue curve(upper) is measured with pump beam s-polarized and the probe beam p-polarized. The red curve (bottom) is measured with both pump and probe beams p-polarized.

4.2.1 Results of a-b Face

In Fig. 4.5, the blue curve (upper) is the reflectivity change as function of delay time obtained from the a-b face of the crystal with the pump beam s-polarized and the probe beam p-polarized. There is a sharp drop when the pump-probe delay is zero, relaxing back as the delay increases on the blue curve in addition to oscillation. The red curve (bottom) is the reflectivity change as a function of the delay time obtained from the a-b face of the crystal with both pump beam and probe beam s-polarized. There is a sharp spike (6×10^{-4}) at zero delay time in addition to a sharp drop and oscillations. This sharp spike is called the coherent optical response which is due to coherent electronic coupling of the pump and probe fields via the nonlinear susceptibility of the sample. When we changed the polarization of probe beam to s-polarization, the shape of the data were similar. The only difference is that the optical coherent peak appears in the

situation that the pump beam is *s*-polarized. The relaxation time of the drop is 0.80 ± 0.2 ps.

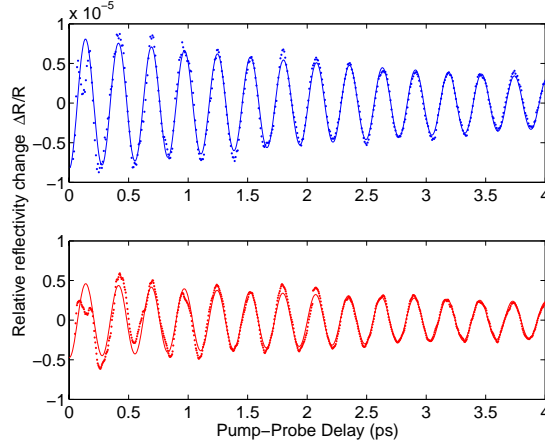


Figure 4.6: Oscillatory components of the reflectivity curves of Fig. 4.5. Those oscillations have a frequency of 3.61 THz and an initial phase close to π .

Fig. 4.6 shows the oscillatory components of the reflectivity curves of Fig. 4.5. The dots are the original data. Exponentially decaying cosine curves were used to fit the data, which are the lines in the figure. The blue (upper) curve in Fig 4.6 was acquired on the a-b face with pump *p*-polarized and probe *s*-polarized. It was fitted with $A_0 \cos(22.7t - 3.13) \exp(-.238t)$ (*t* in ps), which means the initial phase is 0.996π and the oscillation frequency is 3.61 THz (120.3 cm^{-1}). The oscillatory components acquired from the a-b face have an average initial phase of $(0.956 \pm 0.05) \pi$ and average frequency 3.61 ± 0.04 THz for all pump-probe polarization directions. We did not observe any oscillations in the reflectivity change curves from the a-b face when we used the differential measurement as described in Section 2.2.

4.2.2 Results of a-c Face

The reflectivity change curves measured from the cleavage face (01 $\bar{1}$ 0) (a-c face) have different shapes. A curve with both a sharp drop and oscillations was obtained when both pump and probe were polarized perpendicular to the *c* axis of the crystal, which is shown as the blue curve (upper) in Fig. 4.7. When the pump beam was polarized

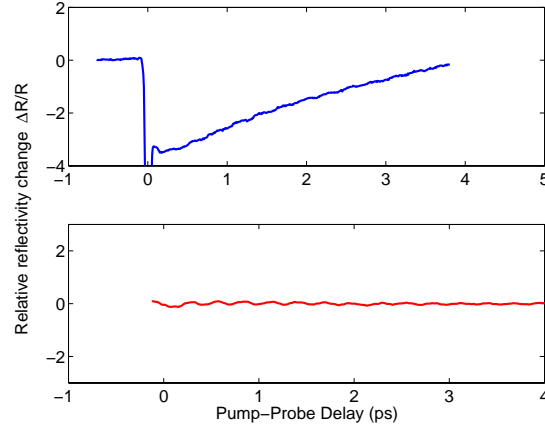


Figure 4.7: Pump-probe Spectra of LuMnO_3 from a-c face at room temperature. The blue curve (upper) is measured with both pump and prob beams perpendicular to the c axis. The red curve (bottom) is measured with the pump beam polarized perpendicular and probe beam polarized parallel to the c axis.

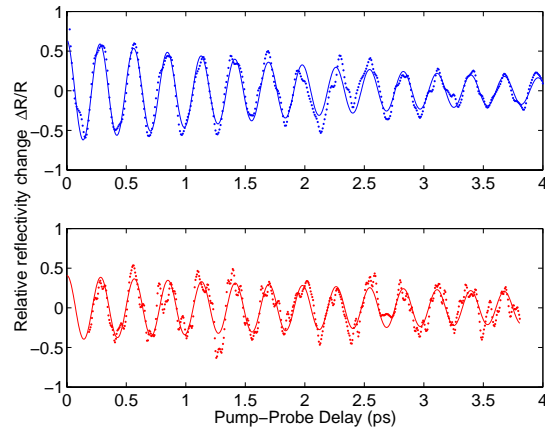


Figure 4.8: Oscillatory component of the reflectivity change curve of Fig. 4.7. Those oscillations have a frequency of 3.54 THz and an initial phase close to 0.

perpendicular to the c axis while the probe beam was polarized parallel to the c axis, there was no drop in the reflectivity changes curve shown in the red curve in Fig 4.7, but nevertheless there were coherent phonon oscillations. Neither a drop nor oscillations appeared on the reflectivity curves when the polarization of the pump beam was parallel to the c axis. The oscillation frequency was 3.54 ± 0.02 THz (118 cm^{-1}) with an initial phase $0.004 \pm 0.028 \pi$. Compared to the results from the a-b face, the frequency was slightly lower, and the initial phase was shifted by approximately π . The blue curve (upper) in Fig. 4.8 is the oscillatory part of the reflectivity change curve (blue) in Fig.

4.7. The red curve in Fig. 4.8 is the oscillatory component acquired from the a-c plane with the pump beam polarized perpendicular and the probe polarized parallel to the c axis. The average initial phase with probe polarization parallel to the c-axis is 0.008π while the average initial phase with the probe beam polarization perpendicular to the c-axis is -0.02π . The difference is in the range of the measurement error.

4.3 Symmetry Analysis of Phonon Spectra

The space group of ferroelectric LuMnO₃ crystal is $P6_3cm \{C_{6v}^3\}$, and Table 4.2 is the character table of C_{3v} the corresponding point group ². The IR active modes are A_1

Table 4.2: Character table of $\{C_{6v}\}$ point group

Mode	E	$2C_6(z)$	$2C_3(z)$	$C_2(z)$	$3\sigma_v$	$3\sigma_d$
A_1	1	1	1	1	1	1
A_2	1	1	1	1	-1	-1
B_1	1	-1	1	-1	1	-1
B_2	1	-1	1	-1	-1	1
E_1	2	1	-1	-2	0	0
E_2	2	-1	-1	2	0	0

and E_1 . The A_1 mode is polarized in the z direction, while the E_1 mode is polarized in the a-b plane for IR absorption. The Raman active modes are A_1 , E_1 and E_2 . Their Raman tensors are giving by the following [131]:

$$A_1 : \begin{pmatrix} a & 0 & 0 \\ 0 & a & 0 \\ 0 & 0 & b \end{pmatrix}$$

$$E_1(x) : \begin{pmatrix} 0 & 0 & c \\ 0 & 0 & 0 \\ c & 0 & 0 \end{pmatrix} \quad E_1(y) : \begin{pmatrix} 0 & 0 & 0 \\ 0 & 0 & c \\ 0 & c & 0 \end{pmatrix}$$

²Bilbao crystal server, <http://www.cryst.ehu.es/>

$$E_2(xy) : \begin{pmatrix} 0 & d & 0 \\ d & 0 & 0 \\ 0 & 0 & 0 \end{pmatrix} \quad E_2(x^2 - y^2) : \begin{pmatrix} -d & 0 & 0 \\ 0 & d & 0 \\ 0 & 0 & 0 \end{pmatrix}$$

From these Raman tensors, we can obtain the selection rules of Raman scattering as shown in Table 4.3. Since the modulations in the reflectivity that we measured are

Table 4.3: Raman scattering configuration and the measured phonon symmetry

Incident direction	incident polarization	scattered polarization	scattered direction	symmetry modes
z	x	x	\bar{z}	A_1, E_2
z	x	y	\bar{z}	E_2
x	y	z	\bar{x}	E_1
x	y	y	\bar{x}	A_1, E_2
x	z	y	\bar{x}	E_1
x	z	z	\bar{x}	A_1

caused by motions in the phonon displacement coordinate, which are related to refractive index modulations, the reflectivity change curves are only sensitive to those modes where the refractive index has a first order dependence on the phonon displacement. The derivative of the polarizability with respect to the phonon displacement coordinate is the Raman tensor, so the phonon oscillation we measured are Raman active modes. The "incident" beam in Table 4.3 corresponds to the incident probe beam in our experiments while the "scattered" beam in Table 4.3 is the reflected probe beam in the experiments. Thus we can use the incident probe polarizations, the reflected probe polarization and Table 4.3 to obtain the symmetry of the coherent phonon mode. We can exclude E_2 symmetry for the phonon measured from the a-b face by the fact that the initial phase is independent of the probe polarization. An E_2 phonon should reverse its phase when the probe polarization is rotated by 90° . The E_1 modes is not sensitive to light only polarized in the a-b plane. Thus, the symmetry mode of the phonon measured from the a-b face must be A_1 .

Since we measured the oscillation in the reflectivity change from the a-c face with the probe beam polarized parallel to the c axis, the E_2 mode can be excluded. The E_1

mode can also be excluded since we measured oscillations with the incident and the reflected probe beam polarized in the same direction. Thus, the phonon we measured from the ac plane is also an A_1 mode.

The LuMnO_3 unit cell has 30 atoms, implying 90 degrees of freedom. Table 4.4 lists the character values of these degrees of freedom at the Γ point. The vector of

Table 4.4: Total character value at Γ point

Mode	E	$2C_6(z)$	$2C_3(z)$	$C_2(z)$	$3\sigma_v$	$3\sigma_d$
Γ_t	90	0	0	0	10	0

characters can be decomposed into the irreducible representation of characters in the character table by

$$\Gamma_t = 10A_1 + 5A_2 + 10B_1 + 5B_2 + 15E_1 + 15E_2$$

These means that LuMnO_3 crystal has 60 Γ point phonon modes. The acoustic phonon modes are one A_1 and one E_1 mode [124]. Thus, the Raman active optical modes Γ_R are $9A_1 + 14E_1 + 15E_2$, and the IR active optical modes Γ_{IR} are $9A_1 + 14E_1$. The other modes $5A_2 + 10B_1 + 5B_2$ are silent. When propagated in the z direction, the A_1 phonon is a longitudinal optical (LO) mode and the E_2 modes phonon are transverse optical (TO) modes. When the propagation direction is in the a-b plane, the excited A_1 phonon is a TO mode and the E_1 and E_2 modes each have both TO and LO polarization.

4.4 Shell Model Calculation

The shell model of lattice dynamic is a phenomenological model based on inter atomic potential functions [132]. In this model, each ion has a massless "shell" and a massive core. The charge of the ion is distributed between the core and the shell. If the core and the shell have some displacement with respect to each other, a dipole moment is produced [133]. The interaction between the core and its shell is treated as a harmonic potential with a force constant k. The charge distribution and the force

constant are parameters to fit the experimental phonon mode frequencies. Those constants can be transferred from some simple ionic crystals. The interaction between the ions are treated as a combination of long-range Coulomb potentials and a short-range Born-Mayer-Buckingham potential in the form of:

$$V = A\exp(-r/\rho) - \frac{c}{r^6} \quad (4.1)$$

Here, r is the interionic separation. The constants A , ρ , c are fitting parameters, which may be obtained from some well studied simple ionic materials [124, 134].

Table 4.5: Shell model parameters

Ion	$Z(e)$	$Y(e)$	k (eV/Å ²)	Ionic Pair	a (eV)	b (Å)	c (eVÅ ⁶)
Lu	2.85	1.7	50.45	Lu-O	1668	0.32624	0
Mn	2.85	3.0	35.98	Mn-O	1928	0.29504	0
O	-1.9	-3.0	64.8	O-O	22764	0.14901	20.37

In our calculation, the lattice parameters of the LuMnO₃ crystal are adopted from reference [135] and the atomic positions come from Table 4.1. The shell model parameters from reference [124, 134, 132] were used as starting parameters. The shell model code ³ in reference [133] was used to calculate phonon frequencies and eigenvectors. A MATLAB program was written to assign phonon symmetries. Then, the calculated phonon frequencies were compared to IR absorption spectra [75] of the same symmetry. The shell model parameters were optimized to fit the IR spectra. Table 4.5 shows our final shell model parameters. Table 4.6 and Table 4.7 are the calculated phonon frequencies and the major ion motion in their eigenvectors. In Table 4.6, the IR frequencies at 300 K are from reference [75], and the Raman frequencies from Girsh Bloomberg at Alcatel-Lucent Bell Laboratories.

In the calculation, the temperature dependence of phonon frequencies is very small. The possible reason is that the temperature dependence of the phonon frequencies is

³The shell model code was provided by Dr. M.B. Taylor, Bristol University, UK

Mode symmetry	Calc. (cm^{-1})		Expt. (cm^{-1})		Direction and sign of largest atomic displacement
	LO	TO	IR	Raman	
A_1	124	123	119		+z(Lu2), -z(Lu1)
A_1	251	208	223		+z(Mn), -z(Lu1)
A_1	267	260	261	260	Rot _{xy} (MnO ₅)
A_1	283	280	295		x(Mn), z(O3)
A_1	421	393			z(O4, O3)
A_1	460	435		451	+z(Mn), -z(O3, O4)
A_1	475	472	478		xy (O1, O2), -z(O3)
A_1	620	591	568		+z(Mn, O3, O4), -z (O1, O2)
A_1	676	676		686	+z(O1), -z(O2)
E_1	119	119			+x,-y(Lu), +y,-x(Mn, O3,O4)
E_1	137	137			+x,+y (Lu1), x,y (Lu2)
E_1	141	141	161		+x,-y (Lu1), -x, +y (Lu2)
E_1	235	234			-x,+y(Mn),
E_1	251	249			x,y (Lu2, O2), Z(Mn)
E_1	336	269			+x (O2), -y(O2)
E_1	363	336			-x,+y(O3), +x,-y(O2)
E_1	402	369	366		-x,+y(O1), +x, -y(O2)
E_1	407	404	414/424		x, y (O1, O2)
E_1	496	465			+x,+y(O3), -x,-y(Mn)
E_1	529	497			-x,+y(O3), +x,-y(O4)
E_1	552	552			+x,+y(O3),-x,-y(O4)
E_1	573	573	597		z(O1,O2,Mn)
E_1	639	639			-x,-y(O3),+x, +y(O4)

Table 4.6: Calculated values of A_1 and E_1 mode frequencies compared with experimental values, and calculated phonon eigenvector properties

caused by structure changes and spin-phonon coupling [129, 75]. Realistically, therefore, we may need to adjust the crystal structure with temperature which was not done in the calculation.

4.5 Discussion and Conclusion

4.5.1 Phonon Excitation Mechanism

The reflectivity drop at zero delay time is attributed to the partial saturation of the Mn d-d transition. The center wavelength of the femtosecond pulse is at 800nm, which is slightly off the resonance absorption peak of the Mn d-d transition. As the Mn d-d

Mode symmetry	Calc.(cm ⁻¹) LO TO	Direction and sign of largest atomic displacement
E_2	68	x,y(Lu)
E_2	114	x, y(Mn,O3,O4)
E_2	131	x,y(Lu)
E_2	144	x,y (Lu1)
E_2	233	x,y(Mn)
E_2	251	z (Mn)
E_2	271	x,y (O1,O2)
E_2	347	x,y(O1,O2,O4)
E_2	356	x,y(O1,O2)
E_2	400	x,y(O)
E_2	469	x,y(O3)
E_2	490	x,y(O4)
E_2	555	x,y(O3,O4)
E_2	576	x,y(O4), z(Mn,O1,O2)
E_2	638	x,y(O3,O4),z(o1,O2)

Table 4.7: Calculated values of E_2 mode frequencies and their largest atomic displacements.

transition is excited, the population of the Mn ground state d_{xy}, x^2-y^2 decreases and the population of the excited states increases, which lowers the absorption peak, therefore decreases the reflectivity. When the polarization of the probe beam is parallel to the c axis, the Mn d-d transition can not be excited. Thus, in this geometry, saturation of the Mn $d_{xy}, x^2-y^2 \rightarrow d_{3z^2-r^2}$ transition does not occur. This is confirmed by the fact that the reflectivity does not show a sudden change at zero delay time when the probe beam is parallel to the c axis.

When the polarization of the pump beam is perpendicular to the c-axis, the phonon oscillation is observed while no phonon oscillation is observed when the polarization of the pump beam is parallel to the c axis. The excitation of the coherent phonon follows the selection rule of the Mn d-d transition. The initial phase of the phonon oscillation is close to an integer multiple of π indicating a displacive mechanism associated with an electronic excitation of life time much larger than the phonon oscillation period. These considerations strongly suggest that the driving force of the A_1 phonon excitation is the Mn d-d transition, which couples to the phonon coordinate either via a resonant TSRS

or a displacive hot electron mechanism.

4.5.2 Phonon Coordinate Motion

The coherent phonon measured in the a-b face is an A_1 symmetry phonon with a frequency of 120 cm^{-1} . The phonon measured from the a-c face is also an A_1 symmetry phonon with a frequency of 118 cm^{-1} . According to the shell model calculation, the mode is identified as the lowest A_1 optical phonon mode, which involves the Lu1 and Lu2 ions vibrating along the c axis in opposite directions as shown in Fig. 4.9. From the motion of the ions, longitudinal optical (LO) mode polarization can be assigned to the phonon measured from the a-b face, and the phonon measured from the a-c face can be assigned to the transverse (TO) mode, as shown in Fig. 4.11.

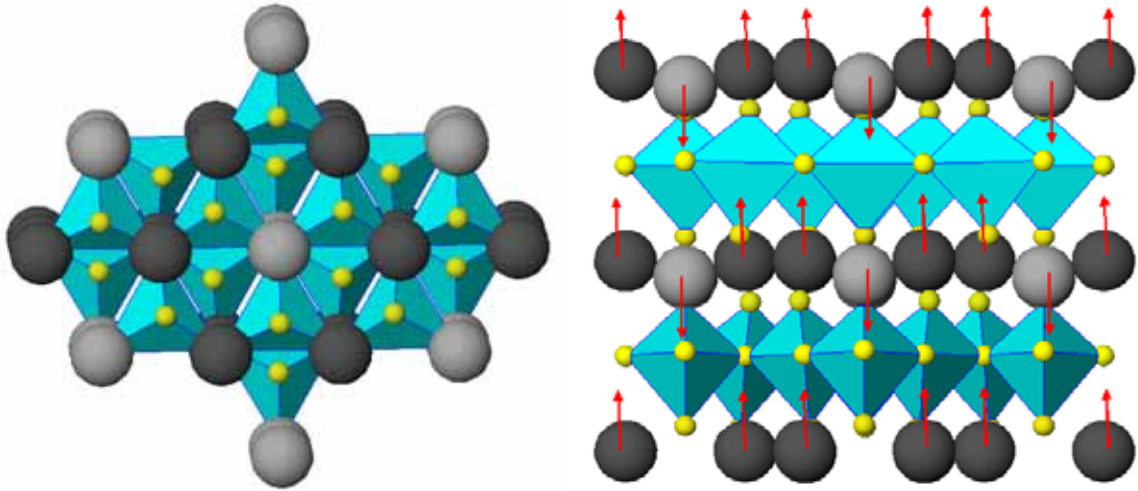


Figure 4.9: schematic view of the structure of hexagonal LuMnO_3 . On the left is the top view and on the right is the side view. MnO_5 is represented by triangular bi-pyramids. The oxygens are at the apex of the bi-pyramids with the Mn ion in the center. Lu1 and Lu2 are represented by the gray and black balls, respectively. The displacively excited A_1 phonon in our experiment involves Lu1 and Lu2 ions vibrating along the c axis as shown by the red arrow in the right figure.

An initial phase close to π or 0 suggests that the coherent phonon motion is excited by changing the equilibrium ion positions (displacive excitation). A possible pathway for this excitation process is described below. When an 800 nm photon excites the

electronic transition from d_{xy, x^2-y^2} to $d_{3z^2-r^2}$, electronic charge is transferred from the in-plane oxygen ions to the apical oxygen ions, because of covalent bonding between the in-plane 3d orbital of the Mn ion and the in-plane oxygen ions. The in-plane oxygens then exert a more repulsive force on the nearest Lu ions, resulting in a change of the equilibrium position of Lu ions. The phonon eigenvector resembles the static distortion that the crystal undergoes when the crystal changes its phase from the prototypic to the ferroelectric structure. As we project the ferroelectric distortion on to the eigenvectors of the A_1 phonons, the A_1 phonon with Lu ions moving along c axis has 80% of the ferroelectric distortion character. The other A_1 phonons with higher frequency provides the remaining 20%. So we conclude that the coherently excited phonon mode is the soft mode mediating the transition from prototypic $P6_3/mmc$ phase to the ferroelectric $P6_3cm$ phase.

The driving force of the ferroelectric phase transition was identified as the atomic motion along two normal mode coordinates of different symmetries, labeled as Γ_2^- and K_3 according to the irreducible representations of the prototypic $P6_3mmc$ space group [112]. The K_3 symmetry mode is a unit cell tripling, Brillouin-zone boundary (K-point) mode involving the bucking of rare earth ion planes and rotation of MnO_5 bipyramids. Static distortion along the K_3 coordinate breaks the inversion symmetry, but it does not involve a first-order ferroelectric polarization since zone boundary modes are nonpolar. A finite distortion along the K_3 coordinate allows for a third order polarization, and enables coupling between the K_3 mode and polar Γ_2^- modes, since both K_3 and Γ_2^- reduce to the same totally symmetric (Γ_1) irreducible representation ($k=0$ and A_1 point group) into the $P6_3cm$ space group. In order to relate the coherent phonon mode observed in our experiment to these static distortion modes, we decompose both the static distortion and the calculated phonon eigenvectors into symmetry components corresponding to the prototypic $P6_3/mmc$ structure. The result is shown in Table 4.8. The static distortion exhibits predominantly the K_3 symmetry (98%) and

Static distortion					
	Total	Γ_1^+	Γ_2^-	K_1	K_3
Lu1(z)	0.485	0	-0.035	0	0.521
Lu2(z)	-0.296	0	-0.035	0	-0.260
Mn(x)	0.012	0	0	0.012	0
Mn(z)	0.024	0	0.024	0	0
O1(x)	-0.076	0	0	0.003	-0.079
O1(z)	0.019	-0.000	0.0197	0	0
O2(x)	0.081	0	0	0.003	0.079
O2(z)	0.019	0.000	0.019	0	0
O3(z)	-0.137	0	0.035	0	-0.172
O4(z)	0.121	0	0.035	0	0.086
Weight	1.000	0.000	0.023	0.001	0.977

123 cm ⁻¹ phonon eigenvector					
	Total	Γ_1^+	Γ_2^-	K_1	K_3
Lu1(z)	0.562	0	-0.013	0	0.576
Lu2(z)	-0.301	0	-0.013	0	-0.288
Mn(x)	0.016	0	0	0.016	0
Mn(z)	0.009	0	0.009	0	0
O1(x)	-0.005	0		-0.005	0.000
O1(z)	0.002	-0.002	0.004	0	0
O2(x)	-0.005	0		-0.005	0.000
O2(z)	0.006	0.002	0.004	0	0
O3(z)	0.033	0	0.019	0	0.014
O4(z)	0.012	0	0.019	0	-0.007
Weight	1.000	0.000	0.004	0.002	0.994

Table 4.8: Decomposition of the static distortion in the ferroelectric $P6_3cm$ structure and the 123 cm⁻¹ TO phonon eigenvector into irreducible representations of the $P6_3/mmc$ space group. Γ_1^+ and Γ_2^- are Brillouin-zone center modes, while K_1 and K_3 are unit cell tripling, Brillouin-zone boundary modes. The ferroelectric polarization is due to a distortion of Γ_2^- symmetry, which is the only polar mode symmetry involved. In order to directly compare these modes, both the static distortion mode and the phonon eigenvector are expressed as atomic displacements, weighted by the square root of the atomic mass, and normalized to unity upon summation over all 30 atoms in the $P6_3cm$ unit cell. The decomposition of the 124 cm⁻¹ LO phonon eigenvector is essentially the same as that of the TO phonon.

only a small admixture of the polar Γ_2^- symmetry (2%). Similarly, the calculated coherent phonon is essentially motion along the K_3 soft-mode coordinate that drives the ferroelectric transition, with a small amount of admixture of polar Γ_2^- motion.

4.5.3 Depolarization Field Effect

From the decomposition of the phonon eigenvector, the amount of polar Γ_2^- mode component is small. However, it has important consequences. This small polar component makes the mode infrared active and further is responsible for a small frequency splitting between the LO and TO propagation geometries. This is due to the additional restoring force exerted on the ions by the electric depolarization field present in the LO mode, but absent in the TO mode. Since the electric polarization field is along the c-axis, the LO phonon propagates along the c-axis and the TO phonon propagates in the a-b plane. Although the vector of the coherent phonon is not well defined in the thin, near-surface slab of the excited crystal, we can still distinguish the LO and TO modes by the propagation direction of the laser beam. In the experiment, the TO mode measured from the a-c plane has a frequency of 118 cm^{-1} while the LO mode measured from the a-b plane has a frequency of 120 cm^{-1} . The splitting between the LO and TO mode (2 cm^{-1}) is consistent with the small splitting calculated in the shell model and the expected weak mode polarity caused by the small Γ_2^- symmetry component.

In addition to the frequency splitting, we also observed a remarkable reversal of the initial phase of the oscillation between the reflectivity change curves measured from the a-b face and the a-c face. There are several possible factors which could influence the initial phase of the oscillation in the reflectivity change curves. However, if we compare the two oscillatory components in Fig. 4.10, we can exclude all possibilities except the vector of the phonon. These two curves were obtained in the same polarization geometry, with both pump and probe beams polarized in the a-b face with parallel polarization. The only difference is that the upper curve was obtained from the a-b

face while the lower one was obtained from the a-c face. As we discussed before, the phonon measured from the a-b face is assigned to the LO mode while that measured from the a-c plane is assigned to the TO mode.

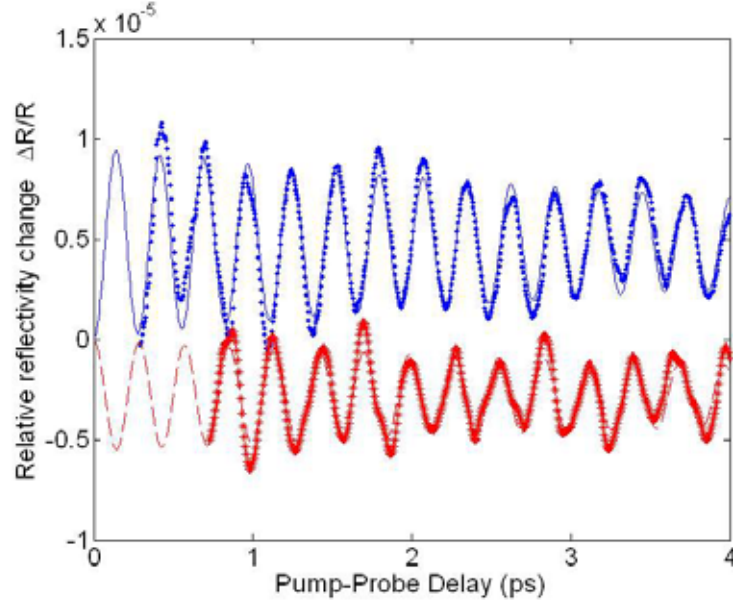


Figure 4.10: Oscillatory component of the reflectivity change curve. The blue curve (fitted by the solid line) is the oscillatory data acquired from the a-b face with both pump and probe s-polarized. Those oscillations have a frequency of 3.61 THz and an initial phase of π . The red curve (fitted by the dash line) is the oscillatory data acquired for the a-c plane, with a frequency of 3.54 THz and an initial phase close to zero. These two curves correspond to the same pump-probe polarization directions.

The reflectivity modulated by the phonon oscillation can be expressed phenomenologically in the form of [66, 70, 87, 88]:

$$\frac{\Delta R}{R} \propto rE + \frac{1}{\sqrt{2\pi}} \int_{-\infty}^{+\infty} d\Omega e^{i\Omega t} Q^*(\Omega) \chi^R \quad (4.2)$$

Where $Q^*(\Omega)$ is the Fourier transform of the normalized displacement of the lattice $Q(t)$, and χ^R is the Raman susceptibility tensor. The second term represents the phonon motion's direct contribution to the reflectivity. E is the macroscopic depolarization field induced by the polarization of the lattice and r is the high-frequency electro-optic coefficient of the crystal. If only a single mode of the phonon is excited,

equation 4.2 can be simplified to:

$$\frac{\Delta R}{R} \propto rE + \alpha Q(t)\chi^R \quad (4.3)$$

where α is a constant. In some polar crystals, the linear electro-optic effect is very strong. In the longitudinal coherent phonon, E corresponds to the coherent depolarization field as shown in Fig. 4.11 right, which has the same frequency as the lattice vibration. However, in the transverse mode, the depolarization field is essentially zero due to the large aspect ratio of the excited slab. In some references, the first term is explained as the fast electronic response [70, 136]. In many crystals, this term is the major cause of the coherent longitudinal mode phonon excitation and also can reverse the effect of the second term on the reflectivity change [70]. In the case of coherent phonons in LuMnO_3 , the oscillation measured from the a-c face is the effect of a TO phonon, which only contributes to the reflectivity change curve via the second term of the equation. The oscillations obtained from the a-b face are the result of a LO phonon, which contributes to the reflectivity change via both terms. The reversed initial phase of the phonon oscillation with respect to the TO phonon suggests that the first term contributes more to the reflectivity change than the second term, and that two terms have opposite signs.

As we discussed in the section 4.5.1, the excitation mechanism can be either a resonant TSRS, or a displacive hot electron mechanism, even a mixture of the two. It is also possible that the phase reversal of the coherent phonon oscillation can originate from the excitation mechanism. In this scenario, the TO coherent phonon is excited by a resonant TSRS mechanism, while the LO mode is excited by a combination of TSRS and an electric-field mediated mechanism. In this latter mechanism, electronic excitation leads to a sudden change in ferroelectric polarization, which gives rise to a depolarization field in the LO geometry, which in turn couples to the IR active phonon. In the TO mode, the depolarization field is absent, thus the coherent phonon excitation can be the TSRS only. Provided that the field mediated mechanism is more efficient than the TSRS mechanism and two mechanisms lead the phonon displacements of opposite

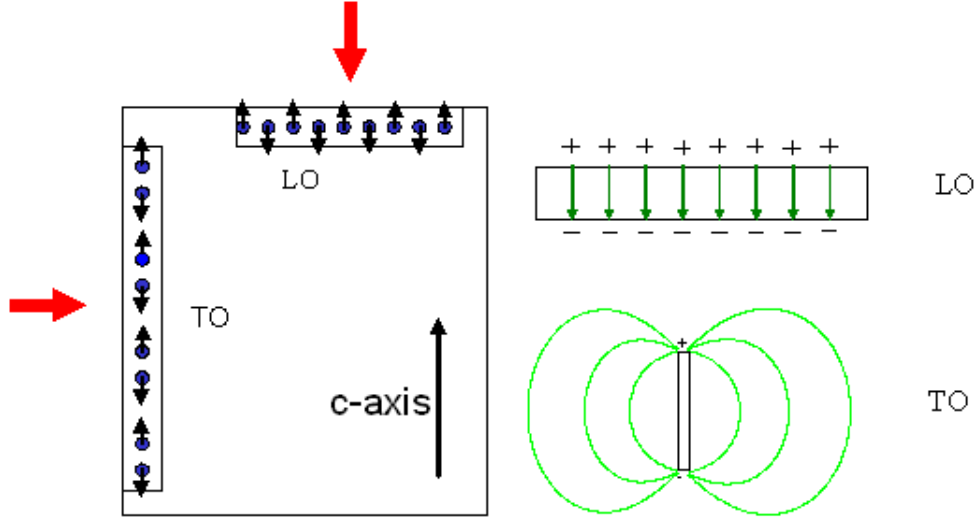


Figure 4.11: Schematic view of LO and TO phonon modes. The left diagram shows how the phonon modes are assigned. When the coherent phonon is excited on the ab face, the vector of the phonon is parallel to the c axis and the motion is also parallel to the c axis, thus it is assigned to the LO mode. On the other hand, when it is measured from the ac face, the vector is perpendicular to the phonon polarization, thus it is a TO mode. When the coherent LO phonons are excited, the ions in the excited slab move in phase, thus forming a macroscopic electric field, which is called depolarization field and has the same frequency with phonon motion. When TO phonon is excited, the depolarization field is zero due to the large aspect ratio.

sign, the observed phase reversal would be the result. In the similar crystal YMnO_3 , the corresponding A_1 phonon mode exhibits a much larger Raman cross section than any other modes whose frequencies are lower than 15 THz. This may explain why only this phonon mode (A_1 , 120 cm^{-1}) can be observed in the pump probe spectra.

4.5.4 Summary

In summary, we have used femtosecond pump-probe techniques to investigate the femtosecond and picosecond dynamics of LuMnO_3 crystal. The absorption of 800 nm light results a drop of the reflectivity of light polarized perpendicular to the c axis due to partial saturation of the $\text{Mn } d_{xy, x^2-y^2} \rightarrow d_{3z^2-r^2}$ transition. However, the reflectivity of the light polarized parallel to c axis does not drop due to the direction of transition dipole. Upon the excitation of the $\text{Mn } d \rightarrow d$ transition, an A_1 symmetry phonon mode (TO:

118 cm^{-1} and LO: 120.3 cm^{-1}), which involves the Lu1 and Lu2 ions vibrating along the c axis with opposite phases, is coherently excited via a displacive mechanism. This phonon is identified as the soft mode, which drives the ferroelectric phase transition. The TO and the LO phonons exhibit opposite initial oscillation phase in the reflectivity change curve which is interpreted as an effect of the longitudinal depolarization field of the LO phonon via the linear electro-optical effect or the excitation mechanism.

Chapter 5

Summary and Future Work

5.1 Summary

Semiconductors and multiferroic materials are tremendously important both technologically and economically. It is very important to understand the microscopic ultrafast dynamics of both types of materials for future more advanced applications. In this thesis, we studied the ultrafast dynamics of two semiconductors GaAs and Ge, and one hexagonal multiferroic material, LuMnO_3 , with our ultrafast pump-probe optical spectroscopy, paying particular attention to the excitation mechanism of the coherent phonon.

There are three kinds of excitations contributing to the reflectivity change when GaAs or Ge single crystals are excited by a 25 femtosecond pulse with center wave length 800 nm. The first is the excitation and the relaxation of charge carriers, which exhibits a few-femtosecond rise or drop on the reflectivity change curves with a picosecond exponential relaxation. The second is the coherent optical response peak, which is the coherent electronic coupling of the pump and probe beam via the nonlinear susceptibility of the sample. The width of this peak is of the order of the autocorrelation peak width. The third is coherent phonon oscillation, which appears on the reflectivity change curve as a decaying cosine oscillation with an initial phase.

The probe beam polarization dependency of the coherent phonon in both GaAs and Ge is $\cos(2\theta)$, which satisfies the symmetry of T_2/T_{2g} phonon Raman tensor. The pump beam polarization dependency of the coherent phonon in Ge is also $\cos(2\theta)$, which is a direct evidence that the coherent phonon in Ge is excited by the Transient Stimulated

Raman Scattering mechanism. The initial phase of the coherent phonon in Ge crystal is $102 \pm 15^\circ$, which is consistent with the impulsive stimulated Raman scattering; any deviation from 90° are likely due to the fact that excitation is resonant and the lifetime of the resonant is greater than zero.

When the pump is polarized along the [100] or [010] directions, the initial phase of the coherent oscillation is $0 \pm 4^\circ$. As the pump polarization is rotated from the [1-10] direction to the [110] direction, the coherent phonon amplitude changes from the maximum value to the minimum value and the initial phase changes from a positive value to a negative value. The correlation analysis of the initial phase and the amplitude suggests that the excitation mechanism in GaAs is a combination of TSRS and surface field screening mechanism. In Ge crystal, the surface field is very weak because of the inversion symmetry of the crystal structure. The initial phase for TSRS mechanism is $109 \pm 4^\circ$. We used continuous wavelet transform (CWT) to analyze our calibrated experimental data and simulated reflectivity change curves. The frequency of cancellation in the CWT spectra (spectral hole) is determined by the initial phase of the phonon oscillations.

We also observed the relaxation of the Mn $d_{xy}, x^2-y^2 \rightarrow d_{3z^2-r^2}$ excitation with a time constant of $.8 \pm .2$ ps as well as the resonant excitation of a coherent phonon oscillations. The phonon modes, involving Lu ions moving along the c-axis, is of A_1 symmetry, and identified as the soft mode driving the ferroelectric transition. The excitation of the phonon follows the symmetry of the Mn $d_{xy}, x^2-y^2 \rightarrow d_{3z^2-r^2}$ transition instead of the symmetry of the phonon itself, and the initial phase of the phonon oscillation is very close to a integral multiple of π . All these observation suggest that the excitation mechanism could be TSRS, or a screening effect of photoexcited electrons, or a combination of two. We also observed a phase reversal between the reflectivity change curve of the LO phonon and of the TO phonon. This phase reversal is attributed either to linear electro-optic effect of the macroscopic depolarization field

accompanying the infrared active longitudinal phonon modes or the different excitation mechanism. Further experiments are proposed to exclude or prove the excitation mechanism and the explanation of the reversal of the initial phase.

5.2 Future Work

We studied the excitation of the coherent phonon with time resolution spectra in semiconducting and multiferroic materials. Excitation mechanism of these coherent phonon modes were discussed in microscopic view. Further experiments are needed to understand the physics of the coherent phonon excitation.

5.2.1 Future Work With GaAs and Ge

We measured pump-probe reflectivity change of semiconductors GaAs and Ge. To the best of our knowledge, this is the first time that a coherent phonon mode excited by both TSRS and the screening effect of photoexcited electrons were observed in the same experiment. A phenomenological explanation is that when the electric charge carrier is excited, it only excites the phonon following the selection rule of the phonon modes. As time goes on, the charge carrier is scattered by other charge carriers, and the momentum of the charge carrier changed, then these charge carriers can excite the coherent phonon in the DECP mechanism. In Cho's experiments [61], the excitation photon energy is about 2.0 eV, much higher than the band gap of the GaAs, implying that there are several channels to scatter the charge carriers, intra- and intervalley scatterings. This decreases the time to lose memory of the momentum of the initial excitation. As we expect at lower photon energy, the charge carriers can only be scattered intra valley, which resulting them to retain their momentum for a longer time. Thus the TSRS mechanism has a stronger effect on the excitation. The contribution of the TSRS mechanism makes the initial phase deviate from zero initial phase. The change of the absorption coefficient [105] and Raman scattering crosssection [106]

also support our explanations. To obtain a clear picture of the details, we need more experimental results with different pump wave lengths. First principle simulation of electronic-phonon, photon-phonon coupling and charge carrier scattering would also be helpful.

5.2.2 Future Work on Hexagonal Multiferroic Manganites

We measured the reflectivity change of LuMnO_3 crystal at room temperature. A coherent phonon, accompanying resonant excitation of the Mn $d_{xy, x^2-y^2} \rightarrow d_{3z^2-r^2}$ transition, is excited. At high temperature, there are several possible phase transition paths in the theory [112]. The phonon we observed is identified as the soft mode that drives the ferroelectric transition. It will be very interesting to study changes of this phonon mode at the temperature of the ferroelectric phase transition. There are two ways we can increase the sample temperature. The first one is to directly heat the sample up, and the second is to use a pump beam with high intensity to heat the sample locally. Furthermore, when the temperature of LuMnO_3 is lower than 90 K, antiferromagnetic order sets in. As the temperature is moved through phase transition, the resonant absorption peak undergoes an anomalous blue shift, which is due to the Mn-Mn superexchange interaction. The charge and orbital order may be kept for some time after electronic excitation when the material is antiferromagnetic [74]. It is very interesting to observe the pump-probe reflectivity change when the LuMnO_3 crystal is either at high or low temperature in regard to the coupling between charge, spin and phonon. Also it will be interesting to observe the coherent phonon's pump intensity dependence. In our experiments, we used the resonance absorption of the pump beam to excite the coherent phonon. The wavelength of the pump beam determined the absorption, which may change the resonant excitation cross-section of the different phonon modes.

We have studied the coherent phonon in LuMnO_3 . There are other materials with similar structures, for example, HoMnO_3 , YMnO_3 , and ErMnO_3 . All of them are multiferroic materials with hexagonal structure. It will be interesting to observe coherent

phonons in those materials at low temperatures. I am especially interested in HoMnO_3 since it has orthorhombic and hexagonal phase. The pump probe reflectivity changes of different structures of the same material may uncover some correlation between crystal structure and the phonon dynamics.

5.3 Conclusion

Ultrafast spectroscopy is an powerful experimental method, which provides temporally resolve phenomena at the timescale of the ionic and electronic motions. By using ultrafast spectroscopy, we studied the excitation, and relaxation of electrons, coherent phonons in the semiconductors GaAs and Ge, and multiferroic LuMnO_3 with femtosecond time resolutions. The excitation mechanism of the coherent optical phonon in Ge is transient stimulated Raman scattering and that in GaAs is a mixture of transient stimulated Raman scattering and hot electron effect.

The relaxation time of the Mn $d_{xy}, x^2-y^2 \rightarrow d_{3z^2-r^2}$ excitation is of $.8 \pm .2$ ps. A coherent phonon, involving Lu ions moving along the c-axis is resonantly excited, and the dephasing time is of 4 ± 2 ps. The excitation mechanism of this coherent phonon could be TSRS, or a screening effect of photoexcited electrons, or a combination of two.

Appendix A

An Introduction to Femtosecond Laser Pulses

Laser pulse is used in lots of scientific field due to its short duration, broad spectrum, high repetition rate and peak intensity [2]. There are lots of review papers talk about the techniques in this field [2, 3, 137, 138, 139, 140, 141, 142]. In my graduate student life, I have been aligning pulse laser and optimizing pulse energy and duration for very long time. In this appendix, I will talk about my understanding about the pulse laser and laser pulse. Some of them comes from the reference and the other comes directly from my experience. In the first section, I will talk about what is the laser pulse, and how to measure its pulse width. In the second section, I will talk about the propagation of the laser pulse, include group velocity dispersion and compensation methods. In the last section, laser pulse generation will be introduced.

A.1 Wave Packets and Pulse Width Measurement

An wave pulse can be express at

$$E(t) = \sum_{k=-n}^n A_k \exp \{i(2\pi(\nu_0 + k\delta\nu)t + \Phi_k)\} \quad (\text{A.1})$$

Here, ν_0 refers to the center frequency, A_k and Φ_k denote the amplitude and the phase of mode k respectively. In its best shape, the phase Φ_k can be a constant or constant+ $2n\pi$ (n represents a integer). If the $E(t)$ has a Gauss shape, A_k also have a Gauss distribution by k . From the equation A.1, we can calculate out the pulse width in the best situation (which means $\Phi_k = \text{const} + 2n\pi$) from the measured spectrum (A_k). This pulse width is named transform limit pulse width. The left panel in Fig. A.2 is one of the spectra in

our experiments. The width of spectra is 57 nm, which corresponding to a transform limit pulse width 17 fs. However, in the real situation, Φ_k can not be in the best situation, it disperses in the some degree, which elongate the pulse width. We have have to measure it in real time. For femtosecond pulses, autocorrelation, frequency-resolved

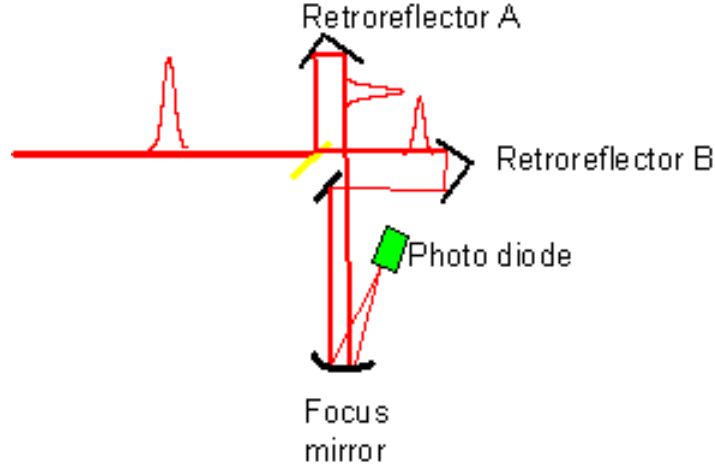


Figure A.1: Schematic diagram of autocorrelation measurement. The yellow line is the beam splitter, and black line is the mirror.

optical gating (FROG) [143] are commonly used. Some advanced method is autocorrelation data together with the fundamental spectrum [144, 145]. In our experiment, autocorrelation used to measure the pulse width, while spectrometer is used to monitor the spectra. Fig. A.1 is a schematic of autocorrelation measurement. In this schematic, the yellow line and black line represent beam splitter and mirror respectively. The photodiode only response to the photon with wavelength ranging from 300nm to 600 nm, which means the output current of the photodiode is excited by two photon effect. The femtosecond pulse beam is split into two parts, both of them pass a certain path, then focus onto the photodiode. The photodiode output current is proportional to average of the square of transient beam intensity. If the delay time between the two pulses arriving the same photodiode area is τ , the output current can be expressed by

$$I(\tau) = \alpha \int (I_1(t) + I_2(t+\tau))^2 dt = \alpha \int I_1(t)I_2(t+\tau)dt + \alpha \int I_1(t)^2 dt + \alpha \int I_2(t+\tau)^2 dt \quad (\text{A.2})$$

Here α is a constant, which is related to the sensitivity of the photo diode, the focusing and overlap of the two beam. The tighter the beam is focused, the larger α , and the better overlap in active area, the larger α . I_1 and I_2 are the intensities of the pump and probe beam respectively. From equation A.2, we know that the second and the third term on the right hand is independent to the τ . The average output of two photon current of these two terms will be DC currents when we scan the delay time τ . The first term is dependent to the value of the τ when the laser beam is a pulse beam. If two pulses do not have any time overlap, this term will be zero. The maximum value appears when two pulses have perfect time overlap. In the experiment, the current is recorded as function of τ when retro reflector B moves¹. If we know the pulse shape, we can easily calculate the pulse width t_p from the Half Maxim Full Width (HMFV) of the autocorrelation peak width t_a . For the Gauss shape, $t_a/t_p = \sqrt{2}$. For Lorentz shape pulse, the ratio is 2, and sech shape pulse, the ratio is 1.54. Figure A.2 right is an autocorrelation curve of a pulse with the spectra plotted in its left. The width of the peak is 33 fs, corresponding to 21 fs pulse width by assuming the shape is Sech. So there is some dispersion in the pulse.

A.2 Group Velocity Dispersion and Compensation

As I mentioned in last section, the pulse width measured by autocorrelation is 4 fs longer than the transform limit. This is due the group delay (GD) of pulses. When a pulse passes through a optical devices with length l , the spectral components with angular frequency ω delayed by a group delay

$$T_g(\omega) = \frac{l}{c} \frac{\partial}{\partial \omega}(\omega n) = \sum_{i=0}^{\infty} \frac{1}{i!} \frac{\partial^i T_g}{\partial \omega^i} \Big|_{\omega_0} (\omega - \omega_0)^i \quad (\text{A.3})$$

¹The motion direction of the the retro reflector B have to be parallel to the incident beam. Otherwise, the overlap on the diode or the sample will change when the retro reflector is scanning. when align the direction of the incident beam or scanning direction, half the laser spot were on the diode with large scanning range of the scanner. If the beam is well aligned, the output current of the diode should be a constant. Otherwise, it have a slope. Both vertical and horizontal direction should be tested.

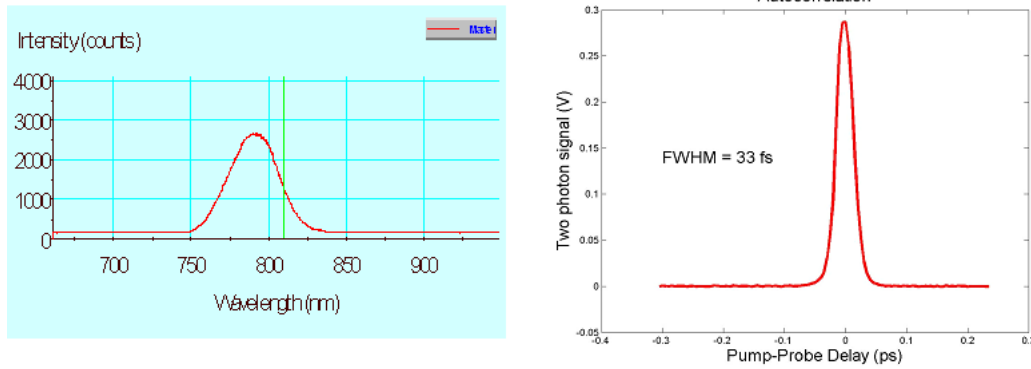


Figure A.2: The left graph is the spectrum of a pulse. The width of the spectrum is 57nm with center at 791 nm. The transform limit width of this pulse is 17 fs. The right is the autocorrelation result of this pulse, the width of this function is the 33 fs, assume the shape is sech, the pulse width will be 21 fs.

Here, c is the speed of the light in vacuum, n is the refractive index, which depends on ω , and ω_0 is a reference frequency for series expansion. The coefficient of the second order expansion $\frac{\partial T_g}{\partial \omega}$ is called group delay dispersion, which is the major term of the dispersion. However, when the pulse is shorter than 20 fs, the higher order dispersion can not be neglected. In the commonly, the non-absorptive materials generally exhibit positive dispersion, and the regrouping of different spectral components needs the negative dispersion. Methods to obtain the negative dispersion are grating pairs, prism pairs [146, 147] and chirped mirror [3, 142]. The grating pairs are not commonly used due to the lost of energy via higher order diffraction.

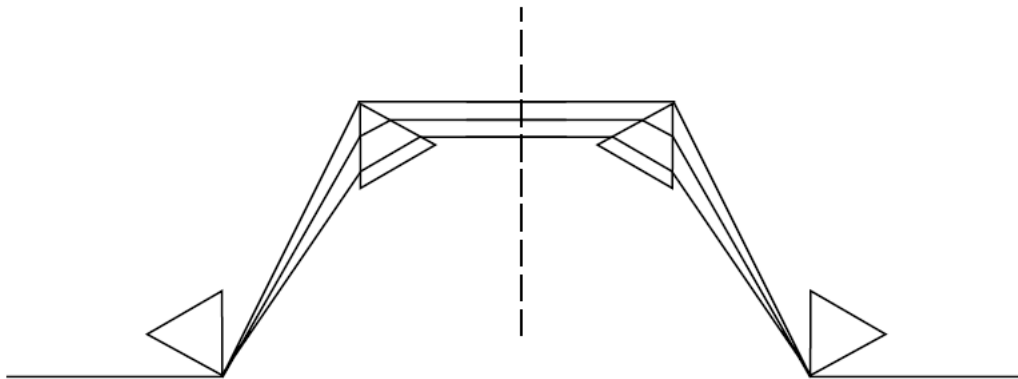


Figure A.3: Schematic of optical path of of prism pairs

Prism pairs, which were used in our experiments, have been used to compensate

dispersion since 1984. Prism pairs are arranged as Fig. A.3 shown. In experiments, prism is set at an angle of minimum deviation for central frequency. The first prism disperse the light of different frequencies to different directions. The second one make these lights parallel, the third focus these disperse light to a point the forth prism. The forth combines them together as a pulse beam. A mirror is used in the position of the dash line in Fig. A.3 to save the space on the optical bench and a pair of prism, and the compensated beam is picked out at the same place. Fig. A.4 are the schematic for

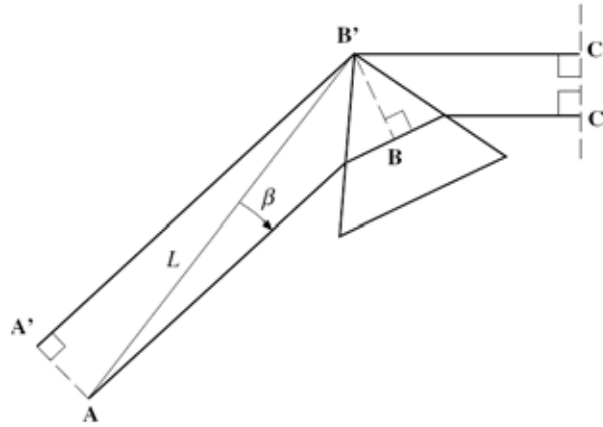


Figure A.4: Schematic for calculating the prism pair dispersion

calculating the prism pair dispersion. Point A represents the apex of the first prism, the beam of the central frequency directly passes to the position B'. The dispersed beam pass through point B to C. We can draw an equivalent path A'B'C'. If the distance between the apex of the two prism is L, so the optical path from A to B can be expressed

$$l_{p-p} = L \cos [\beta(\omega)] \quad (\text{A.4})$$

$\beta(\omega)$ represents the disperse angle from the center frequency light. Thus, the phase obtained by traveling through the prism pairs is:

$$\phi(\omega) = \frac{\omega}{\epsilon} 2l_{p-p} = \frac{2L\omega}{\epsilon} \cos [\beta(\omega)] \quad (\text{A.5})$$

The group delay dispersion (GDD) is the second derivation of the $\phi(\omega)$. If we assume the refractive index $n = n_0 + n_1$, n_0 is the part that independent to frequency and n_1 is

the frequency dependent term. Thus, $\cos[\beta(\omega)]$ can be expressed in to second order of n_1 ,

$$\cos[\beta(\omega)] = 1 - n_1 \left(\frac{n_0^2 \sin^2 \varphi}{\sqrt{1 - n_0^2 \sin^2 \varphi}} - 2n_0 \sin^2 \varphi \right) - n_1^2 \left[\frac{n_0 \sin^2 \varphi}{2\sqrt{1 - n_0^2 \sin^2 \varphi}} \left(4 - 2\tan^2 \varphi + \frac{n_0^2 \sin^2 \varphi}{1 - n_0^2 \sin^2 \varphi} \right) + \sin^2 \varphi \tan^2 \varphi \right] \quad (\text{A.6})$$

Here, φ is the half of apex angle of first prism. If we only want to obtain sign of GDD, we only need to expand n_1 to $a\omega$, and third term in equation A.6 is small compare to the second term. GDD is expressed

$$\frac{d^2 \phi}{d\omega^2} = \frac{-2aL}{\epsilon} \left(\frac{n_0^2 \sin^2 \varphi}{\sqrt{1 - n_0^2 \sin^2 \varphi}} - 2n_0 \sin^2 \varphi \right) \quad (\text{A.7})$$

For the material of the prisms, $a > 0$, so the condition of $d^2 \phi/d\omega^2$ is

$$\frac{n_0^2 \sin^2 \varphi}{\sqrt{1 - n_0^2 \sin^2 \varphi}} - 2n_0 \sin^2 \varphi > 0$$

which means

$$\sin \varphi > \sqrt{\frac{1}{n_0^2} - .25} \quad (\text{A.8})$$

Equation A.8 is pretty easy to satisfy. Most of the right angle prism can satisfy it. From equation A.7, the compensation of the GDD with prism pairs is proportional to the distance between prisms (L). If first prism in the path is inserted more, which equal to elongate L , GDD will be compensated more. Insert second prism more only increases more positive GDD material in the path. However, the high order of dispersion we have not calculated yet. The prism pairs can only compensate one order of dispersion. When we use prisms to compensate the dispersion, the first order can be compensated, but the higher order dispersion still exists, may even larger. In the our experiment, our measured pulse width is about 3 fs larger that the transform limit of the spectral due to the high order dispersion. The most obvious way to avoid it is to make the laser beam pass as less material as possible.

When light incident on the chirped mirror, the longer wavelength light can penetrate deeper in the mirror, thus obtain negative dispersion by passing through this mirror. The dispersion function is design by the sequence and thickness of layers of dielectric material coated on the mirror. Reference [3] discussed the principle of chirped mirror and the advanced product, double chirped mirror. When the chirped mirror is used to compensate the dispersion, the number of bound from the mirror is an adjustable parameter. One of the technique can only compensate one order dispersion. The combination of techniques can compensate multi-orders dispersion. It is reported a pairs of prisms combined with a grating pairs compensated the first and second order of equation A.3 (quadratic and cubic phase distortion) [148].

A.3 Laser Pulse Generation

The techniques to produce the laser pulse are Q-switch [141,149,150,151], active mode locking [137, 141, 152, 153, 154] and passive mode locking [141]. The width of pulse produce by these technique are in the order of nanoseconds, picoseconds, and femtosecond respectively. In this section, I will only talk about the passive mode locking, which is the laser that we used in our experiment, and is used in wide area of research field in the world. If someone have interest in Q-switch or active mode locking, the references have the better narration. In the passive mode locking, intracavity nonlinear elements change radiation fields in a cavity to produce the laser pulse. There are several kinds of the nonlinear elements used in the mode locking, for example, additive pulse mode locking (APM) which uses an additional cavity coupling to the main resonator [155,156,157,158,159,160], Kerr-lens mode locking (KLM) which uses the Kerr effect to realize the mode locking. Ti:Sapphire laser is one of Kerr-Lens mode locking lasers. Chirped Optical Parametric Amplification is a new method to obtain the higher peak energy, shorter pulse width, and variable center wave length of the pulse [142].

A.3.1 Principle of Kerr-Lens Mode-locking

The femtosecond pulse laser cavity is composed of 3 major function parts: a gain media, a mode-locking element, and a GDD or GVD compensator. As we discussed in section A.1, femtosecond wave packages have very broad spectral width, which requires the gain media support a very broad spectral gain. In the Ti:sapphire laser, the Ti:Sapphire crystal works as the gain media for the laser whose maximum gain ranges from 650 nm to 1100 nm [161]. A prism pair is commonly used as GVD compensator in Ti:sapphire lasers. In recent years, the double chirped mirror or combine with the prism pairs become more popular since they can compensate the GVD better. However, in our laser, we only have the prism pairs. In the Kerr Lens Mode-locking, the Kerr effect of a gain media is also a mode-locking element. In the Ti:sapphire laser, the Ti:sapphire crystal acts as both gain media and mode-locking element.

Kerr effect is the name of the nonlinear effect that the refractive index is dependent of intensity of the light beam, $n = n_0 + In_2$. When light beam propagated through a Kerr effect device with length L , the phase delay can be expressed by

$$\Phi = -2\pi nL/\lambda = -2\pi L(n_0 + In_2)/\lambda$$

Here, λ is the wave length of the light. The intensity dependent phase modulation can produce the time dependent of the frequency shift,

$$\delta\omega = \frac{d\phi}{dt} = \frac{-2\pi Ln_2}{\lambda} \frac{dI}{dt} \quad (\text{A.9})$$

In the case of positive n_2 , we can see that the front part of the pulse, in which the intensity is increasing, the frequencies shift to lower, and frequencies shift to higher at the back part of the pulse. Thus, the pulse has broader spectra after it passes through a Kerr effect device. In the other word, it has the shorter transform limit pulse width. However, when the pulse pass through Ti:sapphire crystal, the phase is dispersed. Prism pairs or some other devices will compensate the GDD. To obtain stable pulses, devices in a laser should arrange in some special position. Hnilo used an iterative map

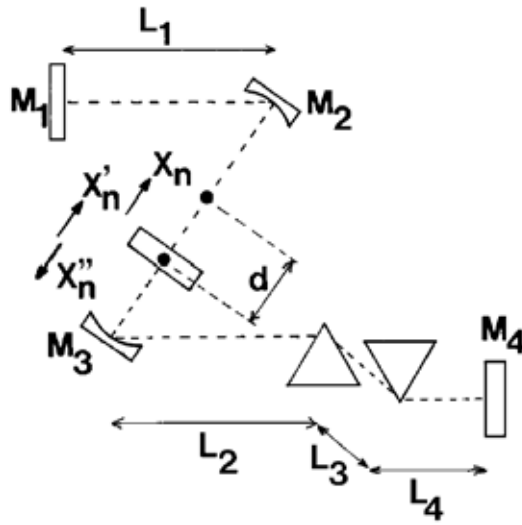


Figure A.5: Ti:Sapphire laser schematic for calculation. d is the distance between focal point of mirror M_2 and M_3

to describe the generation of laser pulse [162]. The main idea is that a pulse should have stable energy, pulse width, spectrum, pulse geometry after it pass through all three functional elements. Fig. A.6 is a schematic of Ti:sapphire laser used in the calculating model. Fig. A.6 is relation between the pulse energy, pulse duration and the negative GVD introduced by the prism pairs with fixed d . Here D is the net negative GVD that prism pairs produced, and τ is the pulse duration, U is the pulse energy. The dash line is the results of the iterative map, and the solid line are the result of another method [163]. It is obvious that the pulse width decreases when the prism insertion increases. However, the pulse energy decrease much slower than the pulse width. Fig. A.7 are the region of stability (not shadowed). Here, V is proportional to d and a constant equal to $8L_1/r^2$ (r is the curvature radius of the focal mirror M_3). When the negative D is large, the stable state area is much large, which means it is easy to find out the stable region. Second, the inner region (which means the distance between the focal point of M_3 and M_2 is smaller) of the stable can reach the shortest pulse duration. In this calculation, the gain of the media also affect the width of stable region. When the gain is larger, the stable region band became narrow, but the pulse duration can reach shorter. Thus,

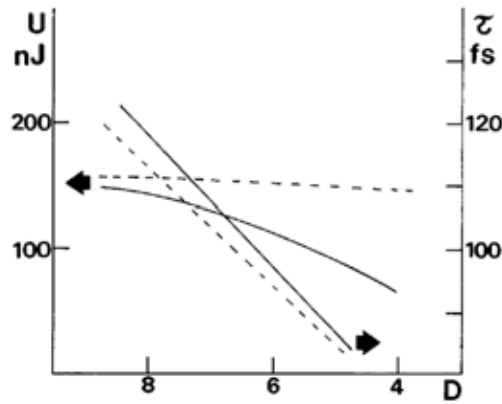


Figure A.6: Variation of pulse duration τ and energy U at the fixed d as a function of the negative GVD introduced by the prisms, D (in thousands of fs^2). [162]

the search of the stable region becomes more difficult. If we vary the length of L_1 , the output pulse will have multiple shape [164].

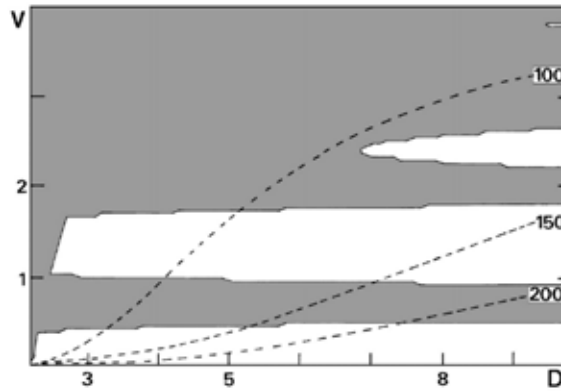


Figure A.7: Region of stability (not shadowed). D (in thousands of fs^2) is the negative GVD introduced by the prisms. The dot curves are the isobars joining points of equal pulse duration (fs).

A.3.2 Aligning the Ti:Sapphire Laser

In this section, the procedure in our experiment will be talked about. The Ti:Sapphire laser was bought from the KM lab, some of my view came from the *instruction manual* and *frequently asked questions*. Fig. A.8 is the schematic of the Ti:sapphire laser. The devices are labeled in the figure.

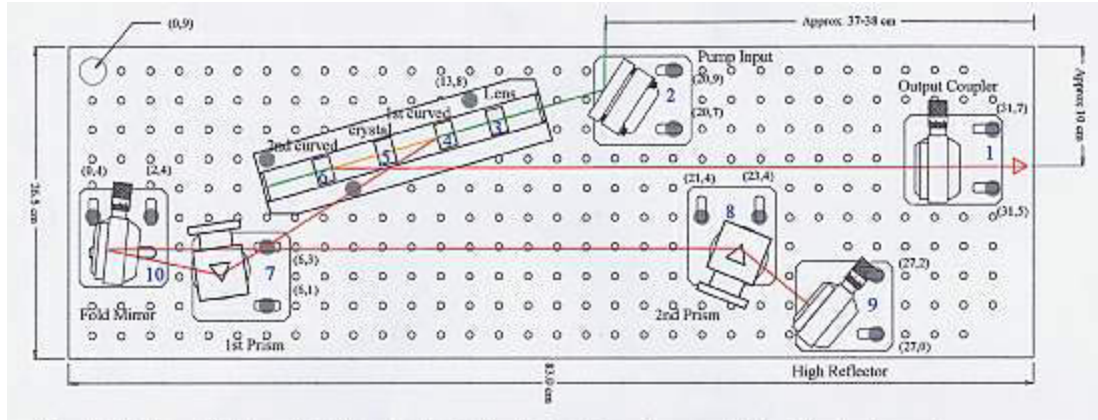


Figure A.8: Ti:Sapphire laser schematic

In our procedure, the first step is adjusting the knobs on the output coupler and high reflector to make the light bounce back to the coming direction from these devices in the condition of enough pump power. Then, slowly adjust the knobs on those two devices, to tune up the laser energy, in the other word, to maximize the gain. At this stage, the output coupler and high reflector change its direction at same time. This will change the inferred beam direction in the Ti:sapphire crystal (called walk the beam). When the laser output is maximized, the inferred beam overlaps green pump beam in the Ti:Sapphire crystal. Due to the color dispersion of the crystal, the inferred beam should have smaller incident angle than the pump green beam to Ti:sapphire crystal. If we watch the beam spot on the end curve mirror, the inferred spot is on the side close to wall. The distance between two spot is about 1.5 spot size center to center. In this process, we also need to move the position of the crystal to make sure it was on the focal point of first curve mirror and lens. Then, we also move the end curve mirror to maximize the output power.

After we maximize the CW output power, we minimize the insertion of the prism in the optical path to obtain maximum stable region for mode-locking. By gently shake the 2nd prism while very slowly moving the end mirror forward, we can find out the pulse spectra in the spectrum meter. Stop moving the end curve mirror when see the mode locking.

When the mode locking is found, the spectrum width is still narrow. We can insert more 1st prism to wide the spectra. However, this may lead to lost the mode-locking. If so, just move the end curve mirror a little bit, about 0.02mm. If there are some CW break through in the mode lock spectral, do the same. Do it repeatedly, until the spectrum width is about 40 nm. If there something else happen, please read the instruction manual of the laser and read the reference listed in this appendix.

Appendix B Optical Modulator

To obtain high frequency intensity oscillation of the laser beam, a resonant optical modulator has been designed, which works at 13.765 kHz. When it used with an optical slit, the intensity of the laser beam oscillates at a frequency of 27.53 kHz.

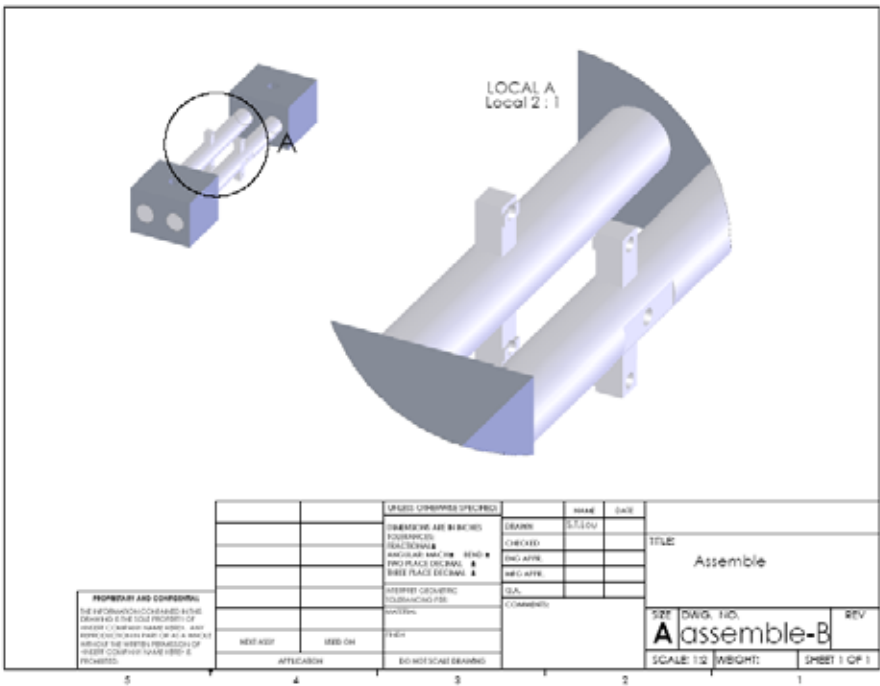


Figure B.1: 3D schematic of the optical modulator.

Fig. B.1 is the design effect schematic drawing of optical oscillator. The long flat facet at outside center of the bar is a place for mounting a retro reflector. On the outside of the other bar, there is a position for mounting a 1/4 inch diameter mirror for reflecting laser beam. Between two small rods, two piezo drivers have been installed for driving

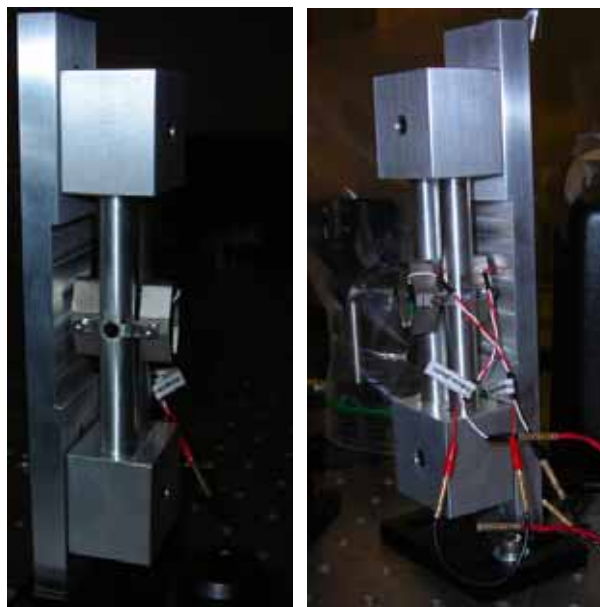


Figure B.2: Photographs of the optical modulator taken from two opposite sides

main rods to rotating oscillation. Figure B.2 are the photograph of the finished optical modulator. They were taken from the opposite sides in order to better illustrated. When piezo drivers are connected in serial with opposite electrodes (red electrodes connects to red electrodes), two piezo drivers extend and shrink in the opposite phases, driving the mirror to walk the laser beam periodically at a frequency of driving frequency. When piezo drivers are connected in serials with same current direction (red electrodes connected to white electrodes), the retro reflector will oscillate the optical path length at the driving frequency. It is best to driving it at its resonant frequency (13.765 kHz). When it works at its resonant frequency, the current passes the piezo drivers is pretty large. A home designed current amplifier has been built to drive this modulator. Its schematic is shown in Fig. B.3. To protect over load of the current driver, a $2\ \Omega$ resistor is serial in the output circuit of current amplifier..

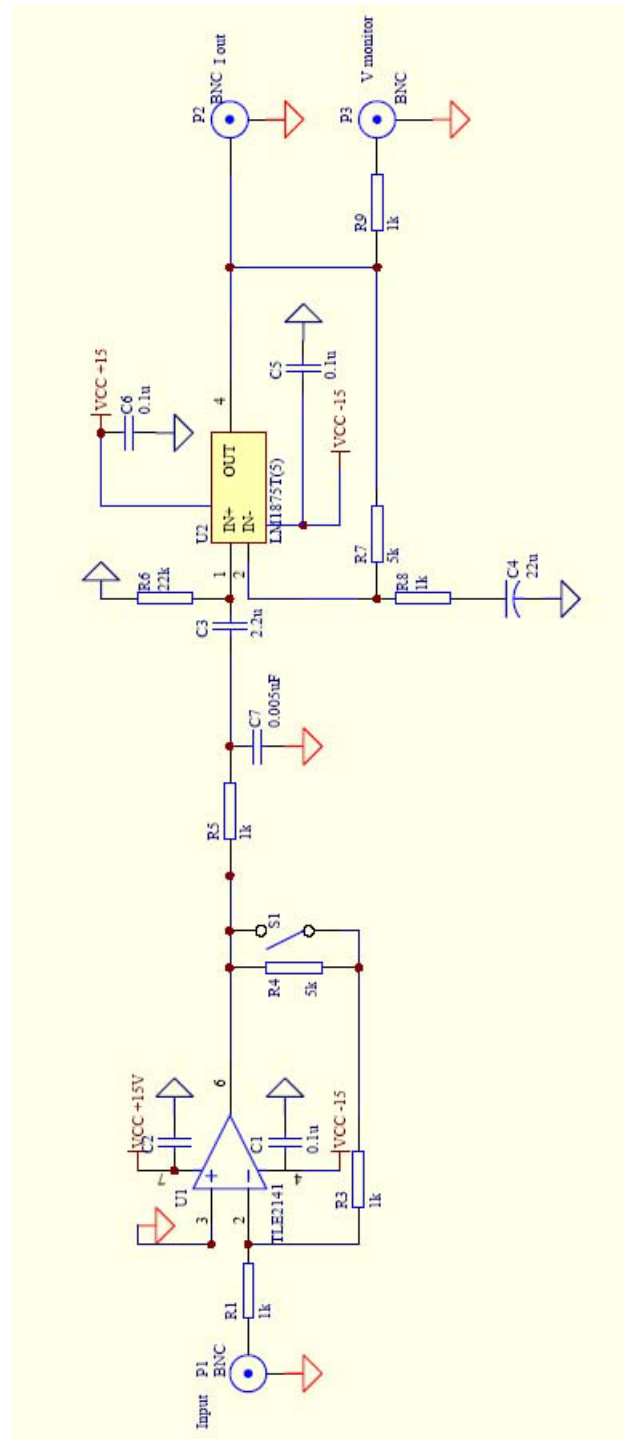


Figure B.3: Schematic of current driver of the optical modulator

Appendix C

List of Acronyms

APM	Additive Pulse Mode-locking
COPA	Chirped Optical Parametric Amplification
CWT	Continuous wavelet transfer
DECP	displacive-excitation of coherent phonon
FSS	Femtosecond spectroscopy
FWM	Four wave mixing
FROG	Frequency resolved optical gating
GDD	Group Delay Dispersion
GVD	Group Velocity Dispersion
ISRS	Impulsive stimulate Raman scattering
KLM	Kerr Lens Mode-Locking
LEED	Low energy electron Diffraction
LO	Longitudinal optical
TO	Transverse Optical
TSRP	transient stimulated Raman scattering

References

- [1] Innovation and technology Transfer **5**, 12 (1999).
- [2] U. Keller, Nature **424**, 831 (2003).
- [3] G. Steinmeyer, D. Sutter, G. L., Matuschek, and K. U., Science **286**, 1507 (1999).
- [4] D. von der Linde, J. Kuhl, and H. Klingenberg, Physical Review Letters **44**, 1505 (1980).
- [5] J. Y. Bigot, M.-A. Mycek, S. Weiss, R. G. Ulbrich, and D. Chemla, Physical Review Letters **70**, 3307 (1993).
- [6] D. Chemla, J. Y. Bigot, M.-A. Mycek, S. Weiss, and S. Scafer, Physical Review B **50**, 8439 (1994).
- [7] A. Kimel, R. Pisarev, F. Bentivegna, and T. Rasing, Ferroelectrics **279**, 135 (2002/).
- [8] A. Othonos, J. physics: Condens. Matter **16**, R995 (2004).
- [9] A. Othonos, Journal of applied physics **83**, 1789 (1998).
- [10] J. Shah, *Ultrafast spectroscopy of semiconductors and semiconductor nanostructure* (Springer, New York, USA, 1998).
- [11] R. Merlin, Solid State Communications **102**, 207 (1997/04/).
- [12] H. Bakker, s. Hunsche, and H. Kurz, Review of Modern Physics **70**, 523 (1998).
- [13] G. Garrett, T. Albrecht, J. Whitaker, and R. Merlin, Physical Review Letters **77**, 3661 (1996/10/21).
- [14] D. Lim, R. Averitt, J. Demsar, A. Taylor, N. Hur, and S. Cheong, Applied Physics Letters **83**, 4800 (2003/12/08).
- [15] A. Gambetta, C. Manzoni, E. Menna, M. Meneghetti, G. Cerullo, G. Lanzani, S. Tretiak, A. Piryatinski, A. Saxena, R. L. Martin, and A. R. Bishop, NATURE PHYSICS **2**, 515 (2006).
- [16] H. Petek and S. Ogawa, Progress in Surface Science **56**, 239 (1997/12/).

- [17] M. Woerner, K. Reimann, and T. Elsaesser, *Journal of Physics: Condensed Matter* **16**, 25 (2004/02/04).
- [18] W. Lin, L. Fujimoto, E. Ippen, and R. Logan, *Applied Physics Letters* **50**, 124 (1987/01/19).
- [19] R. Averitt and A. Taylor, *Journal of Physics: Condensed Matter* **14**, 1357 (2002/12/23).
- [20] Y. Ren, X. Zhang, G. Lupke, M. Schneider, M. Onellion, I. Perakis, Y. Hu, and Q. Li, *Physical Review B (Condensed Matter and Materials Physics)* **64**, 144401 (2001/10/01).
- [21] Y. Shen, *Applied Physics A (Solids and Surfaces)* **A59**, 541 (1994/11/).
- [22] K. Kuhnke, R. Becker, H. Berger, and K. Kern, *Journal of Applied Physics* **79**, 3781 (1996/04/01).
- [23] I. Kityk, J. Kasprczyk, and K. Plucinski, *Journal of the Optical Society of America B (Optical Physics)* **16**, 1719 (1999/10/).
- [24] J. Hohlfeld, U. Conrad, and E. Matthias, *Applied Physics B (Lasers and Optics)* **B63**, 541 (1996/11/).
- [25] A. McClelland, V. Fomenko, and E. Borguet, *Journal of Physical Chemistry B* **110**, 19784 (2006/10/12).
- [26] Y. Glinka, T. Shahbazyan, I. Perakis, N. Tolk, X. Liu, Y. Sasaki, and J. Furdyna, *Surface and Interface Analysis* **35**, 146 (2003/02/).
- [27] G. Kodis, V. Gulbinas, L. Valkunas, and S. Jursenas, *Advanced Materials for Optics and Electronics* **6**, 391 (1996).
- [28] Y. Hu, S. Koch, and N. Peyghambarian, *Journal of Luminescence* **70**, 185 (1996).
- [29] F. Kadlec, C. Kadlec, P. Kuzel, P. Slavicek, and P. Jungwirth, *Journal of Chemical Physics* **120**, 912 (2004).
- [30] G. Dakovski, B. Kubera, S. Lan, and J. Shan, *Journal of the Optical Society of America B (Optical Physics)* **23**, 139 (2006/01/).
- [31] F. Hegmann, R. Tykwinski, K. Lui, J. Bullock, and J. Anthony, *Physical Review Letters* **89**, 227403 (2002/11/25).
- [32] J. Kitagawa, Y. Kadoya, M. Tsubota, F. Iga, and T. Takabatake, *Journal of Magnetism and Magnetic Materials* **310**, 913 (2007).
- [33] B. Ferguson and X. Zhang, *NATURE MATERIALS* **1**, 26 (2002).

- [34] D. Dragoman and M. Dragoman, PROGRESS IN QUANTUM ELECTRONICS, **28**, 1 (2004).
- [35] Q. Wu and X.-C. Zhang, Applied Physics Letters **67**, 3523 (1995).
- [36] O. Mitrofanov, M. Lee, J. Hsu, I. Brener, R. Harel, J. Federici, J. Wynn, L. Pfeiffer, and K. West, IEEE Journal of Selected Topics in Quantum Electronics **7**, 600 (2001/07/).
- [37] O. Mitrofanov, M. Lee, L. Pfeiffer, and K. West, Applied Physics Letters **80**, 1319 (2002/02/25).
- [38] J. Williamson, M. Dantus, S. Kim, and A. Zewail, Chemical Physics Letters **196**, 529 (1992/08/28).
- [39] J. Williamson, J. Cao, H. Ihee, H. Frey, and A. Zewail, Nature **386**, 159 (1997/03/13).
- [40] J. Cao, H. Ihee, and A. Zewail, Chemical Physics Letters **290**, 1 (1998/06/26).
- [41] H. Ihee, V. Lobastov, U. Gomez, B. Goodson, R. Srinivasan, C.-Y. Ruan, and A. Zewall, Science **291**, 458 (2001/01/19).
- [42] R. Srinivasan, V. Lobastov, C. Y. Ruan, and A. H. Zewail, HELVETICA CHIMICA ACTA **86**, 1763 (2003).
- [43] A. Scholl, L. Baumgarten, R. Jacquemin, and W. Eberhardt, Physical Review Letters **79**, 5146 (1997/12/22).
- [44] M. Hase, M. Kitajima, K. Mizoguchi, and S. Nakashima, Physica B **316-317**, 292 (2002).
- [45] M. Hase, K. Mizoguchi, H. Harima, S. Nakashima, M. Tani, K. Sakai, and M. Hangyo, Applied Physics Letters **69**, 2474 (1996/10/21).
- [46] M. Hase, K. Ishioka, M. Kitajima, S. Hishita, and K. Ushida, Applied Surface Science **197-198**, 710 (30 Sept. 2002).
- [47] U. Bovensiepen, Journal of Physics-Condensed Matter **19**, 083201 (2007).
- [48] U. Bovensiepen, Applied physicsA **82**, 395 (2006).
- [49] A. Melnikov, I. Radu, U. Bovensiepen, O. Krupin, K. Starke, E. Matthias, and M. Wolf, Physical Review Letters **91**, 227403 (2003/11/28).
- [50] W. Lin, L. Fujimoto, E. Ippen, and R. Logan, IEEE Journal of Quantum electronics **24**, 267 (1988).
- [51] A. Dementyev, P. Khandelwal, N. Kuzma, S. Barrett, L. Pfeiffer, and K. West, Solid State Communications **119**, 217 (2001/).

- [52] G. Gilliland, Mater. Sci. Eng. R Rep. (Switzerland) **R18**, 99 (1997/03/).
- [53] H. Haug, Progress in Quantum Electronics **29**, 261 (2005//).
- [54] E. Knoesel, M. Bonn, J. Shan, and T. Heinz, Physical Review Letters **86**, 340 (2001/01/08).
- [55] C. Cesar, J. Jacob, G., G. Tudury, M. Marquezini, and L. Barbosa, Atti della Fondazione Giorgio Ronchi **59**, 519 (2004/07/).
- [56] D. Chemla, Comptes Rendus de l'Academie des Sciences, Serie IV (Physique, Astrophysique) **2**, 1427 (2001/12/).
- [57] R. Kaindl and R. D. Averitt, Thz Spectroscopy: Principle and applications (2007).
- [58] W. Lin, L. Fujimoto, E. Ippen, and R. Logan, Applied Physics Letters **51**, 161 (1987).
- [59] L. Schultheis, J. Kuhl, A. Honold, and C. Tu, Physical Review Letters **57**, 1797 (1986).
- [60] M. Woerner, Laser Physics **5**, 611 (1995/05/).
- [61] G. Cho, W. Kutt, and H. Kurz, Physical Review Letters **65**, 764 (1990).
- [62] T. Pfeifer, W. Kutt, H. Kurz, and R. Scholz, Physical Review Letters **69**, 3248 (1992/11/30).
- [63] T. Pfeifer, W. Dekorsy, T. and Kutt, and H. Kurz, Applied physics A **55**, 482 (1992).
- [64] T. Dekorsy, T. Pfeifer, W. Kutt, and H. Kurz, Physical Review B (Condensed Matter) **47**, 3842 (1993).
- [65] H. Zeiger, J. Vidal, T. Cheng, E. Ippen, G. Dresselhaus, and M. Dresselhaus, Physical Review B **45**, 768 (1992).
- [66] T. Stevens, J. Kuhl, and R. Merlin, Physical Review B (Condensed Matter) **65**, 144304 (2002).
- [67] M. Hase, M. Kitajima, A. Constantinescu, and H. Petek, Nature **425**, 51 (2003/11/06).
- [68] M. Hase, S. Nakashima, K. Mizoguchi, H. Harima, and K. Sakai, Physical Review B (Condensed Matter) **60**, 16526 (1999/12/15).
- [69] M. Hase, K. Mizoguchi, H. Harima, F. Miyamaru, S. Nakashima, R. Fukasawa, M. Tani, and K. Sakai, Journal of Luminescence **76-77**, 68 (1998/02/).

- [70] A. V. Kuznetsov and C. J. Stanton, Physical Review B (Condensed Matter and Materials Physics) **51**, 7555 (1995).
- [71] A. Lobad, R. Averitt, and A. Taylor, Physical Review B (Condensed Matter) **63**, 060410 (2001/02/01).
- [72] K. Nontapot, R. Kini, A. Gifford, T. Merritt, G. Khodaparast, T. Wojtowicz, X. Liu, and J. Furdyna, Applied Physics Letters **90**, 143109 (2007/04/02).
- [73] R. Prasankumar, H. Okamura, H. Imai, Y. Shimakawa, Y. Kubo, S. Trugman, A. Taylor, and R. Averitt, Physical Review Letters **95**, 267404 (2005/12/31).
- [74] K. Miyasaka, M. Nakamura, Y. Ogimoto, H. Tamaru, and K. Miyano, Physical Review B (Condensed Matter and Materials Physics) **74**, 12401 (2006/07/01).
- [75] A. Souchkov, J. Simpson, M. Quijada, H. Ishibashi, N. Hur, J. Ahn, S. Cheong, A. Millis, and H. Drew, Physical Review Letters **91**, 027203 (2003/07/11).
- [76] A. Kimel, A. Kirilyuk, P. Usachev, R. Pisarev, A. Balbashov, and T. Rasing, Nature **435**, 655 (2005/06/02).
- [77] K. Takahashi, N. Kida, and M. Tonouchi, Physical Review Letters **96**, 117402 (2006/03/24).
- [78] R. Lu, M. Hase, M. Kitajima, S. Nakashima, and S. Suga, Physical Review B (Condensed Matter) **75**, 012107 (2007).
- [79] K. Istomin, V. Kotaidis, and A. Plech, Applied Physics Letters **90**, 022905 (2007).
- [80] H. M. Perry and T. P. Dougherty, Physical Review B (Condensed Matter) **55**, 5778 (1997).
- [81] D. Dvorsek, V. Kabanov, J. Demsar, S. Kazakov, J. Karpinski, and D. Mihailovic, Physical Review B (Condensed Matter and Materials Physics) **66**, 020510 (2002/07/01).
- [82] O. Misochko, K. Sakai, and S. Nakashima, Physica C **329**, 12 (2000/01/01).
- [83] N. Gedik, P. Blake, R. Spitzer, J. Orenstein, R. Liang, D. Bonn, and W. Hardy, Physical Review B (Condensed Matter and Materials Physics) **70**, 14504 (2004/07/01).
- [84] Y. Long, L. Zhao, B. Zhao, X. Qiu, C. Zhang, P. Fu, L. Wang, Z. Zhang, S. Zhao, Q. Yang, and G. Wang, Physica C **436**, 59 (2006/04/15).
- [85] J. Chelikowsky and M. Cohen, Physical Review B **14**, 556 (1976).
- [86] <http://www.semiconductors.co.uk/propiiiv5653.htm> .

- [87] R. W. Boyd, *Nonlinear Optics* (Academic Press, CA, USA, 2003).
- [88] Y. R. Shen, *Principles of Nonlinear Optics* (New York, New York : Wiley, 2002).
- [89] <http://www.semiconductors.co.uk/propiviv5431.htm> .
- [90] A. Mysyrowicz, D. hulin, A. Antonett, A. Migus, W. Masselink, and H. Morkoc, *Physical Review Letters* **56**, 2748 (1986).
- [91] W. Knox, D. Chemla, D. Miller, and S. Schmitt-Rink, *Physical Review Letters* **62**, 1189 (1989).
- [92] P. Xin-Yu, W. Shu-Feng, H. Wen-Tao, Y. Hong, L. Xia, J. Hong-Bing, and G. Qi-Huang, *Chinese Physics Letters* **18**, 979 (2001/07/).
- [93] K. Myers, S. Zollner, R. Lange, K. Jensen, J. Dolan, D. Bailey, and C. Stanton, 23rd International Conference on the Physics of Semiconductors **vol.1**, 673 (1996).
- [94] W. Kutt, W. Albrecht, and H. Kurz, *IEEE Journal of Quantum Electronics* **28**, 2434 (1992/10/).
- [95] N.-H. Ge, C. Wong, J. Lingle, R.L., J. McNeill, K. Gaffney, and C. Haris, *Science* **279**, 202 (1998/01/09).
- [96] H.-C. Zhang, J.-H. Wen, B. Guo, and W.-Z. Lin, *Chinese Journal of Semiconductors* **21**, 867 (Sept. 2000).
- [97] A. Leitenstorfer, G. Goger, M. Betz, M. Bichler, G. Abstreiter, and W. Wegscheider, *Trends in Optics and Photonics. Twelfth International Conference on Ultrafast Phenomena. Vol.43. Technical Digest. Postconference Edition* 570 (2000//).
- [98] M. Betz, G. Goger, A. Leitenstorfer, R. Zimmermann, M. Bichler, W. Wegscheider, and G. Abstreiter, *Physica Status Solidi B* **231**, 181 (2002/05/).
- [99] L. Schultheis, J. Kuhl, A. Honold, and C. Tu, *Physical Review Letters* **57**, 1635 (1986).
- [100] M. Webb, S. Cundiff, and D.G.Steel, *Physical Review Letters* **66**, 934 (1991).
- [101] G. Noll, D. Siegner, S. Shevel, and E. O. Gobel, *Physical Review Letters* **64**, 792 (1990).
- [102] M. Koch, J. Feldmann, G. von Plessen, E. O. Gobel, P. Thomas, and K. Kohler, *Physical Review Letters* **69**, 3631 (1992).
- [103] D. C. A. Johnston, M. B.and Whittaker, A. Davies, and E. Linfield, *Physical Review B (Condensed Matter)* **65**, 165301 (2002).
- [104] A. Kuznetsov and C. Stanton, *Proceedings of the SPIE - The International Society for Optical Engineering* **3277**, 28 (1998//).

- [105] D. Aspnes and A. Studna, *Physical Review B (Condensed Matter)* **27**, 985 (1983/01/15).
- [106] M. H. Grimsditch, D. Olego, and M. Cardona, *Physical Review B* **20**, 1758 (1979).
- [107] M. Hase, J. Demsar, and M. Kitajima, *Physical Review B (Condensed Matter and Materials Physics)* **74**, 212301 (2006/12/01).
- [108] U. Fano, *Physical Review* **124**, 1866 (1961).
- [109] J. Lee, J. Inoue, and M. Hase, *Physical Review Letters* **97**, 157405 (2006/10/13).
- [110] H. Yakel, W. C. Koehlee, E. F. Bertaut, and E. F. Forrat, *Acta Cryst.* **16**, 957 (1963).
- [111] B. van Aken, A. Meetsma, and T. Palstra, <http://arxiv.org/abs/cond-mat/0106298>.
- [112] C. Fennie and K. Rabe, *Physical Review B (Condensed Matter and Materials Physics)* **72**, 100103 (1 Sept. 2005).
- [113] T. Katsufuji, M. Masaki, A. Machida, M. Moritomo, K. Kato, E. Nishibori, M. Takata, M. Sakata, K. Ohoyama, K. Kitazawa, and H. Takagi, *Physical Review B (Condensed Matter and Materials Physics)* **66**, 134434 (2002/10/01).
- [114] P. Sharma, J. Ahn, N. Hur, S. Park, S. B. Kim, S. Lee, J.-G. Park, S. Guha, and S.-W. Cheong, *Physical Review Letters* **93**, 177202 (2004/10/22).
- [115] M. Fiebig, C. Degenhardt, and R. Pisarev, *Journal of Applied Physics* **91**, 8867 (2002).
- [116] M. Fiebig, D. Frohlich, T. Lottermoser, and M. Maat, *Physical Review B (Condensed Matter and Materials Physics)* **66**, 144102 (2002/10/01).
- [117] O. Vajk, M. Kenzelmann, J. Lynn, S. Kim, and S.-W. Cheong, *Journal of Applied Physics* **99**, 08 (2006).
- [118] O. Vajk, M. Kenzelmann, J. Lynn, S. Kim, and S.-W. Cheong, *Physical Review Letters* **94**, 087601 (2005).
- [119] B. Lorenz, F. Yen, M. Gospodinov, and C. Chu, *Physical Review B (Condensed Matter and Materials Physics)* **71**, 14438 (2005/01/01).
- [120] F. Yen, C. Cruz, B. Lorenz, Y. Sun, Y. Wang, M. Gospodinov, and C. Chu, *Physical Review B (Condensed Matter and Materials Physics)* **71**, 180407 (2005/05/01).
- [121] B. Lorenz, A. Litvinchuk, M. Gospodinov, and C. Chu, *Physical Review Letters* **92**, 87204 (2004).

- [122] D. Tomuta, S. Ramakrishnan, G. Nieuwenhuys, and J. Mydosh, *Journal of Physics: Condensed Matter* **13**, 4543 (2001/05/21).
- [123] C. Cruz, F. Yen, B. Lorenz, Y. Wang, Y. Sun, M. Gospodinov, and C. Chu, *Physical Review B (Condensed Matter and Materials Physics)* **71**, 60407 (2005/02/01).
- [124] M. Iliev, H.-G. Lee, V. Popov, M. Abrashev, A. Hamed, R. Meng, and C. Chu, *Physical Review B (Condensed Matter)* **56**, 2488 (1997/08/01).
- [125] Y. Aikawa, T. Katsufuji, T. Arima, and K. Kato, *Physical Review B (Condensed Matter and Materials Physics)* **71**, 184418 (2005/05/01).
- [126] M. Fiebig, D. Frohlich, K. Kohn, S. Leute, T. Lottermoser, V. Pavlov, and R. Pisarev, *Physical Review Letters* **84**, 5620 (2000/06/12).
- [127] B. van Aken, T. Palstra, A. Filippetti, and N. Spaldin, *Nature Materials* **3**, 164 (2004/03/).
- [128] T. Katsufuji, S. Mori, M. Masaki, Y. Moritomo, N. Yamamoto, and H. Takagi, *Physical Review B (Condensed Matter and Materials Physics)* **64**, 104419 (1 Sept. 2001).
- [129] B. Van Aken and T. Palstra, *Physical Review B (Condensed Matter and Materials Physics)* **69**, 134113 (2004/04/01).
- [130] T. Lottermoser, T. Lonkai, U. Amann, D. Hohlwein, J. Ihringer, and M. Fiebig, *Nature* **430**, 541 (2004/07/29).
- [131] D. A. Long, *The Raman effect : a unified treatment of the theory of Raman scattering by molecules* (Chichester;, New York : Wiley, 2002).
- [132] V. N. Popov, *J. Phys. : Condens. Matter* **7**, 1625 (1995).
- [133] M. Taylor, G. Barrera, N. Allan, T. Barron, and W. Mackrodt, *Computer Physics Communications* **109**, 135 (1998/04/).
- [134] A. Litvinchuk, M. Iliev, V. Popov, and M. Gospodinov, *Journal of Physics: Condensed Matter* **16**, 809 (2004/02/18).
- [135] B. van Aken, A. Meetsma, and T. Palstra, *Acta Crystallographica, Section E (Structure Reports Online)* **E57**, (2001/11/01).
- [136] C. Bosshard, R. Spreiter, L. Degiogi, and Günter, *Physical Review B (Condensed Matter)* **65**, 144304 (2002).
- [137] E. Ippen, *Applied Physics B* **58**, 159 (1994).
- [138] A. M. Weiner, *Prog. Quant. Electr.* **19**, 161 (1995).

- [139] E. N. Glezer, Ph.D. thesis, Harvard University, 1996.
- [140] U. Keller, *Current Opinion in Solid states and materials Science* **1**, 218 (1996).
- [141] J. Kleinbauer, R. Knappe, and R. Wallenstein, *Topics in Appl. Phys.* **96**, 9 (2004).
- [142] A. Dubietis, R. Butkus, and A. P. Piskarskas, *IEEE Journal of Selected Topics In Quantum Electronics* **12**, 163 (2006).
- [143] R. Trebino and K. J. Daniel, *J. Opt. Soc. Am. A* **10**, 1101 (1993).
- [144] A. Baltuska, Z. Wei, and et al, *Applied Physics B* **65**, 175 (1997).
- [145] J. Peatross and A. Rundquist, *J. Opt. Soc. Am. B* **15**, 216 (1998).
- [146] R. L. Fork, O. E. Martinez, and J. P. Gordon, *Opt. Lett.* **9**, 150 (1984).
- [147] R. E. Sherriff, *J. Opt. Soc. Am. B* **15**, 1224 (1998).
- [148] R. L. Fork, C. H. B. Cruz, P. C. Beck, and C. V. Shank, *Optics Letters* **483**, 12 (1987).
- [149] C. Wu, Z. Wang, L. Cheng, and Y. Zhao, *Laser Physics* (Fudan University Press, Shanghai, China, 1989).
- [150] V. Arsen'ev, I. Matveev, and N. Ustinov, *Soviet Journal of Quantum Electronics* **7**, 1321 (1977/11/).
- [151] A. Penzkofer, *Applied Physics B (Photophysics and Laser Chemistry)* **B46**, 43 (1988/05/).
- [152] P. French, *Reports on Progress in Physics* **58**, 169 (1995/02/).
- [153] G. Malcolm and A. Ferguson, *Optical and Quantum Electronics* **24**, 705 (1992/07/).
- [154] I. Tomov, R. Fedosejevs, and M. Richardson, *Soviet Journal of Quantum Electronics* **10**, 797 (1980/07/).
- [155] E. Ippen, H. Haus, and L. Liu, *Journal of the Optical Society of America B (Optical Physics)* **6**, 1736 (Sept. 1989).
- [156] H. Haus, J. Fujimoto, and E. Ippen, *IEEE Journal of Quantum Electronics* **28**, 2086 (1992/10/).
- [157] S. Feldman, B. Moore, D. Weinberger, and H. Winful, *Optics Communications* **105**, 113 (1994/01/15).
- [158] S. Mathur, T. Brabec, S. Kelly, and E. Wintner, *Optics Communications* **105**, 73 (1994/01/15).

- [159] A. Major, N. Langford, T. Graf, and A. Ferguson, Applied Physics B (Lasers and Optics) **B75**, 467 (2002/10/).
- [160] J. Wang, Optics Letters **16**, 1104 (1991/07/15).
- [161] P. F. Moulton, J. Opt. Soc. Am. B **3**, 125 (1986).
- [162] A. Hnilo, J. Opt. SOC. Am. B **12**, 718 (1995).
- [163] O. E. Martinez and J. L. A. Chilla, Opt. Lett. **17**, 1210 (1992).
- [164] M. Kovalsky, A. Hnilo, A. Libertun, and M. Marconi, Optics Communications **192**, 333 (2001).

Vita

Shitao Lou

Education

- 05/2007 Ph.D. degree at Rutgers University, USA
- 10/2004 M.S. degree at Rutgers University, USA
- 06/2000 M.S. degree at Chinese Academy of Sciences, P.R.China
- 06/1997 B.S. degree at Fudan University, P.R.China

Presentation

1. *Femtosecond Spectroscopy of LuMnO_3* , Shitao Lou, F. M. Zimmermann, Robert A. Bartynski, N. Hur, S. W. Cheong, APS March meeting, Baltimore, March, 2006
2. *Femtosecond Spectroscopy of Electron-Lattice Coupling in LuMnO_3* , Shitao Lou, Frank M. Zimmermann, Robert A. Bartynski, N. Hur, S. W. Cheong, APS March meeting, Los angeles, March, 2005
3. *Development of Ultrafast Near-Field Optical Microscopy* Shitao Lou, Frank M. Zimmermann, Robert A. Bartynski, Brian Sheehy, Michael White, DOE Nanoscale-Science research centers workshop, Washington DC, February, 2003

Publications

1. *Coherent phonon excitation in GaAs and Ge* Shi-Tao Lou, , Frank M. Zimmermann, Robert Bartynski, in preparation
2. *Real-Time Dynamics of Coherent Optical Phonons in LuMnO_3* Shi-Tao Lou, , Frank M. Zimmermann, Robert A. Bartynski, Namjun Hur, Sang-Wook Cheong, in preparation.
3. *Degassing and Temperature Effects on the Formation of Nanobubbles at the Mica/Water Interface* Xue H. Zhang, Xiao D. Zhang, Shi T. Lou, et al. LANG-MUIR 20 (9): 3813-3815 APR 27 2004

4. *Studies of nanobubbles produced at liquid/solid interfaces* Lou ST, Gao JX, Xiao XD, et al. MATER CHARACTER 48(2-3): 211-214 APR 2002
5. *Nanobubbles at the liquid/solid interface studied by atomic force microscopy* Lou ST, Gao JX, Xiao XD, et al. CHINESE PHYS 10: S108-S110 Suppl. S JUL 2001
6. *NanoBubbles on Solid Surface Imaged by Atomic Force Microscope* Lou ST, Ouyang ZQ, Zhang Y, et al. J VAC SCI TECHNOL B 18 (5): 2573-2575 SEP-OCT 2000
7. *Nanobubbles at interface of solid and liquid*, Shitao Lou, Yi Zhang, Guanglai Li, Jun Hu, Mingquan Li, Micro- and Nanometer Science and Technology, Vol.5 No.1 430, 2000
8. *Two-dimensional Manipulation of Single Molecular DNA*, Yi Zhang, Qihua Xiong, Shitao Lou, Yibo Huang, Lin Tang, Guanglai Li, Bin Li, Jun Hu, Minqian Li, Micro- and Nanometer Science Technology, Vol.5 No.1 406-408, 2000
9. *Stretching DNA molecules with a centrifugal method and imaging with atomic force microscopy*, Yi Zhang, Qihua Xiong, Bin Li, Shitao Lou, Zhenqian Ouyang, Jun Hu, Minqian Li, Probe Microscopy, Vol.2, No.1, 31-36, 2000
10. *Remote Scanning Probe Microscope Based on Internet*, Lv Lu, Lou Shitao etc. High Technology letters, 2000(4), 45